DYNAMIC PHASE AND POPULATION CONTROL OF STATE SELECTED WAVE PACKETS IN Li_2

by

Joshua B. Ballard

University of Colorado

Boulder, Colorado

2003

Dynamic Phase and Population Control of State Selected Wave Packets in Li_2

By

Joshua B. Ballard

A.B., Harvard University, 1995

A thesis submitted to the

Faculty of the Graduate School of the

University of Colorado in partial fulfillment

of the requirements for the degree of Doctor of Philosophy

Department of Chemistry and Biochemistry

2003

This thesis for the Doctor of Philosophy degree by

Joshua B. Ballard

has been approved for the

Department of Chemistry and Biochemistry

by

_____

Stephen R. Leone

_____

David Jonas

Date_____

The final copy of this thesis has been examined by the signatories, and we find that both the content and the form meet acceptable presentation standards of scholarly work in the above mentioned discipline.

Ballard, Joshua (Ph.D., Physical Chemistry)

Dynamic Phase and Population Control of State Selected Wave Packets in Li_2

Thesis directed by Professor Stephen R. Leone

Pulse shaping of ultrafast pulses with a Liquid Crystal Spatial Light Modulator (SLM) is used to control both transient and non-transient state-resolved wave packet dynamics in Li_2. In almost all of the experiments, a single launch state (generally $A^1\Sigma_u^+$ v_A=11, J_A=28) is prepared via excitation with a cw laser, from which a pump pulse excites a superposition of states on an excited electronic potential energy curve followed by a photoionizing ultrafast probe pulse. Using feedback and an Evolutionary Algorithm (EA), the weak field pump-probe photoionization signal at a single time delay is optimized in Li_2 for the state $E\,^1\Sigma_g^+$ (v_E=9, J_E=27 & 29). First order time dependent perturbation theory is used to explain the mechanism by which the photoionization is maximized. Following this, the transient dynamics of excitation of wave packets is studied in detail. A clear separation is made between resonant and nonresonant effects. Both population and resultant phase in the molecule are transiently manipulated. By varying the polarization of the probe light, population dynamics can be separated from interfering wave packet dynamics, allowing precise determination of the instantaneous population and wave packet dynamics. A pulse shaping scheme is described that implements a sign inversion for one state of a two state superposition, and all sign inversion matrix elements are quantified. Elements of strong field coherent control are also explored in Li_2. From the launch state, the strong optical field couples the A and E electronic states,

inducing sequential $\Delta J=\pm 1$ transitions to populate states up to $\Delta J=\pm 4$. Taking advantage of Rapid Adiabatic Passage, state selectivity is controlled by manipulating chirp parameters on the excitation pulse, achieving selectivity of either Stokes or anti-Stokes quantum beats of nearly unity. Finally, wave packet dynamics on highly excited electronic states is examined. Electronic wave packets consisting of beating between bound states on the $F^1\Sigma_g^+$ and $G^1\Pi_g$ electronic states are observed.

“I thought of that while riding my bike.”

-Albert Einstein on the theory of relativity

Acknowledgements

To fully describe the degree to which I feel indebted to my wife for her support in this endeavor of studying graduate chemistry, a little background is in order. By 1997, after my wife and I had lived in San Francisco for a few years, we had a very comfortable existence. The internet and multimedia industries were blooming in The City, and jobs were plentiful and high paying. Even though I was enjoying a well paying position in high-tech, I had time to direct and produce my own movies for personal expression while my wife Rebecca and I were living in the most quaint neighborhood just two blocks from Golden Gate Park. From our front door, we could walk to any of sixty restaurants within five minutes. Even in this very urban environment, our house was surrounded by gardens, and we would wake to the sound of birds chirping without the usual din expected of the city. It was quite peaceful spending the morning in our mature garden sipping coffee and collecting our thoughts for the day.

On one particular trip home to visit the parents, I had a conversation with my father-in-law Garth Gillan, who at the time was a Professor of philosophy at the local university. I was telling him about how cool a life we were living, and he asked me if I felt like I was getting anything out of it, or if I was just whoring myself out to the highest bidder. Try to guess my answer…. Shortly after that, I quit my job to study chemistry. Within three months, I was taking some undergraduate chemistry courses, and we had moved to one of the roughest neighborhoods in San Francisco. It was typical to have to wade through a group of thugs clad in ski-masks to get up the stoop to our front door (actually, we'd just go to our back door). Now, instead of being

surrounded by birds chirping and gardens, we were in the midst of what would be considered a war zone anywhere but in America. One night, as Rebecca and I were on our way to BART, we passed by a bleeding stabbing victim. There were police there, so we kept on walking. One block later, we passed a gunshot victim. Hey, I wanted to go to graduate school. Rebecca knew that I needed to study to get to graduate school, so she endured this extreme change in situation—for me.

It is especially comforting to know that I have someone like Rebecca behind me. As might be expected, her support has not wavered since entering graduate school.

One particularly large series of events in graduate school revolved around relocating our lives and labs back to California. It would have been impossible to deal with if not for the collective impetus of everybody in the group. Laurie and Jodi were especially nice to have around. We started graduate school together and spent countless hours in the same room in lab. Seeing them in California is an important constant, helping make the personal adjustments bearable.

In lab, it has been a pleasure to share so many conversations with Hans Stauffer. He tends to get worked up when talking about science, and that can be very motivating during the long haul of graduate school. On a personal level, it has been very nice to have Hans and the rest of his family around for so many important events.

Through my five years of graduate school, there have been many others who have helped me develop or endure. First of all, my advisor Steve has been quite a source of motivation, that is in addition to taking all of the responsibilities of the role

of advisor that needs not be explained to anybody reading this text. It seems like almost every conversation I had with him resulted in me wanting to do some of the best science ever. There were several times I would go into a meeting with him feeling like Dave Stoler [from *Breaking Away*] working in his father's used car lot, and leave feeling like Dave on the last lap of the Little 500.

I have to give a shout out to JILA, where it is very easy to do science. There are so many people there whose main goal is to make the pursuit of knowledge seamless. I particularly enjoyed participating in OSEP, where I got to follow the progress of people in so many different groups. I can hardly imagine getting through grad school with nearly the perspective I have if it were not for everybody involved in OSEP. It has truly been an enriching experience to be involved in such an interdisciplinary group.

There are many others that deserve acknowledgement from me. We have to keep perspective though: this isn't the Oscars.

Table of Contents

List of Figures

List of Tables

Chapter 1

Introduction

Ultrafast phenomena comprise a vast field of study in chemistry and physics, with many types of applications, particularly the direct study of processes happening on sub-picosecond timescales. The short timescales inherent to ultrafast pulses correlate to a wide bandwidth in the frequency domain. During excitation, especially to a first order approximation, several transitions can often simultaneously become excited. In the case of dissipative or quasi-continuum systems, such as a solid state semiconductor or a repulsive molecular electronic potential, a predominant characteristic of the wide bandwidth excitation is a rapid decay of signal[1-3]. In an atom or molecule in the gas phase, the energy level structure can contain narrow bandwidth resonances, implying the presence of slowly decaying states. In the presence of resonances, the dynamics of ultrafast excitation can drastically change from a monotonic exponential decay to series of recurrences, or temporal interferences[4-8]. Thus, if more than one state is excited, a time dependent wave function, or wave packet, results. By defining a wave packet as a superposition of multiple states, a continuum process—such as molecular dissociation—represents the limit of wave packet behavior with an infinite number of component states, but in this case a wave packet consists of a limited number of states[1, 2, 4, 9-11]. In the presence of a limited number of transitions, an oscillatory behavior can show up in time as the time dependent wave function returns to a configuration in state space that is favorable for

observation. This regular recurrence of the wave function to a favorable configuration can be thought of as a re-phasing process. Once launched, the component states of the wave packet accumulate variable amounts of phase as determined by their energy and eventually they can all come into phase at some later time. This re-phasing time depends on both the number of states involved and their relative energy spacing, so it is not necessarily predictable.

The recurrence phenomenon of wave packets leads to the possibility of directing the wave packet's path as it travels through its configuration space and has come to be realized in many forms. Known as coherent control, this study of directing wave packet creation and propagation has seen attention in a wide range of systems from the relatively simple to the seemingly impossibly complex[9, 12-26]. Although early hopes that coherent control would be viable as a synthetic tool have yet to come to fruition, the process of performing coherent control can lead to a better understanding of many types of molecular and spectroscopic processes[22]. Many examples of coherent control have been implemented in the past, with one primary method of control revolving around manipulating the phase and amplitude of the component wave functions of a wave packet by manipulating the excitation laser source[16, 21, 27-31]. In effect, a laser is manipulated, and information from the laser is written onto the wave packet[32, 33].

This thesis addresses several aspects of using ultrafast pulse shaping to control both transient and stable wave packet dynamics. The dynamics to be studied are state resolved, allowing very precise investigations into the spectral

aspects of the dynamics of ultrafast excitation. Most of the studies involved in this thesis address the creation and propagation of precisely prepared wave packets. A wave packet is defined as a superposition of stationary state wave functions that displays time dependent dynamics. A basic description of a wave packet is included here, where the total wave function is a summation of component wave functions:

$$\Psi(t) \propto \sum_i c_i(t)\psi_i e^{i\omega_i t}, \tag{1.1a}$$

where n is a normalization constant, $c_i(t)$ is simply a weighting coefficient, and ψ_i is a component stationary state wave function, and the exponential factor is a time dependent phase factor that depends on the wave function energy. Since an observable consists not of a wave function but a modulus squared of the wave function over some coordinate, the above equation needs to be rewritten to reflect the qualitative act of observation:

$$|\Psi(t)|^2 \propto \sum_i \sum_j |c_i(t)\psi_i|^2 + |c_j(t)\psi_j|^2 + |c_i(t)c_j(t)|\cos(\omega_{ij}t), \tag{1.1b}$$

where ω_{ij} is the energy difference between states in a wave function, and the overlap integral between the component wavefunctions along an observation coordinate is assumed to be unity. In the above equation, the observable time dynamics come from the cosine term representing an interference between states, accounting for the "rephasing" processes mentioned above. In the weak field limit the non-transient weighting coefficients are expressed as

$$c_i \propto \varepsilon(\omega_{ig})\mu_{ig}, \tag{1.1c}$$

where the excited state coefficient depends upon both the transition dipole between the launch and excited state (μ_{ig}) and the electric field strength at the resonant frequency between the launch and target state [$\varepsilon(\omega_{ig})$]. Note that in the presence of an electric field, $c_n(t)$ can change but after an excitation pulse, these factors are effectively constant over timescales on the order of over a nanosecond. Various permutations of Eq. (1) will be invoked several times in the text, and additional details will be added in or expanded upon in the following chapters. The equations above show that, qualitatively, we observe wave packets that get stronger as the excitation laser gets stronger and that contain an oscillatory component in time. At the beginning of each chapter, a justification and a frame of reference will first be established, so that it will come as no surprise when a specific detail is included.

To begin, a summary of important experimental considerations will be considered in chapter 2. The summary will include a short discussion of the experimental setup, excitation scheme, and a somewhat detailed analysis of the limitations of the pulse shaping apparatus. This pulse shaper is very similar to a number of other pulse shapers and has been analyzed in the literature[30, 34], but since its use plays such a large role in many of the experiments of later chapters, a discussion is included. Another experimental technique, here referred to as Wavelength Subtraction Spectroscopy (WSS), is examined. This technique consists of looking at a signal as narrow bands within an ultrafast spectrum are attenuated. This is similar to observing an absorbance process, except

interference effects between different wavelengths in the ultrafast pulse can be examined with WSS.

Chapter 3 describes the use of an Evolutionary Algorithm (EA) to optimize several types of processes in the weak field limit (*i.e.* peak power $<10^{10}$ W/cm^2 in these experiments in Li_2). After a brief exposition of the routines used by the EA, a sample pulse compression is performed. In this case, the EA performs the same task as a pulse reconstruction algorithm in that it finds the spectral phase of an input pulse. This is followed by an optimization of weak field wave packet dynamics at times after the pump pulse is over, in effect addressing issues related to resonant absorption processes within ultrafast pulses. An optimization of transient weak field wave packets shows that during a pulse, various nonresonant processes can be controlled, as verified by the good agreement of a modeled optimization with experimental results.

Chapter 4 explores in more detail the limits of controlling transient population transfer processes in the weak field. It is shown that the spectrum of an ultrafast pulse can be divided into multiple spectral regions resulting in spectral channels, or groups of wavelengths, that can be used for ultrafast pulse shaping. Resonant and nonresonant effects are shown to be independently controllable, with the nonresonant effects providing the basis for controlling transient dynamics. Even though this sounds similar to Wavelength Division Multiplexing, it differs in that it really pushes the degree to which the control channels can be separated, and it takes advantage of nonresonant effects in a way not previously exploited.

Chapter 5 demonstrates a method for controlling the instantaneous phase of a wave function, as observed by a change in wave packet phase. This is a case of an application of the lessons learned in chapter 4. The observed dynamics are shown to transform a superposition of wave functions in a way that is consistent with a quantum computational Z-gate.

One of the limitations of the wave function manipulations described in Chapter 5 as applied to quantum computation is that the excited state superposition contains significant launch state character. One way around this coherence is to fully transfer the population out of the launch state. This is addressed in chapter 6 as a goal of strong field coherent control (with peak laser powers up to ~10^{12} W/cm^2), where significant launch state population depletion is possible. In this regime, Eqs. (1a-c) fail to describe the population dynamics, as it is seen that both the ground and excited state populations oscillate as a function of electric field strength. In a two level system, this population oscillation is known as a Rabi oscillation[5]. This chapter starts with a theoretical examination of wave packet dynamics in the presence of both a uniform electric field and a spatially Gaussian electric field. Finally, a chirped pulse Rapid Adiabatic Passage scheme is proposed and implemented to transfer population through specific excited states. Specifically, a Raman transition is excited such that the population that transfers through the E electronic states gets depleted to nearly zero along with the launch state. Stokes/anti-Stokes excitation is selected by simply changing the sign of chirp.

Finally, chapter 7 summarizes studies using a tunable ultrafast laser, with the ultimate goal of identifying energetic regions favorable to studying electronic wave packets. Chapter 7 begins with a study of wave packet dynamics between two bound electronic states. In this low lying Rydberg state regime, it is shown that quantum beats can be observed between individual states on the separate curves. Additional work verifies that the observations are of primarily rotational states, as progressions of rotational quantum beats for increasing vibrational quanta are observed. Within this vibrational progression of rotational beats lie additional coherences that are attributed to quantum beats between electronic states. It is shown that the electronic beats are between states with $\Delta\Lambda=1$, suggesting a potential handle for further controlling the wave packet dynamics via Stark shifting one state relative to the other. Chapter 7 concludes with a series of experiments exploring an ultrafast transient effect that is ultimately deemed to be atomic in nature. This final series of experiments is left with open questions to be revisited at a later date.

Chapter 2

Experimental Setup and Overview

2.1 Experimental Apparatus and techniques

In most of the experiments in this thesis, a three step excitation scheme is used to produce a time dependent photoionization signal, and hence observe time dependent wave packet dynamics as presented in the previous chapter. The experimental setup uses a cw launch state preparation laser to excite the transition for $A\ ^1\Sigma_u^+ \leftarrow X\ ^1\Sigma_g^+$, an ultrafast laser system to produce the pump and variably delayed probe pulses, a pulse shaping apparatus, a heat pipe containing the Li_2 sample, various detection apparatuses, and controlling software on a computer.

The laser system is pumped by an argon ion (Ar^+) laser operating at ~27 W, which pumps a cw dye laser for launch state preparation, and various ultrafast lasers, depending upon the experiment [see Fig. 2.1 for a sample excitation scheme]. The experimental laser setup will be discussed in more detail in the respective section where data will be presented, since the setup changes depending upon the experiment. Figure 2.2 summarizes the optical table layout, with notes where the laser setup is changed. In almost all cases, three lasers interact to produce photoions, and pump-probe experiments are performed. It is duly noted where the excitation scheme deviates from a three laser interaction.

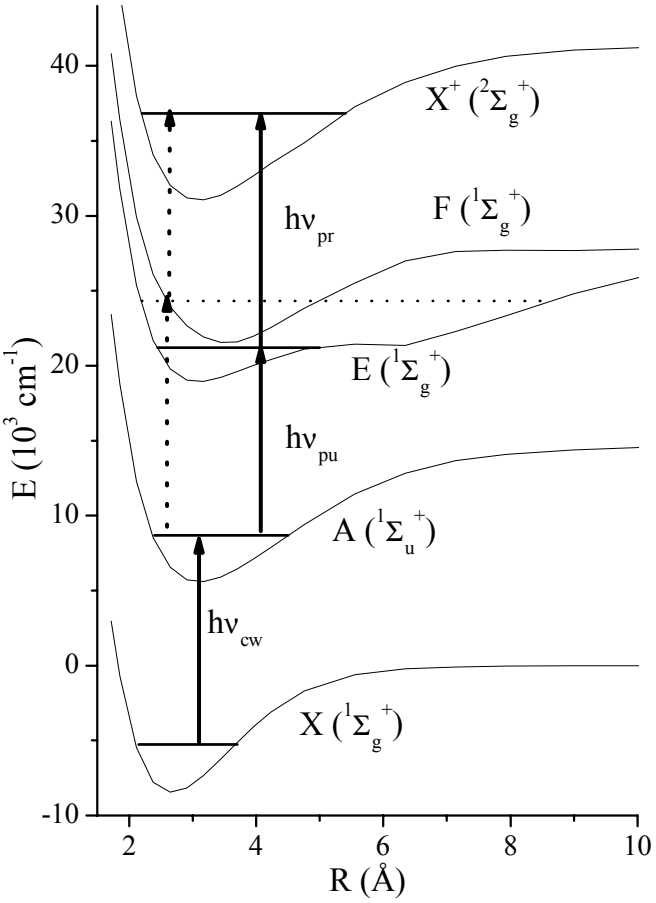

Figure 2.1: Typically excited potential energy curves in Li_2. In this scheme, the pump and probe pulses are of different colors. A cw laser excites from the X ($^1\Sigma_g^+$) electronic curve to a pure launch state on A ($^1\Sigma_u^-$). An 800 nm ultrafast laser excites a superposition of states on the E ($^1\Sigma_g^+$) curve, which is subsequently ionized by a time delayed 640 nm ultrafast probe pulse. At negative delays (dotted lines), the probe-pump pathway (for 640 nm probe pulse) through the F ($^1\Sigma_g^+$) state, as indicated by the dotted lines, has a much lower yield than the positive time pathway due to unfavorable Frank-Condon overlap factors. Note that in some experiments, as described in the appropriate chapters, the excitation scheme will deviate from above.

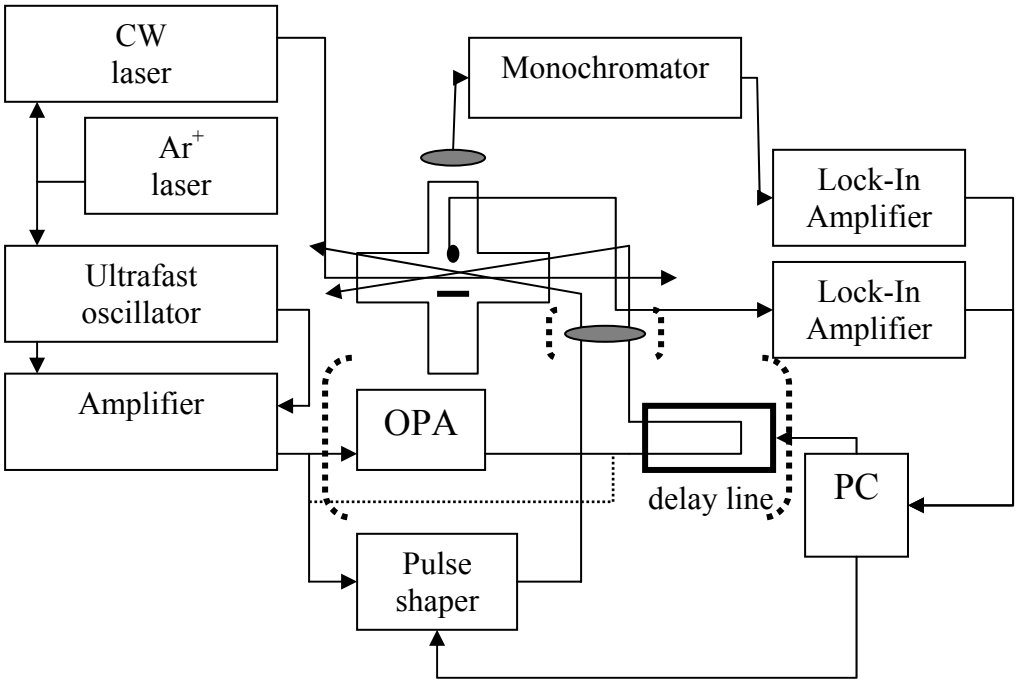

Figure 2.2: Schematic experimental setup. Sections in parentheses indicate changeable portions of the setup. The output from the regenerative amplifier is divided into up to two beams. One beam goes through the pulse shaper. This beam can be either the pump or probe pulse, depending on the pulse timing, but is actively shaped only in experiments where it is acting as the pump pulse. The second beam is either split unchanged or goes through the OPA to produce tunable ultrafast output from 500-700 nm. The ultrafast and cw beams intersect in the heat pipe which is equipped to detect ions and fluorescence. Focusing optics can be placed into the beam lines to increase peak intensity.

2.1.1 Pulse shaper

Since many of the experiments described in this thesis depend exquisitely on the manipulation of ultrafast dynamics by phase and amplitude shaping the spectrum of an ultrafast laser pulse, it is necessary to discuss the pulse shaping setup in some detail. The pulse shaper consists of a zero dispersion, four focal length imaging system, and uses a spatially addressable, double stack 128 pixel SLM between crossed polarizers, in a setup similar to that described by Weiner *et al.*[30] and Wefers *et al.*[29, 34, 35] In the Fourier plane, the pulse is dispersed linearly with respect to wavelength across the face of the SLM. Generally, the bandwidth of our pulses is dispersed across up to 40 pixels (FWHM) on the SLM. With a pulse bandwidth of 9 nm, this results in approximately 4 cm^{-1} per pixel resolution for frequency domain pulse shaping. By applying specific voltages to the pixels, we can manipulate the phase and amplitude of each wavelength of the pulse.

With a single frequency imaged to a spot size of 170 μm, the broadband pulses can be temporally shaped within a time envelope approximately 8 ps wide (referred to as the "pulse shaping window"), as derived previously [29] and observed experimentally. This envelope, which will be an important experimental constraint, is a result of both the sampling effects of the finitely sized pixels of the SLM and the finite spot size for each frequency component. To shift a pulse in time, a linear phase is applied across the pulse according to $\Delta t = d\varphi/d\omega$. The sampling aspect of the SLM gives an approximation to this formula to be

$\Delta t=\Delta\varphi/\Delta\omega_{pix}$ where $\Delta\varphi$ is the phase shift per pixel, and $\Delta\omega_{pix}$ is the difference in central frequencies imaged onto adjacent pixels. Because of wrap around of phases, a phase shift of $\Delta\varphi$ can also be represented as $\Delta\varphi+2n\pi$, where n is an integer. This produces replicas at $\Delta t=(\Delta\varphi+2n\pi)/\Delta\omega_{pix}$ and attenuates the shifted pulses with attenuation increasing along with Δt. Another limitation is the finite spot size: spatial overlap of more than one pixel by a monochromatic wavelength causes diffraction of certain wavelengths out of the beam. This is because the $\Delta\varphi$ between adjacent pixels introduces a certain amount of destructive interference. We thus see some destructive interference in the direction of propagation, as light that is produced with the multiple phases is diffracted out of the beam to maintain momentum matching conditions[29].

In many of the experiments here, we shape the pump pulse, and the electric field can be written as

$$E(t)=\sum_{i=1}^{128}\int_{-\infty}^{\infty}d\omega_i' \mid \varepsilon_i(\omega_i') \mid T_i^{1/2}\exp[i(\omega_i' t+\varphi_i)], \qquad (2.1)$$

where the summation is over all 128 pixels across the SLM, and $\varepsilon(\omega_i')$ is the amplitude of the electric field at the central frequency ω_i' on each pixel. The amplitude and phase controls over the pulse are included in the $T_i^{1/2}$ and φ_i terms, which represent the absolute value of the amplitude transmittance and applied phase, respectively. Without modulation, $T_i^{1/2}=1$, and $\varphi_i=0$. The $\varepsilon_i(\omega_i')$ term is approximately Gaussian, to reflect the spectrum imaged onto a single pixel, and it will be shown that this bandwidth is approximately 6 cm^{-1}, as opposed to the separation of central frequencies on adjacent pixels of 4 cm^{-1}. Note that the

integrals of adjacent pixels will have significant overlap, resulting in attenuation of the field when phase shifts between adjacent pixels are applied. In typical experiments, excitation is in the weak field, but some experiments will examine stronger field effects. In the experiments described in this thesis, peak electric fields range from 10^5-10^{11} W/cm^2, depending upon the experiment.

As an experimental demonstration of the capabilities of the pulse shaping apparatus, a series of phase locked pulses was generated. First, Fig. 2.3 shows the extent to which a phase locked pulse train can be created with our pulse shaping setup. It is evident from the figure that longer time delays between pulses means less intense pulses, as expected from the diffraction effect argument from above. The longest time delay between pulses of about 8.5 ps demonstrates a limit of pulseshaping. Notice that as the pulse separation increases, the pulse intensity decreases; diffraction due to phase shifts of adjacent pixels decreases the transmitted intensity of phase shaped pulses. In a phase locked pulse replica scheme, a phase grating with an alternation between 0 and π phase between adjacent pixels is applied to the SLM. This represents the maximum linear phase that can be applied. Any more than a π phase shift between adjacent pixels, because of wrap-around effect, will be equivalent to a smaller phase shift with the opposite sign. In later chapters, several instances of pulse-shaping will be cited, and the decrease in pulse intensity seen above will become important.

A second example of a pulse-shaping scheme can be useful for illustrating the limitations of our pulse shaper. Figure 2.4 shows a two-color pulse train,

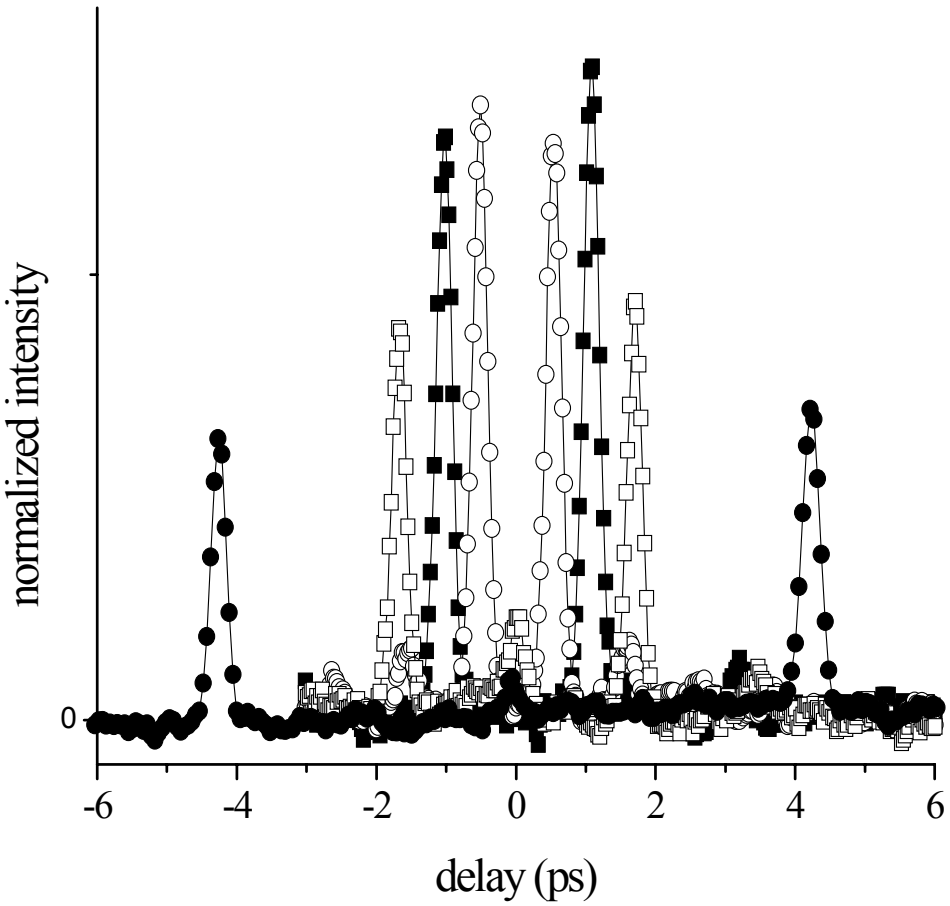

Figure 2.3: Cross correlation pulse profiles for pulse trains with various interpulse delays. The pulse trains are generated by the application of a phase grating of π*$round$[$\cos^2(2\pi p)$], where *round* indicates rounding to the nearest integer (0 or 1), and p indicates a number of pixels from 2 to 16, for the longest to shortest interpulse delay, respectively. The symbols represent scans for different delays between phase locked pulses.

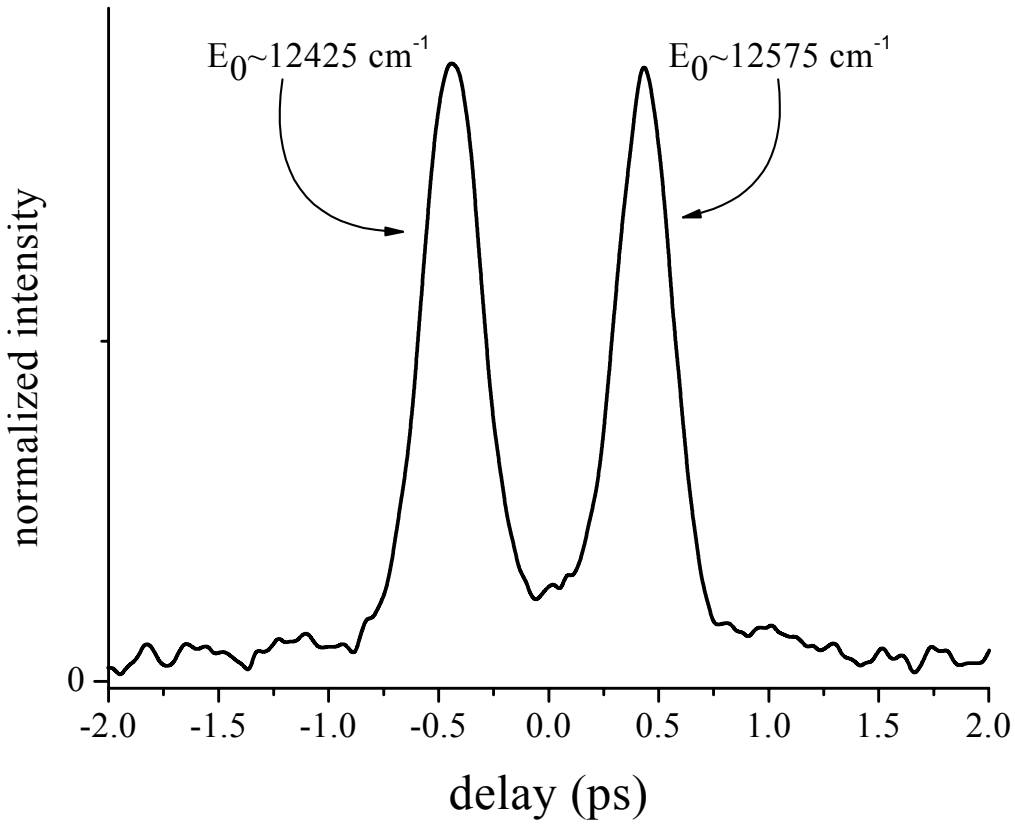

Figure 2.4: Multi-color pulse train. The pulse train was generated by applying opposing linear phases to the high ($E>E_{i0}$) and low energy ($E<E_{i0}$) halves of the input spectrum centered at E_{i0}.

where two phase related pulses are generated that each correspond to a different half of the input spectrum. The pulse train is generated by applying a linear phase $\varphi(p) = \pm mp$ where p is the pixel number and m is a constant. All wavelengths with a shorter than average wavelength get a positive slope to the phase, and those with a longer than average wavelength get a negative slope. The net effect of this is to create two pulses that are equally spaced around t=0 and have pulse durations approximately twice as long as transform-limited pulses. This pulse train is demonstrated here because of its potential importance in strong field control schemes such as stimulated Raman adiabatic passage (STIRAP)[36].

2.1.2 Heat pipe/detection

The lithium dimer sample is contained in a static heat pipe, which is operated at 750°-800° C, with an argon buffer gas pressure of between 1.0 and 3.5 Torr, depending upon the experiment. The lithium atom pressure at this temperature is approximately 1 Torr (130 Pa), which will give a Li_2 pressure of approximately 0.02 Torr (2.6 Pa). The lasers intersect between two parallel plate electrodes that are separated by 1 cm with 10 V applied across them. The current generated by the ionization of the molecules is measured by a lock-in amplifier, which is synchronized to the modulation of the cw laser at 750 Hz by a mechanical chopper. This technique gives a maximum single scan signal-to-noise ratio of up to 10:1.

Signals are generally normalized to the fluorescence from the launch state. This is accomplished by observing fluorescence in a perpendicular geometry [see

Fig. 2.2]. All fluorescent light within the small solid angle bounded by a 2" collection lens is imaged onto a fiber-optic bundle. This fiber bundle then couples into a monochromator, and the light for a specific transition [e. g. A(11, 28)→X(2, 29)] is detected with a photomultiplier tube driven at 950 V. The output voltage is then filtered with a lock-in amplifier, and the photoionization is divided by the fluorescence in real time. The net effect of this is that drift in the power or wavelength of the cw laser becomes less important.

2.2 Wavelength Subtraction Spectroscopy

One of the main traits of ultrafast lasers that separates them from other pulsed or continuous wave (cw) lasers is the wide spectral bandwidth inherent due to the Heisenberg Uncertainty Principle. Since the ultrafast lasers occur on such a short timescale, they are characterized by a wide spectral bandwidth. In studying any sort of ultrafast transition, this wide bandwidth can affect the dynamics of the transition. CW absorption spectroscopy can to a certain extent give complete information describing a transition, but interactions between wavelengths can be lost. As an alternative, Wavelength Subtraction Spectroscopy (WSS), where a transition is measured with a spectral notch in the excitation spectrum, can be used to look at the relationship of different frequencies in an excitation by an ultrafast pulse. This becomes especially important in examining either strong field or phase shaped pulses.

To study the effects of the wide bandwidth on a transition, there are several methods one can use. The first, and perhaps most obvious, is to perform a

variant of tunable cw absorption spectroscopy, where a laser is tuned and absorption is measured, giving an absorption linewidth, followed by performing an Inverse Fourier Transform to infer the time dynamics. In this regime, the signal will simply be a summation of the single frequency components in the signal:

$$S = \left| \int d\omega A(\omega) \right|^2 \tag{2.2}$$

where $A(\omega)$ is simply the signal amplitude—such as an excited state coefficient—expected for any single exciting wavelength; time dependence is implied. For the case of a two state wave packet, it can easily be inferred that the two states interact if coherently excited, so that $S=|A(\omega_1)+A(\omega_2)|^2$, but as an excitation gets more complex, making inferences such as this get more and more complex, as well.

In contrast, WSS can give direct information about the nature of an excitation. As implemented in our experiments, one pixel at a time is blocked on the SLM, as shown in Fig. 2.5. For each gathered data point, the signal is characterized by the following:

$$S_{WSS}(\omega') \propto \left| \int_{\omega} d\omega A(\omega) - \int_{\omega'} d\omega' A(\omega') \right|^2 \tag{2.3}$$

where the integration over ω is the base spectrum, the integration over ω' is the subtracted part of the spectrum, and again $A(\omega)$ is a frequency dependent amplitude with the time dependence implied. The crucial difference between this spectrum and what one would expect from a cw type experiment is that there are now cross terms between the frequency components ω' and ω:

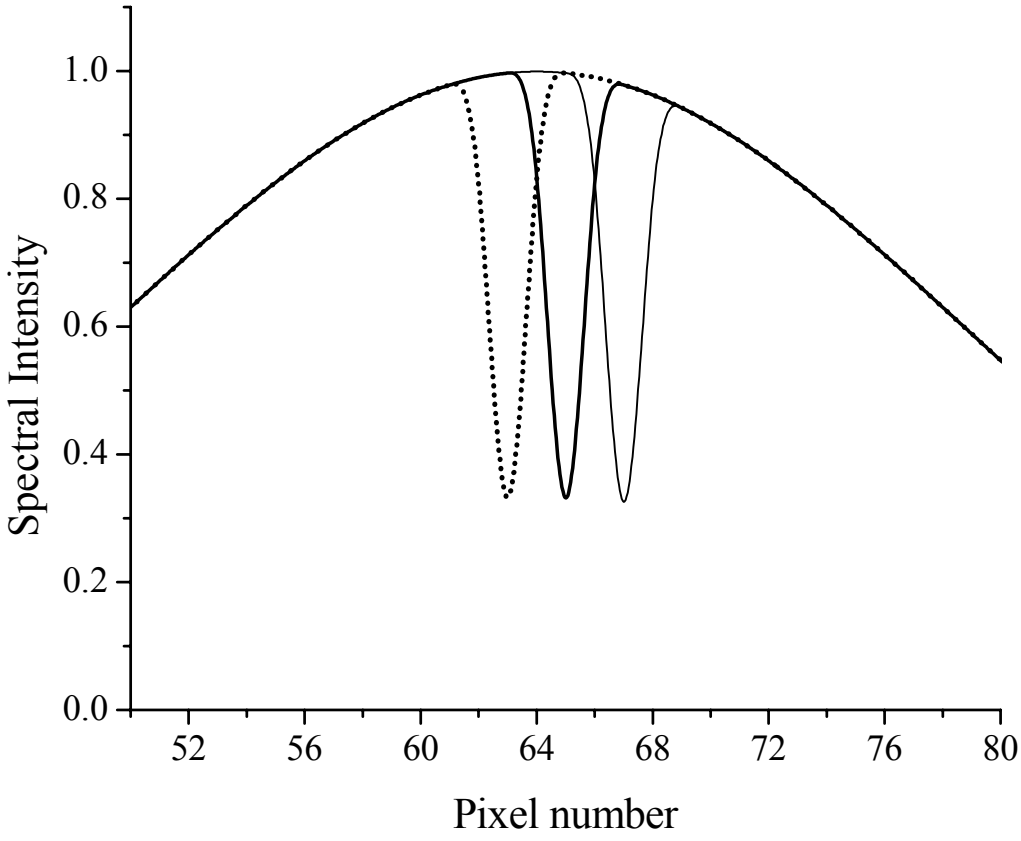

Figure 2.5: Schematic spectra as used in Wavelength Subtraction Spectroscopy (WSS). A signal is acquired for each spectrum as one single pixel at a time is blocked. In the experiment, the light on each pixel is completely attenuated, but when the SLM mask is converted to wavelength units, a single frequency is not completely attenuated due to focusing effects. Three wavelength spectra are shown in the figure as pixels 63, 65, and 67 are sequentially blocked.

$$S_{WSS}(\omega') \propto$$
$$\int_{\infty} d\omega |A(\omega)|^2 + \int_{\infty'} d\omega' |A(\omega')|^2 - \int_{\infty}\int_{\infty'} d\omega d\omega' [A^*(\omega)A(\omega') + A^*(\omega')A(\omega)]. \quad (2.3b)$$

In a case where there is only one resonance present, and the field is weak, the cross terms are significant only when ω and ω' are resonant frequencies[7]. In the two resonance case mentioned above, the only cross term is where ω and ω' represent the two resonant frequencies, and it only modulates the depth of the signals. In more complex cases, the cross terms can become numerous, drastically changing depth and width of the observed signal. New information, including the amplitude of an excitation relative to all other excitation pathways, can now be extracted from a simple spectrum. Since, in pulse shaping schemes, interferences between spectral pathways are often invoked to manipulate a system, this technique gives a measure of the interference (see chapter 5).

To illustrate, Fig. 2.6 shows a comparison of the two cases for examining an excitation at a specific time during an excitation of a two level system. In both cases, the same phase mask is applied to the SLM. In one case, it is assumed that the SLM *transmits* the light from only one pixel at a time, and in the second case, it is assumed that the SLM *attenuates* the light on one pixel at a time. A perturbative calculation is then performed to find an excited state population at a transient time (details of the calculation procedures are presented in chapter 6). The main result to be considered here is that the two types of spectroscopies present qualitatively different results under certain conditions. WSS is basically a type of optical heterodyne detection. In WSS, phase information is gleaned from the signal since the data is gathered with a certain coherent background, as

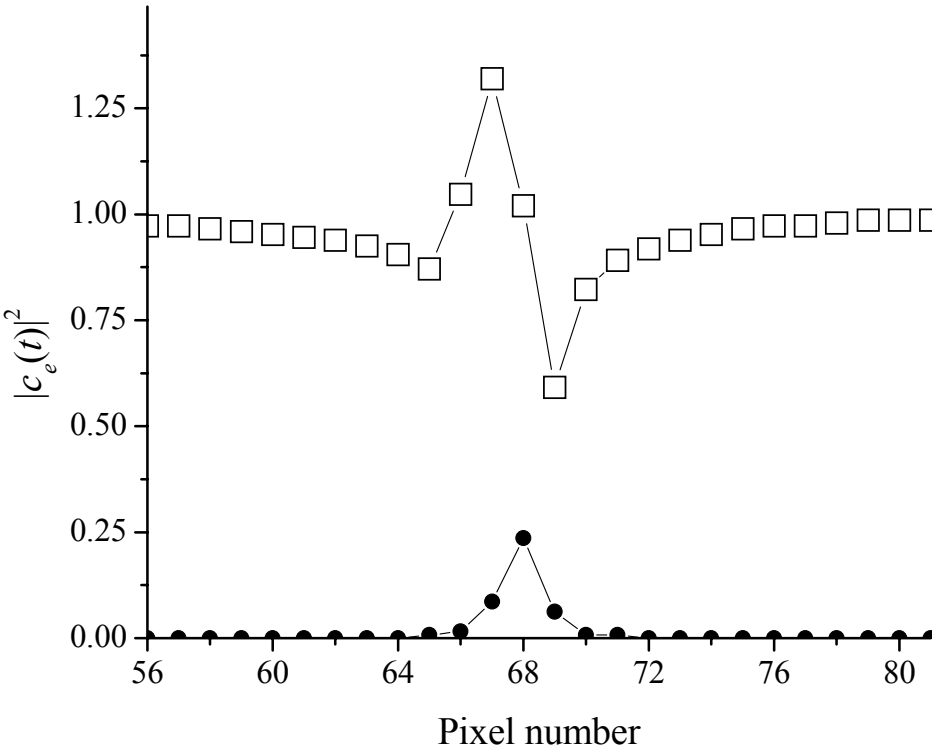

Figure 2.6: Comparison of excited state populations for a weak, phase shaped input using narrow bandwidth excitation and WSS. The dots (●) represent the calculated excited state population at t=0.0 ps with an excitation laser bandwidth equal to the spectrum imaged onto a single pixel of an SLM, scanned pixel by pixel. The squares (□) represent the calculated excited state population at t=0.0 ps using the WSS method. In both cases, an identical phase mask is used.

represented by all other frequencies in the full pulse. In following chapters, the WSS spectroscopic technique will be used in both the limited-cross-term regime and the highly coupled regime.

Chapter 3

Evolutionary Algorithm

3.1 Introduction

Ultrafast laser sources are promising new tools for research in the area of coherent phase control[15, 25]. The wide bandwidth inherent to these lasers is conducive to detailed manipulation of the amplitudes and phases of the fields that interact with the system of interest. Several pulse shaping techniques employ frequency domain manipulations to generate a desired field[26, 30, 37]. These methods provide a large number of amplitude and phase parameters by dividing the frequency bandwidth into numerous segments and adjusting the phase and amplitude of each frequency component of the pulse. Directing a system response from such a complex parameter space can be tedious, even if a detailed mechanistic knowledge of the system is known[13, 38]. Learning algorithms have thus far proved to be an advantageous way to control a physical process to generate desired photo-induced products, and these algorithms can be implemented with little a priori knowledge of the system of interest.

There are several recent applications of learning algorithms (such as evolutionary or genetic algorithms or simulated annealing) to find optimal solutions to various physical problems[20, 25, 26, 39-41]. Three main aspects of these algorithms have been studied in the context of chemical physics: (1) the ability to control molecular processes[20], (2) the methods for reaching the

optimized solution[25, 39], and (3) what can be learned about a physical process from the form of the optimized driving laser field[39]. The benefits of using these algorithms to glean physical information from an unknown system have been difficult to realize, and thus far they have been limited to evaluating just a few parameters such as degree of chirp or pulse train timing[20, 39]. Additionally, few examples exist that address concepts such as the competition between optimization pathways or motion through solution spaces. The effect of manipulating physically irrelevant parameters has been addressed only on a limited scale. This chapter will take these considerations a step further by applying a simple evolutionary algorithm to a system with variable complexity, illustrating multiple mechanisms at play simultaneously and evaluating non-contributing parameters.

This chapter will primarily examine optimization conditions for the preparation step of a wave packet in lithium dimer followed by ionization of the wave packet. The Li_2 $E\ ^1\Sigma_g^+$ state has been studied both spectroscopically and through wave packet dynamics.[7] Here we use phase and amplitude manipulation of an ultrafast preparation pulse to control a wave packet on the E state with learning algorithm optimizations of the ionization probability by a time-delayed probe pulse. Wave packets composed of either two or ten rovibrational states are investigated. The physical processes for one optimization condition involve using only a limited number of wavelengths, and in the second involve optimization of the entire spectrum of the preparation pulses. Actual wave packet traces will be compared to frequency domain solutions to help identify

optimization mechanisms and to show which mechanisms become optimized first. It will be shown that non-resonant wavelengths play a role in photoionization even in the weak field limit, but only at pump-probe time delays when the preparation pulse may temporally overlap the probe pulse.

Sections 2 and 3 of this chapter will provide a characterization of the optimization routine used in the experiments in this and subsequent chapters. A simple pulse compression calculation will be examined in order to performed to perform an analysis of what can be learned about the physical system from the dynamics of the EA operations. Section 4 will show an experimental implementation of the pulse compression calculation of section 2. Section 5 will show experimental results of an optimization of wave packet dynamics under the restriction that transient phase and amplitude effects can not play a role in the optimization. It will be shown in this section that only resonant wavelengths play a role in the dynamics of long time wave packets in the weak field regime. Sections6-8 will show a similar optimization as in Section 4, except transient phase and amplitude effects will both be optimized. Included in this section is a modeled optimization using first order time dependent perturbation theory. Finally, an optimization of the photoionization at 0.0 ps will be analyzed. The solution of this final optimization will form the basis for the work of upcoming chapters.

3.2 Algorithm characterization

The experiments described in this chapter use a multiple membered evolutionary algorithm (EA), similar to several that have been used before[3, 23,

25, 26, 42, 43]. The EA begins with a population of 25 random SLM phase patterns (128 phases each), called individuals. The EA assigns each individual a fitness value proportional to the total ionization signal at a specific pump-probe time delay, then reproduces the fittest individuals and operates on the new population. The process is repeated with each new population until a stopping condition is reached [usually simply a pre-determined number of generations]. In general, any number of operators, or population manipulators, can be used to achieve optimal configurations[43], among which can be both time and frequency domain mutation, crossover, smoothing, averaging, and many others specific to a physical system of interest[25, 40, 41]. In the experiments described here, only mutation is used significantly.

The algorithm used here consists of an elitist reproduction method, followed by a simple mutation operator, as shown in Fig. 3.1. All specific parameters below were found to both quickly and reliably optimize a pulse compression [see section 3.3], so these parameters are used in all optimizations. The reproduction method used here chooses the top 24% of the population, ranked according to their fitness, and propagates them to the next generation. The proportion of the subsequent generation that descends from a particular individual is further weighted according to the rank, R (R=1, 2, 3,…), of the parent, giving the number of children descended from a single individual as approximately $8(R^{-0.6})$. Individual pixels are chosen at random from among the entire new population regardless of individual and are mutated. Approximately one in

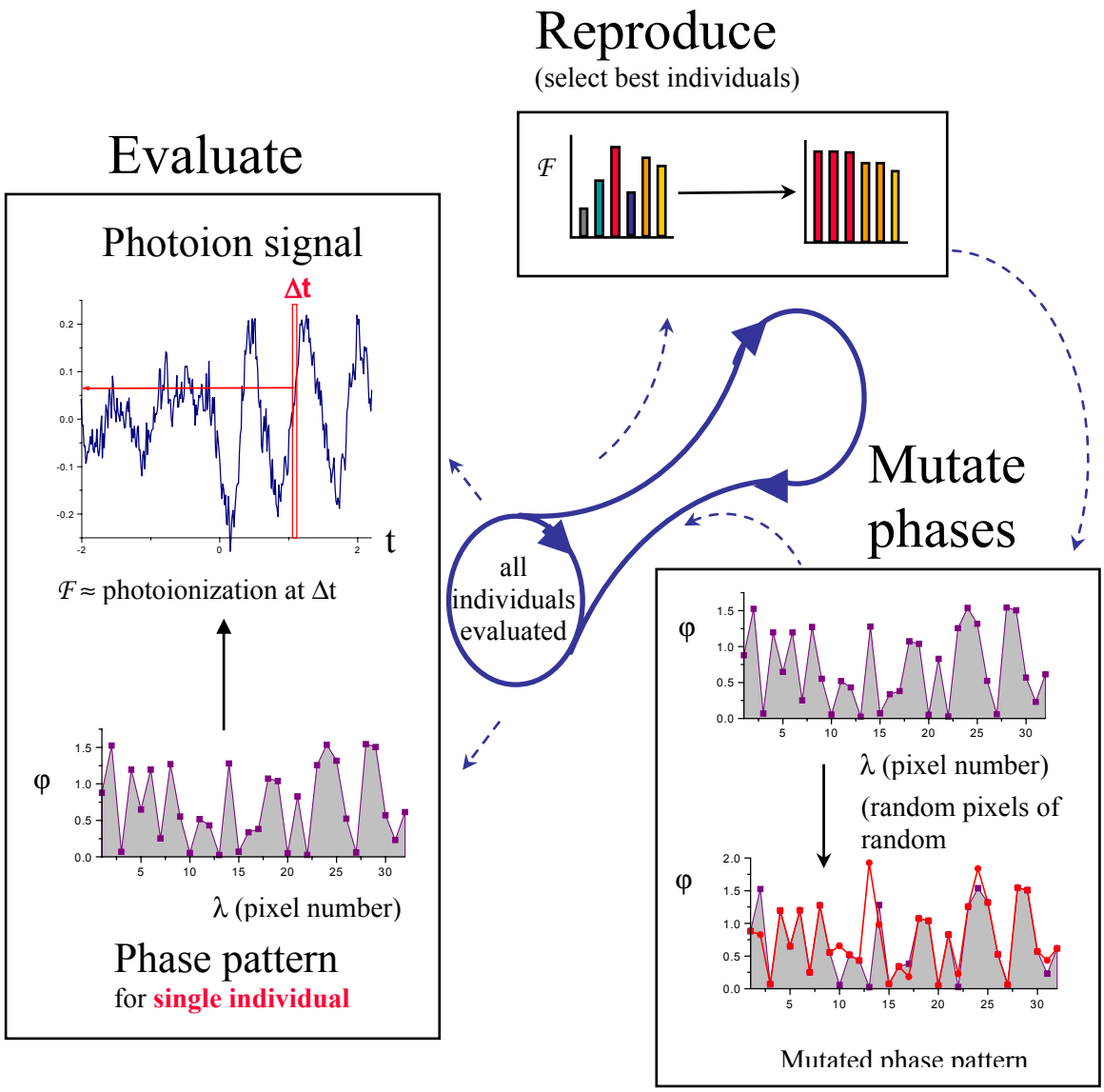

Figure 3.1: Evolutionary Algorithm Flowchart. First, a population of *individuals* consisting of phase masks is created and evaluated. The best individuals are reproduced then mutated. This procedure is repeated until a suitably optimized condition is met.

twenty pixels gets mutated each generation. Here, mutation means that a random phase is added to the phase already on a pixel. The random additional phase is generated according to a normal distribution about zero with a distribution width that goes as the generation number to the -0.75 power, or $\delta\varphi = A(G^{-0.75})$, where $\delta\varphi$ is the standard deviation of the mutation amplitude for a single generation, A is a constant phase (pre-determined to be about 30^{o}), and G is the generation number. This rate of mutation proceeds the same throughout all the optimization experiments so as to act consistently on different systems. The complexity of the EA is kept to a minimum for ease in interpretation of the optimization dynamics. Additionally, physical intuition concerning the well characterized Li_2 system is usually left out of this EA to better simulate the experimental conditions for optimizing unknown processes. The lack of physical intuition written into the EA has the tradeoff of longer convergence times, but the simplicity of the process facilitates interpretation of solutions during optimization.

The fitness function is simply the ratio of an individual's total ionization signal to a reference: $\mathcal{F}(i) = S(\tau, i)/S(\tau, 0,)$, although later experiments not included here use more complex fitness functions[6]. The pump-probe delay is set to a single delay (τ), and the total chopper-modulated ionization signal (S) for each individual (i) is monitored. To correct for experimental instabilities, each fitness value is normalized to a signal generated by an unshaped pump pulse [$S(\tau, 0)$], probed at the same delay. The simplicity of the fitness function can give insight into the physical processes being optimized. As individual pixels that have relatively large effects on the total ionization signal are manipulated, there is a

correspondingly large change in the fitness function upon optimization, so these pixels are the first to be optimized.

The actual signal is the average current generated by the fixed delay pump and probe pulses. Typically, each individual is evaluated for 0.5 seconds, resulting in a maximum coherent oscillation signal-to-noise ratio of 10:1. Occasionally, individuals are evaluated for up to 4 seconds each. When computation and system control times are taken into account, a single generation with 0.5 second averaging takes 40 seconds. When the EA has nearly converged, the 10:1 signal-to-noise ratio masks the differences in the individuals, so that is when a longer averaging time might be used. There are advantages to averaging for shorter periods since low frequency drift in the cw preparation laser has been observed to change the signal on a timescale of approximately a half hour. This will have little effect on the relative fitnesses of individuals within a single generation, but it may affect the average fitness of one generation with respect to another.

3.3 Convergence speed and schema size

One of the advantages of having a fitness value that is linearly related to the physical observable is that when coupled with a simple optimization routine, predictable optimization dynamics can be observed. It is intuitive that optimization of a complex parameter space would take longer to converge than the optimization of a very simple parameter space. It has been empirically observed that the simple EA used in the experiments described here does indeed take a shorter time to converge for problems of reduced dimensionality.

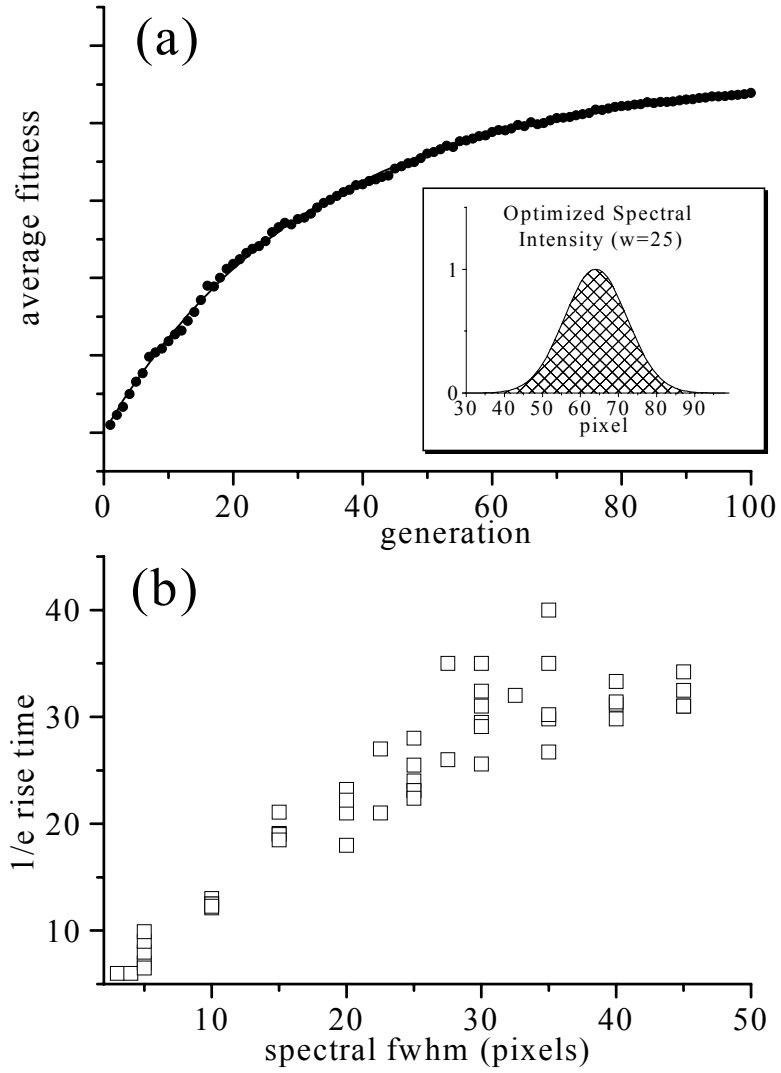

Figure 3.2: Calculated pulse compression dynamics using an evolutionary algorithm, according to Eq. (3.1a) in text. Panel (a): average fitness ($\mathcal{F}$) versus generation number (●) and single exponential rise fit for the inset pulse with 20 pixel FWHM Gaussian spectral profile. The fit has a 28 generation 1/e rise time. Panel (b): relation between model spectral FWHM and optimization rise time. This shows that the more pixels required for the optimization, the longer it will take to reach the optimum.

Evidence for the processes occurring in the physical system can be inferred from the dynamics of an optimization by this simple EA. To illustrate, first we examine the effects of changing schema—*i.e.* groups of pixels that are coupled and physically relevant, or active—on the time required to optimize a certain fitness value. Different processes can be seen by examining the widths of independent schema that are being optimized. For example, optimizing a non-transient incoherent ionization signal for a single quantum state on the $E^1\Sigma_g$ surface requires an optimization of approximately two pixels. The fact that there are two relevant pixels can be attributed to an effect of the single frequency spot size on the SLM being approximately Gaussian and 1.7 pixels wide.

The dynamics of this EA have been studied using a simple model of our current system, as illustrated in Fig. 3.2. In the model, the same EA is used as under experimental conditions, with the determination of the fitness value being the only difference. A few different processes are modeled to generate a fitness value ($\mathcal{F}$), one mimicking a pulse compression, $S(t)_{pc}$, and one mimicking a two state wavepacket optimization, $S(t)_{wp}$, whose form is based on perturbation theory:

$$S(t)_{pc} = |\Sigma_j a_j \exp(i(\omega_j t+\varphi_j))|^2 \tag{3.1a}$$

$$S(t)_{wp} = |\Sigma_k(c_k \exp(i\varphi_k))|^2+|\Sigma_l(c_l \exp(i\varphi_l))|^2$$

$$+|\Sigma_k(c_k\exp(i\varphi_k))||\Sigma_l(c_l\exp(i\varphi_l))|\cos[(\omega_{0c}-\omega_{0(c-10)})t+\varphi_{0c}-\varphi_{0(c-10)}] \tag{3.1b}$$

$$a_j = \exp[-(2/\log(2))(\omega_j-\omega_{0a})^2/w^2] \tag{3.1c}$$

$$c_k = \exp[-(2/\log(2))(\omega_k-\omega_{0c})^2/n^2] \tag{3.1d}$$

$$c_l = \exp[-(2/\log(2))(\omega_l-\omega_{0(c-10)})^2/n^2] \tag{3.1e}$$

where ω_j (ω_k) is the central frequency on pixel j (k), φ_j (φ_k, φ_l) is the phase applied to light on pixel j (k,l), ω_{0a} is the central frequency of the pulse, w is the pulse FWHM in pixels, ω_{0c} and $\omega_{0(c-10)}$ are the frequencies resonant with transitions to the wavepacket states, φ_{0c} and $\varphi_{0(c-10)}$ are the phases applied to those frequencies, and n is the resonant frequency imaged spot size (in pixels). In Eq. (3.1b), the summation factors with the square of the same index account for the incoherent ionization signal, analogous to the a_i term of Eq. (3.1c), and the cosine term accounts for the coherence between wave packet states. They include variable resonant linewidths and the fact that phase jumps between adjacent pixels on the SLM result in some light being diffracted out of the beam. These equations have been normalized so that at their maxima, $S(t)_{pc}$ and $S(t)_{wp}$ have equal amplitude. For simplicity, all models have a pump-probe delay set to t = 0, and the wavepacket state spacing is assumed to be 10.0 pixels. The integrals over the range ω=- ∞ : ∞ from Eq. (2.1) have also been left out of the above equations, resulting in a sampling of the wavelengths on each pixel, giving the summation expressions.

Using Eq. (3.1a) as the model system response [i.e. $\mathcal{F} = S(t=0)_{pc}$], we investigated the effect of the schema size (w from equation 3.1c) on the convergence to the optimum. As shown in Fig. 3.2a, the convergence of a single optimization to the final solution fits very well to a single exponential decay. As w is varied, the decay time does increase as seen in Fig. 3.2b, although the correlation between schema size and decay time is not analytical. One conclusion that can be drawn from this data is that “inactive” pixels have minimal effect on

the EA optimization dynamics. The constant rate of selection of pixels to be mutated assures that this is the case. In every physical case, each active pixel has the same probability of being mutated each generation, regardless of how many other pixels are involved in the EA. These experiments were conducted on various spectral profiles (i.e. Lorentzian and square spectra) and qualitatively similar results were found, with only slight deviations from exponential decay seen in the evolution of the fitness functions, and increasing optimization times for increasing spectral widths.

In this case of pulse compression, every pixel that is involved in the optimization depends on every other one, so there is a high dependence of each pixel's phase on all of the other pixels' phases. This is in contrast to a situation where there are groups of optimized pixels that do not interact, or that interact minimally. One intuitive case of this would be to optimize average laser power, which is simply the sum of the intensities of all laser frequency components. Expressed algebraically (from eq. 3.1a), $|\Sigma_i a_i \exp(i(\omega_i t+\varphi_i))|^2 \neq \Sigma_i a_i^2$, which indicates that the maximum intensity expression contains cross terms between pixels [*i.e.* $|a_i a_k|\cos(\varphi_i-\varphi_k)$], and the average intensity does not. The presence of the cross terms defines the pulse compression as a single process that tries to make $\varphi_i=\varphi_k$ for all i and k, whereas optimization of average power is more of a series of "independent" parallel processes, each process being the optimization of a single spectral amplitude component. The effect seen would be that the optimization of peak intensity will occur more slowly than for average power.

A multiple mechanism optimization was modeled by including both Eqs. (3.1a) and (3.1b) in the optimization [i.e. $\mathcal{F} = S(t=0)_{pc} + S(t=\infty)_{wp}$]. Although this particular case is a highly simplified example of the true $S(t)_{wp}$, it is still instructive for showing the dynamics of multiple embedded processes. As the width (n in eq. 3.1d) of the wavepacket absorption schema increases for this multiple mechanism process, we see that there is a transition in the dynamics of the optimization from double exponential to single exponential behavior. The solid line in Fig. 3.3 shows the evolution of the average fitness function for a simultaneous optimization of a pulse compression with a 30 pixel FWHM schema size and a wave packet with two schema of 1.5 pixels each. In this curve, the average fitness $\mathcal{F}_{avg}(g)$ increases quite quickly in the first few generations, then follows a different exponential decay to the optimum, for a form $\mathcal{F}_{avg}(g)=a_0-a_1\exp[-g/g_1]-a_2\exp[-g/g_2]$. The two lifetimes ($g_1$ & g_2) in the double exponential correspond to schema sizes expected from Fig. 3.2b. This effect will be most pronounced when the interacting schema are of vastly differing sizes. As the processes become more comparable in schema size and interaction, the separability of the two components in the optimization, and hence the fitness, is not apparent. Another instructive trait of the EA is that in this case of two largely different schema sizes, the leading coefficients (a_1 & a_2) correspond to the relative influence of the two processes at play. Since the offset at g=0 is not necessarily 0 in experimental cases, information can only be gathered from the ratio of the two coefficients. In the calculation of Fig. 3.3, the two leading coefficients are both very nearly 1.0, as is expected from this analysis.

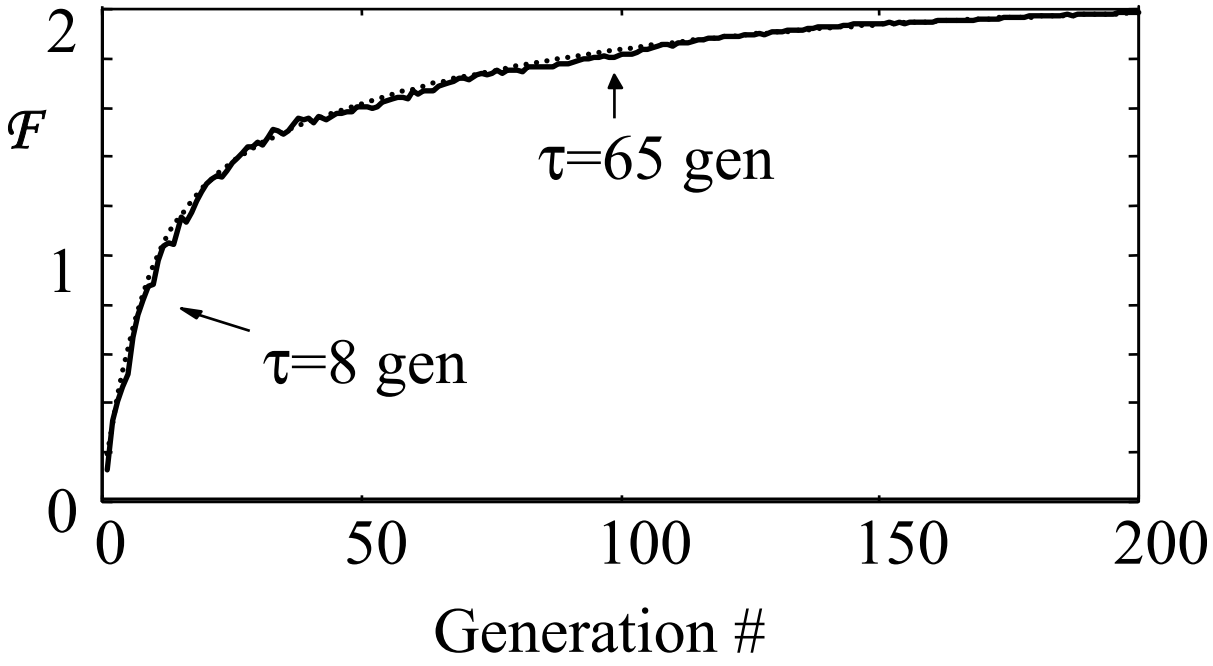

Figure 3.3: Optimized fitness ($\mathcal{F}$) of a two part process showing double exponential behavior. The optimization (solid line) consists of one small schema size process embedded in another larger schema process. The average fitness as a function of generation number was fit with a double exponential (dotted line).

3.4 Pulse compression

As a simple test case, a pulse compression of the pump pulse was carried out, similar to work previously done in other groups[3, 28, 44]. The motivation for performing this experiment is twofold. First, the intuitive dynamics of a pulse compression makes the mechanism of optimization by the EA easy to grasp—we are minimizing an intrinsic phase profile. This makes it easy to verify that the EA is actually performing as expected. A second motivation is that the optimized pulse compression phase mask contains information about the phase applied by nonidealities in the pulse shaping optical setup. The EA optimization acts as a type of analytical instrument for understanding our input pulse's phase function.

The experimental procedure is as follows. First, the pulse shaping setup is slightly misaligned so that it induces a small amount of dispersion into the pump pulse. This slightly modified output pulse and the reference pulse are then focused onto a GaAsP photodiode (bandgap~14,000 cm^{-1}) and the peak in the two-photon absorption signal as a function of interpulse delay is found. Next, the EA is allowed to run as described in the previous section with 32 effective pixels (each group of 4 pixels is treated as a single unit), with the pump-probe delay set to the peak in the signal as found with the unoptimized pump pulse. The total raw current from the photodiode is the fitness. Since the raw current is the cross correlation signal, the fitness $\mathcal{F}$ at τ=0 is proportional to the following, assuming no saturation of the signal:

$$S(\tau) = \int_t \left|E_{pu}(t)\right|^2 \left|E_{pr}(t-\tau)\right|^2 dt \qquad (3.3)$$

where *pu* and *pr* correspond to the optimized pulse and the reference pulse, respectively [these are the same as *pump* and *probe* in the rest of the text]. Assuming that the reference pulse is either transform limited or contains only linear chirp (quadratic phase versus wavelength), the greatest signal will correspond to the optimized pulse being transform limited. The EA searches for a solution that compensates for any intrinsic phase on the pulse to be optimized.

After performing the optimization as described above for 50 generations, the cross correlation time was indeed reduced slightly from the unshaped case, as shown in Fig. 3.4. The cross correlation of the unshaped pulses with the reference pulse was approximately 331 fs FWHM, and the optimized cross correlation showed a FWHM of 316 fs. This change is indeed small, indicating that the pulse shaper imparts a small degree of chirp in these experiments. The overall amplitude of the cross correlation is not quite as high as in the unshaped case, which is attributed a limitation of the EA. The reduced timescale of the optimized pulses shows that the overall signal response deviates slightly from Eq. (3.3). In contrast to most experiments, here we did not adjust the alignment of the pulse shaper to minimize the intrinsic dispersion it adds, so we can assume that the added phase in the experiments described here represents a maximum expected added phase.

The optimized phase pattern contains information that can be helpful for analyzing the pulse shaper output. Assuming the reference pulses are transform limited, the optimized phase pattern essentially extracts identical information (within a factor of -1) as a frequency resolved optical gating (FROG)—a phase

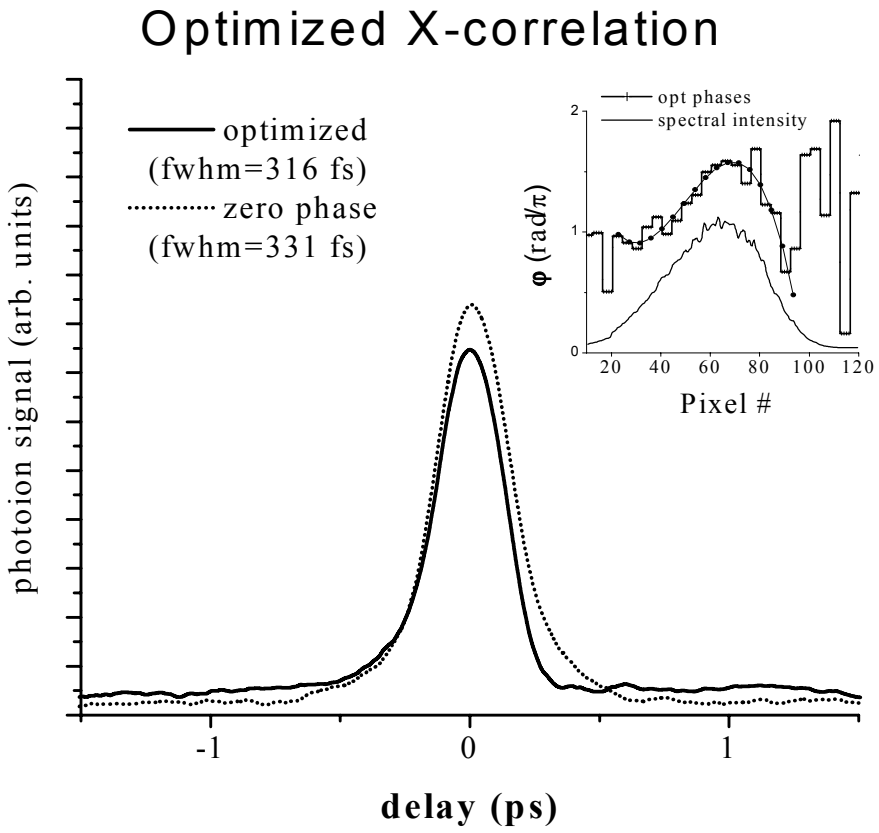

Figure 3.4: Optimized cross correlation. The dotted line is the cross correlation for an unshaped pulse, and the solid line is the cross correlation for the shaped pulse. Notice the small decrease in pulse length in the optimized case. The inset shows the optimized phase profile (+) and fit (●) along with the pulse spectrum.

and amplitude spectrum of the pulses to be studied[45]. Since a cross-correlation, instead of auto-correlation, technique is used, there is no time ambiguity characteristic of several FROG techniques[45]. At t=0.0 ps, the output from the pulse shaper can be rewritten as the following based on Eq. (3.1a):

$$|E(t=0)|^2 = |\Sigma_j a_j \exp(i\varphi'_j)|^2 \quad , \tag{3.4}$$

where φ'_j refers to the intrinsic phase applied by the pulse shaper apart from that intentionally added by the SLM. To maximize the output, the negative of the intrinsic phase must be applied, so that the depleting phase contributions are minimized, or $\varphi_{intrinsic}(\omega)-\varphi_{optimized}(\omega)=C$, where C is a constant. The optimized phase mask in the inset of Fig. 3.4 compensates for the intrinsic phase imparted by the pulse shaping assembly. A fit to the data between pixels 25 and 95 (where there is input intensity) shows an intrinsic group velocity dispersion (GVD) from the pulse shaper of D_v of -577 $fs^2 \pm 100$ fs^2, which was calculated based on a fit to the data of $d^2\beta/d\omega^2=0.0033*(\Delta pixel)^2$, where $D_v=-2\pi d^2\beta/d\omega^2$[46]; the third order dispersion is calculated to be approximately -102 fs^3 based upon the same polynomial fit. The lack of observed high order dispersion distortions such as pulse replicas in the cross correlation verifies a small maximum error (~20 fs^2) due to reference pulse distortions; the large GVD error is approximate and results from the assumption in the fitting procedure that all pulse distortions are characterized by second and third order dispersion. A second order only fit gives

D_v=-347 fs^2. This data fits well with the observation that the cross correlation FWHM was decreased by 15 fs. Using the EA as an analytical tool has proven to be useful for later interpretations, setting a benchmark for how much chirp to expect on our input pulses.

3.5 Optimizing launched wave packet

To analyze the EA even further, we optimize the relative phases of the two eigenfunctions in the two state wave packet. By setting the pump-probe delay to a time outside of the temporal pulse shaping region, we can optimize the wave packet signal without concern for the temporal shape of the ultrafast pulses. The advantage of this is that the system responds only to two resonant frequencies. This permits quantification of the relative accuracy of the EA, and the results are straightforward to interpret. Additionally, an optimization of the ten state wave packet, also at long time delay, will be briefly discussed. This multiple discrete state wave packet will show a more obvious global maximum of the photoionization signal than the phase shifting of a single beat, while still requiring manipulation of only resonant wavelengths.

First, we analyze the two state wave packet, which has a beating period corresponding to a 42 cm^{-1} (or 11 pixel) energy separation between the eigenstates. In Fig. 3.5 is shown the WSS spectrum for the two state wave packet at a long time delay. Also shown is the normalized transmittance recorded with a monochromator while blocking one pixel at each resonant transition wavelength. From the excellent agreement, the effective full width at half maximum (FWHM) attenuation width of each resonantly excited state is approximately 1.7 pixels,

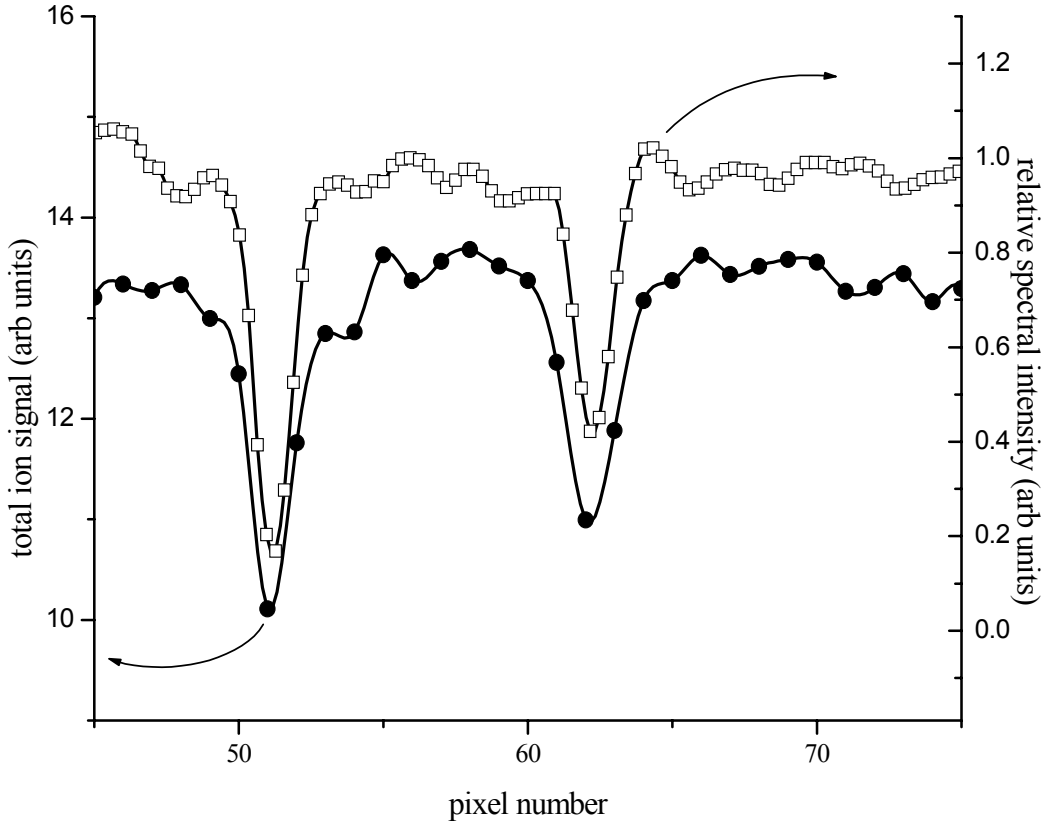

Figure 3.5: WSS (○) Spectrum with the probe set to t>5.0 ps. Spectral attenuation (△) of the pump pulse light [1-I(unattenuated)+I(attenuated)] recorded with a monochromator while blocking pixels 56 and 67 on the SLM. The linewidth of approximately 1.7 pixels is attributed to non-ideal focusing conditions in the pulse shaper.

which is almost entirely an effect of the single frequency spot size on the SLM and not an effect of the absorption lineshape of Li_2. It is confirmed that there are two discrete resonances within the bandwidth of the pump pulse.

Figure 3.6 shows the coherent ionization signals of the two state wave packet following various EA optimizations. In Fig. 3.6(a), the pump-probe delay (dashed line at 5.4 ps) is set so that the wave packet should be in phase with the signal generated by unshaped pulses. This optimization was run for 30 generations, with all 128 pixels involved in the optimization. A full signal versus pump-probe delay was then acquired using the optimized phase pattern. Note how the optimized wave packet signal builds up over a long period. Additionally, the optimized wave packet shows no obvious multiphoton burst as seen at 0.0 ps pump-probe time delay in the unshaped wave packet signal. The traces in Fig. 3.6(b) are optimized for 20 generations under conditions chosen to be out of phase with the reference signal, verifying that an arbitrary wave packet phase can be achieved. In the top trace, only those pixels near the resonances were allowed to be manipulated by the EA, while the rest were kept at a constant phase of π. In the middle trace, the same pixels were manipulated by the EA, but the light on the other pixels was attenuated. The amplitude of the coherent oscillations in all three of these optimized cases is similar in amplitude to the unshaped wave packet signal, regardless of whether or not the non resonant frequencies are manipulated during the optimization.

To analyze further the ability of the EA to find the expected result, shown in Fig. 3.7 are several optimizations that were run to find the repeatability of the

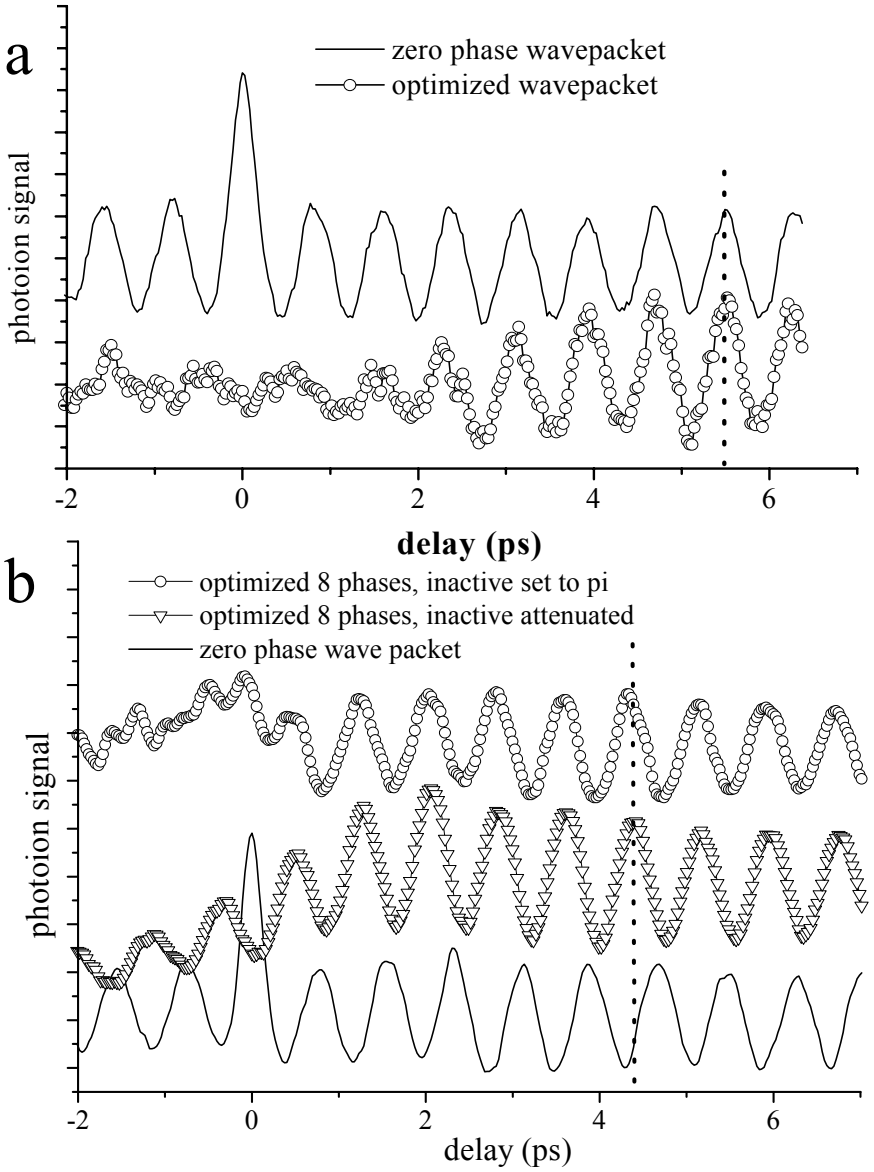

Figure 3.6: Two state wave packet signals for different optimization conditions. In both panels, the vertical dotted line marks the pump-probe time delay at which the signal optimization is sought. Panel (a): Wave packet signal for optimized phases (○) for a pump-probe delay of 5.4 ps, using all 128 pixels in the optimization, and an unshaped wave packet (solid line). The optimized wave packet has been offset for visualization purposes. Note the multiphoton signal burst at zero time delay in the zero phase (unmodified pulse) wave packet signal, which is absent when the phases are manipulated. This is due to the overlap of the pump and probe pulses at t=0. Panel (b): wave packet signal optimized at 4.2 ps when only two regions of four pixels each centered at each resonance (i.e., $\lambda_{resonant}$ ±2 pixels) are used, with non-resonant wavelengths either held at a constant phase of π (○), or attenuated (▽). Wave packet signals are offset vertically for clarity.

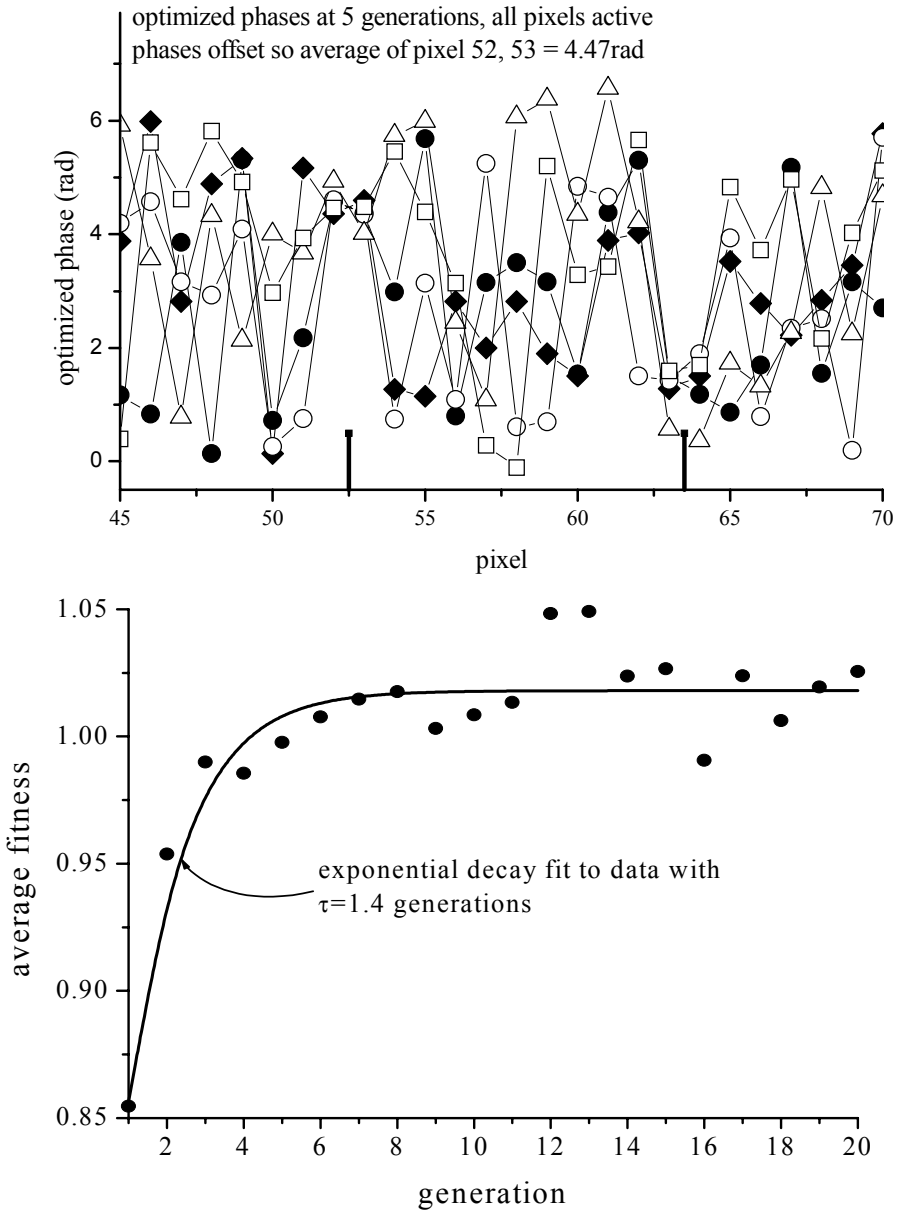

Figure.3.7. Long time delay optimization convergence. Panel (a): optimized phases after five generations for five different optimizations with the pump-probe delay set to 5.1 ps. Phase profiles have been offset so that the average phase of pixels 52 and 53 is the same for all optimizations. Resonant wavelengths are marked with vertical lines. Note the convergence of optimized phases at pixels 63 and 64. Panel (b): evolution of the average fitness (●) by generation number for one of the long time delay optimizations. The fit line is an exponential with a time constant of 1.4 generations.

solutions. Figure 3.7a shows the optimized phase difference of the two resonant wave packet states for the best individual after five generations of each optimization, allowing all 128 pixels to be manipulated. The average phase difference for the best individual from each of the five separate optimizations is $1.0\pi \pm 0.12\pi$ radians, where the pump-probe time delay was set to be π radians out of phase with an unshaped wave packet. This shows that even after just a few generations, the EA converges to a consistent phase difference between the transition frequencies. Another characteristic of the optimized phases in Fig. 3.7a is that at least two pixels are optimized around each transition frequency. This reflects the width of a monochromatic spot on the SLM, which is approximately 1.7 pixels.

Figure 3.7b shows the evolution of the average fitness of each generation for one of the optimizations above, extended to 20 generations. From this data, there is little change in the average fitness after five generations. This indicates that the optimization has largely converged, with a fit to an exponential characterized by a lifetime of 1.4 generations.

In the two state optimizations above, the complexity of the EA is varied by allowing either 128 or 8 pixels to be involved in the optimization of the two state wave packet. The success of the optimization is similar for both cases. This supports the notion that in the weak field limit the EA only sees the pixels relevant for the transition wavelengths. However, the speed of the optimization can be affected by how many pixels are involved in a particular optimization.

This dependence of the optimization time on the number of active pixels can be seen experimentally in Li_2. For the long time delay optimization of the two state wave packet, which has about 4 relevant pixels, the average fitness is characterized by a rise time of 1.4 generations. A similar optimization performed on the ten state wave packet showed a rise time of approximately 13 generations. In this case, the 128 pixel resolution was divided into ten regions (blocks) with each block centered on a transition for each of the ten states in the wave packet, giving ten effective pixels.

To better illustrate that the EA can in fact find a global maximum, the photoionization signal of a ten state wave packet was optimized for 30 generations at a time delay of 6.9 ps, again manipulating all 128 pixels. The EA was able to optimize the photoionization signal, as shown in Fig. 3.8. Notice how the EA has essentially time-shifted the unshaped wave packet dynamics by 6.9 ps. A similar time shift can be accomplished with a knowledge of the state energies and their positions on the SLM, but the result has been obtained here with none of that knowledge applied.

The two state wave packet photoionization signal, which consists of both incoherent and coherent components, was optimized at pump-probe time delays outside of the temporal pulse shaping window. Assuming that little of the resonant wavelength light gets directed out of the beam from abrupt phase shifts, the incoherent signal from the first term in Eq. (1.1) will remain a constant. This leaves the coherent oscillation as the predominant component of the photoionization signal that can be optimized.

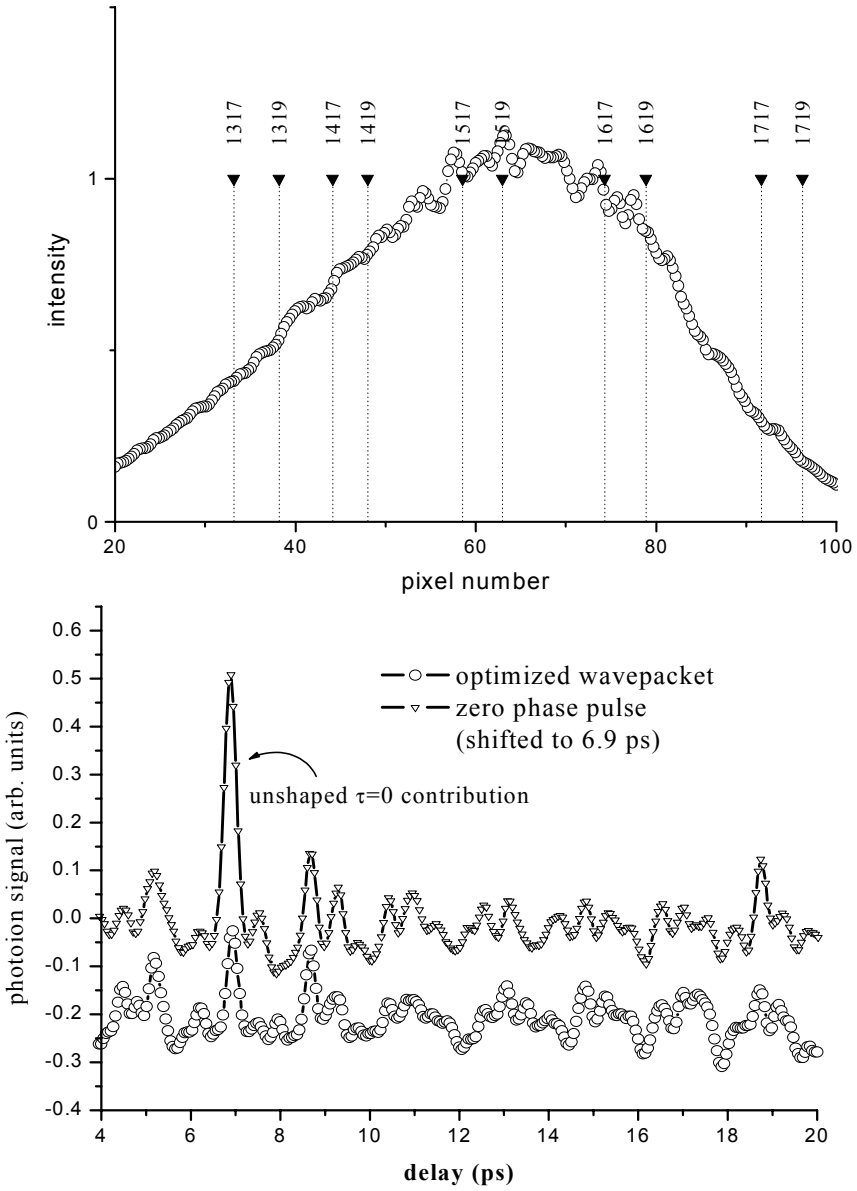

Figure 3.8. Multiple state wave packet optimization. Panel (a): wave packet resonances (vertical lines) superimposed on the pump pulse spectrum. Panel (b): the unshaped wave packet (▽) shifted by 6.9 ps to display its similarity to the wave packet optimized at 6.9 ps (○). Note the multiphoton burst at zero delay in the unshaped wave packet, similar to that in Fig. 3.6. The optimized wave packet has been offset for better visualization.

The main process by which the coherent oscillation gets optimized is the establishment of the correct relative phases of the wave packet states to produce the maximum of a recurrence at the desired time delay. The presence of the single, phase shifted cosine wave in the coherent signal indicates that the EA is setting the relative phases of the two participating eigenstates to be a specific value, with no requirement as to the absolute phase of either state relative to the rest of the pulse. The optimized phases for multiple runs by the EA, as shown in Fig. 3.7, all show a convergence of the relative phase of the resonant wavelengths. The actual phases of pixels 52 and 53, which have been offset in the figure, were distributed fairly evenly between 0 and 2π radians, indicating that the phase relative to any non-resonant wavelength is irrelevant.

These experiments were set up to optimize the photoionization signal after the pump pulse light is no longer present. As can be seen from the onsets of the oscillatory signals in Fig. 3.7, the timescales for the wave packet coefficient amplitude buildup under three different optimization conditions is not defined by the EA, with the $E \leftarrow A$ population transfer happening variably over a period of ~6 ps (*i.e.*, -2 to 4 ps). The buildup of the coefficients depends in a complex way on both resonant and non-resonant wavelengths, but the similarity of the final wave packet amplitudes under several conditions where the non-resonant wavelenths were either restricted (or not) shows that at long time delays non-resonant frequencies in the pump pulse play little to no role in the optimization. Consequently, how the wave packet amplitude builds up does not matter as long as it reaches its maximum value by the optimized pump-probe time delay, which

is the same as its value predicted by the t=∞ approximation implied in Eq. (1.1). Numerous trials show that the wave packet amplitude at long times cannot be distinguished between the unshaped and optimized cases, even though many different coefficient buildup timescales have been observed in using various optimized and randomized phase pulses.

Since the EA uses a constant mutation rate, the mechanism for optimization of the simple two state system is computationally equivalent to that of a more complex system; during any one generation, the EA is only aware of that generation, so historical information such as the number of relevant pixels has no effect on which pixels are mutated. Using this fact, we can observe just a few pixels of the 128 pixel optimization and treat the system as if it contained only four parameters, which in this case are the pixels on which the resonant wavelengths have been imaged. With this simplified physical case, we can develop a measure of the precision of the EA in general. Figure 3.7a shows the phases from the best individual for each of five different optimizations after five generations. The standard deviation of the relative phases between the pixels of the resonant transitions is $\pm 0.12\pi$ radians. We expect the precision of the best individual of each generation to have a lower bound defined by the average fitness of all individuals in each generation of a single optimization, which experimentally shows a 1.4 generation rise time. Assuming the modulated signal is simply the phase of a cosine wave, the root mean square deviation from the true optimum is $\Delta\theta = \text{acos}\,(1-\exp[-gen/\tau])$ where *gen* is the generation number, and τ is the optimization time constant. If we take τ to be 1.4 generations, then at five

generations, the lower bound to the precision of the optimizations should be $\pm 0.09\pi$ radians. This slight discrepancy with observation is most likely a result of a slight miscalibration of the applied phases on the SLM in the experiments, adding error to the readout of the applied phases.

3.6 Optimizing transient wave packet

In this section, we consider a more complex process that has multiple pathways and requires the optimization of the phases of many more frequencies than the previous experiments. This is accomplished by setting the pump-probe time delay to be within the temporal pulse shaping window, as was described in section 2.1. We consider a two state wave packet, and the EA again uses the full 128 pixel resolution, with elitist reproduction and mutation operators only.

We set the pump-probe time delay to the peak of the second recurrence (1.6 ps) of the unshaped coherent oscillation signal. This time delay was chosen for optimization so that the maximum possible transient component of the photoionization signal would be equal to the $t=\infty$ oscillation amplitude. By optimizing the ionization signal at the second recurrence, as produced by unmodified laser pulses, the results from the previous section indicate that the phases of the wavelengths at the two resonant transitions should be the same, *i.e.*, $\Delta\varphi_{ij}=0$.

An EA optimization at this short time delay was carried out for 30 generations, and the results are shown in Fig. 3.9. In Fig. 3.9(a), from the

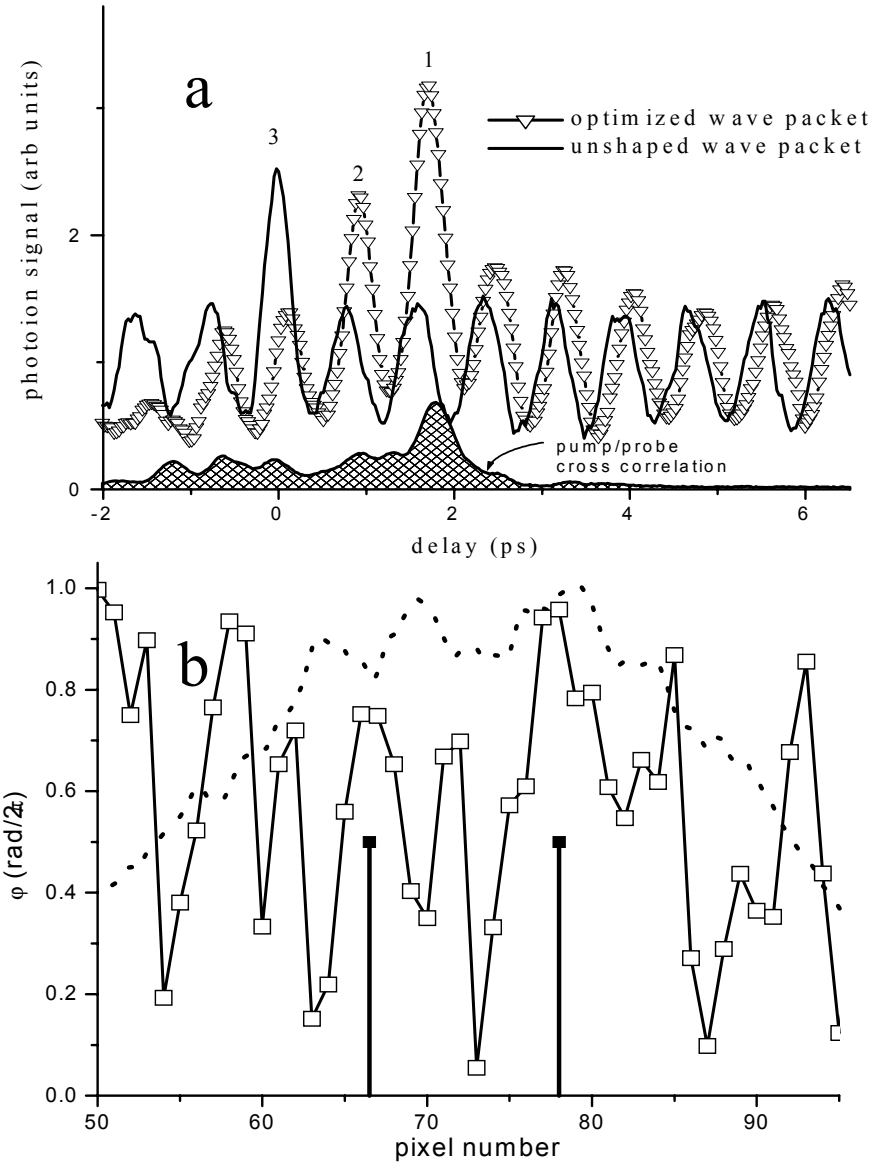

Figure 3.9. Short time delay optimization results. Panel (a): optimized wave packet signal (▽) for a pump-probe delay of 1.6 ps. The solid line shows the wave packet signal produced by unshaped pulses. The shaded region shows the pump-probe cross correlation on a photodiode. Peak 1 has been optimized and clearly exceeds the maximum multiphoton burst (peak 3) of the unshaped trace. Peak 2 was not monitored in the fitness function. Panel (b): optimized phases for a pump-probe delay of 1.6 ps, after 30 generations. The resonant transitions are marked with solid vertical lines, and the spectral intensity is denoted with the dotted line. Note the regions with a linear slope of the phase (most of region shown), the marked deviation from linear slope of the phase around the resonant transitions, and the unequal phase of the resonant transitions.

complete pump-probe signal versus time delay, we see that the EA clearly optimizes the ionization, but at a slightly longer time delay than was desired. Because of the effects of time-dependent wave packet coefficient phase *and* amplitude maximization, the signal at 1.6 ps is actually larger than the t=∞ two-state recurrence alone. For comparison, a wave packet generated using unshaped pulses is included as a reference. As can be seen, the ionization maximum at 1.6 ps far exceeds that of the unshaped pulse at the same time delay, but at time delays longer than 4 ps the amplitudes are the same in both cases. The wave packet signal also shows no discernible phase shifting relative to itself over the course of its buildup. There is a constant 0.4 radian phase shift of the optimized wave packet recurrences relative to the unshaped wave packet from -2 ps to 7 ps. This phase shift is an artifact of competing processes that apply a phase shift to the overall signal in early generations, and it is observed that the wave packet phase does converge on the desired phase as the EA progresses.

A cross correlation of the shaped pulse with an unshaped pulse obtained on a $GaAs_xP_{1-x}$ photodiode, also shown in Fig. 3.9(a), indicates that the peak light intensity at the 1.6 ps optimized time is much less than what occurs in the unshaped, near-transform limited case (not shown). At first glance, this may appear to be a highly suboptimal solution compared to an intuitive solution of a temporally shifted transform limited pulse. However, the photoionization signal at 1.6 ps significantly exceeds the signal at t=0 for the unshaped pulse, in spite of the very low optimized light intensity.

Examination of the phase pattern for the optimization shows some of the processes that are occurring. The phase pattern in Fig. 3.9(b) shows a roughly linearly phase (modulo 2π) as a function of wavelength across much of the pulse, which is characteristic for a pulse that is being shifted in time. Indeed, the shifting of light intensity to longer times is what is observed in the cross correlation. Looking at the phases near the wave packet resonances, however, the linear phase is far from preserved. Finally, the relative phases at the wavelengths resonant with the wave packet transitions show a slight phase shift (0.4 radians) which agrees with that seen in wave packet signal.

Figure 3.10 shows an evaluation of the solutions found by the EA at various stages of an optimization. In Fig. 3.10(a) the average fitness versus generation number is shown; note that the optimization takes much longer to converge than in the long time delay optimization cases presented earlier. In Fig. 3.10(b), it is shown that the manipulation of the long time wave packet at 5.6 ps is achieved on a shorter timescale than the optimization of the photoionization at the short pump-probe delay time of 1.6 ps.

At short pump-probe delays (<4 ps) the pulse shaping apparatus has the ability to produce a pump pulse electric field that overlaps in time with the probe pulse. The simultaneous presence of electric field from both beams can create transient coefficient amplitudes that depend on frequencies that are not resonant with the wave packet preparation frequencies [see Eq. (1.1)]. The EA finds a phase pattern that creates a maximum in the photoionization signal at 1.6 ps, and

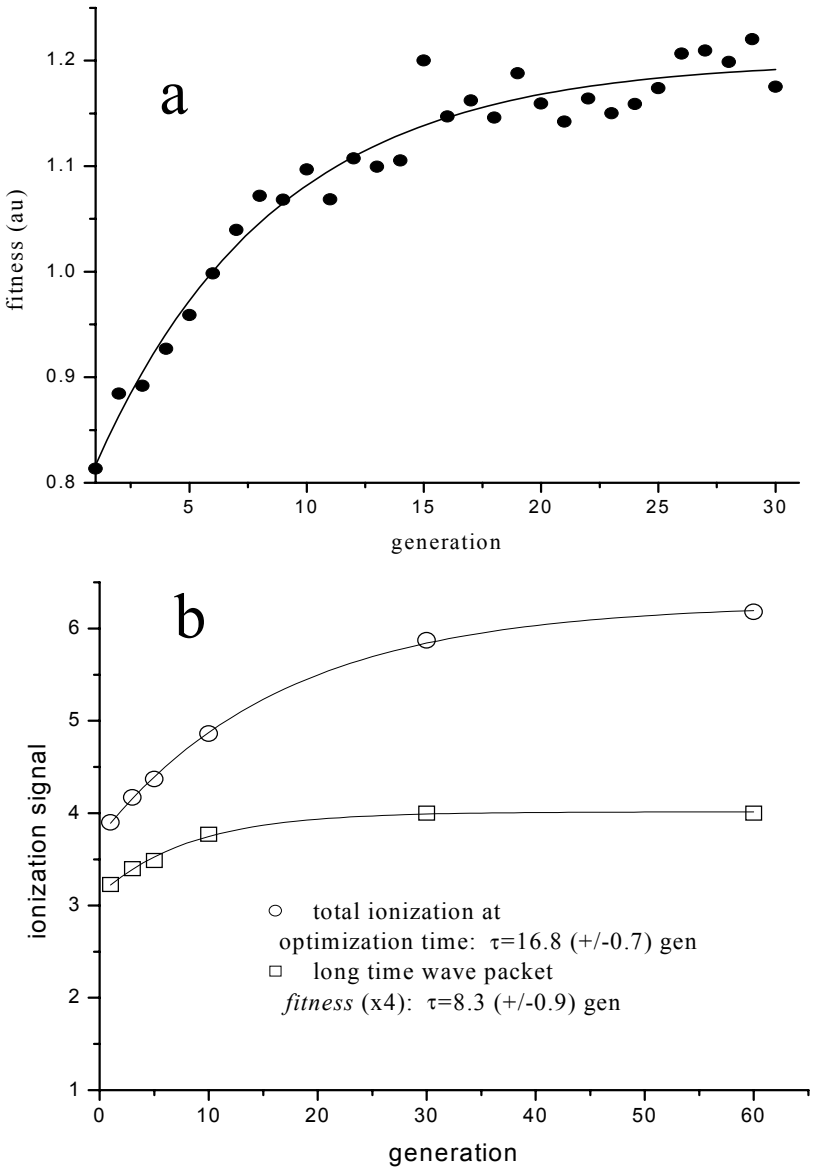

Figure 3.10. Evolution of the fitness versus generation number for the 1.6 ps time delay optimization. Panel (a): average fitness (●) as monitored during the optimization. The solid line is a double exponential fit with time constants of 5 and 35 generations. Panel (b): total coherent ionization signal at 1.6 ps (○) and 5.6 ps fitness value (□) assigned after completion of the optimization using phases from the individuals with the highest fitness values of selected generations. The long time *fitness* value was 4 times the ratio of the total ionization signal divided by the reference (*i.e.* unoptimized) ionization signal at 5.6 ps (note that this value was not monitored during the optimization). The fits show a 17 generation rise time at 1.6 ps pump-probe delay and an 8 generation rise time at 5.6 ps pump-probe delay.

it also generates substantial electric field at 1.6 ps, possibly indicating the presence of multiphoton burst effects.

The EA finds the best maximum in the ionization signal when the pump-probe delay is set within the temporal pulse shaping window. As seen in Fig. 3.9(a), the amplitude of the oscillating photoionization signal around 1.6 ps [peak (1)] is larger than the long time oscillation amplitude; additionally, it exceeds the peak signal in the unshaped case [peak (3)]. At the optimized time delay, the cross correlation data shows a peak in the pump pulse intensity, which suggests that the EA does optimize somewhat a time-ambiguous (i.e. pump-probe + probe-pump), or multiphoton burst, component of the signal. However, the large amplitude of the peak [peak (2)] preceding that at the optimized time delay does not coincide with significant pump pulse intensity. This peak cannot then be attributed to a multiphoton burst. This observation is consistent among repeated optimizations, with little obvious correlation of the wave packet oscillations and the light intensity (except at the optimized time), verifying that the wave packet amplitude coefficients of Eq. (1.1) are transiently pumped while maintaining their correct relative phase relationship.

Notice in Fig. 3.9b that the relative phase of the resonant frequencies is 0.4 radians, which is consistent with the observed phase shift of the optimized experimental wave packet oscillations. Even though first order perturbation theory predicts that wave packet coefficients can change phase during their buildup [see chapter 5], it is not apparent in this data. The phases of each

coefficient may be changing during the pump pulse, but it appears that the transient relative phase ($\Delta\varphi_{ij}$) remains relatively constant at time delays after -2 ps, as judged by the positions of the optimized wave packet recurrences relative to the unshaped wave packet recurrences. The constant non-zero phase shift is due to competition in early generations of the optimization of the wave packet recurrences, wave packet amplitude coefficients, and a multiphoton burst effect.

Although there is no obvious physical requirement that the coefficient phase evolution during the pump pulse must be the same for both wave packet states, the effect of the EA is such that both states have the same transient phase relative to long time [*i.e.*, $\varphi_i(t=1.6\text{ps})-\varphi_j(t=1.6\text{ps}) = \varphi_i(t=\infty)-\varphi_j(t=\infty)$]. As the EA begins to optimize the photoionization signal at 1.6 ps, one dominant early effect to be optimized is the relative phase of the wave packet states. The reason is twofold: the phase shift of the wave packet can cause a large change in the fitness, and very few pixels are involved in determining the phase of the wave packet. Out of random phase configurations, the correct relative phases of the few resonant pixels will be more likely to occur than the correct phases of all the resonant and non-resonant phases. Figure 3.10 shows the evolution of the fitness of an optimization at a time delay of 1.6 ps. It is shown in panel 3.10(b) that while the average fitness rises with an approximate lifetime of 16 generations, the optimization of the long time delay component of the signal (representative of resonant wavelengths) proceeds about twice as fast as the optimization of the peak ionization signal. As the EA proceeds through many generations, the optimal $t=\infty$ phase persists, for it represents a "ridge" in the total photoionization solution

space, leading to a final solution that is a combination of the correct resonant frequency phase shift, transient wave packet amplitude, and possibly multiphoton burst effects.

3.7 Modeled optimization

A calculated model of this system was studied in a situation free from noise and where the optimization could be extended up to 200 generations in order both to compare the form of the perturbation theory solution of Eq. (3.1) and to investigate the competition between coefficient buildup and multiphoton effects. The EA was chosen to modulate 128 phases, similar to how it would normally modulate phases on the SLM. The fitness function given to the computer included both a wave packet oscillation term and an undefined multiphoton burst term, respectively:

$$f(i,t) = |a_1(t)||a_2(t)|\cos[\varphi_1(t)-\varphi_2(t)] + 1.25|\Sigma_j b_j \exp[i(\omega_j t+\varphi_j)]|^2, \qquad (3.5)$$

where the a_1 and a_2 are derived using time dependent perturbation theory as in Eq. (3.1), φ_1 and φ_2 are from Eq. (3.1), and b_j is the amplitude of light with central frequency ω_j and phase φ_j imaged onto pixel j. The multiphoton burst term is normalized so that $|\Sigma_j b_j|^2 = |a_1(\infty)||a_2(\infty)|$. The spectral profile ($b_j$) is Gaussian and has a FWHM of 35 pixels (156 cm^{-1}), centered at 12500 cm^{-1}. States 1 and 2 are set to have energies of 12480 cm^{-1} and 15020 cm^{-1}, respectively.

After 200 generations, the calculated optimal solution has a linear phase applied across almost the entire pulse, with a deviation from linear phase applied near the resonant wavelengths (see Fig. 3.11), and no phase shift between wave

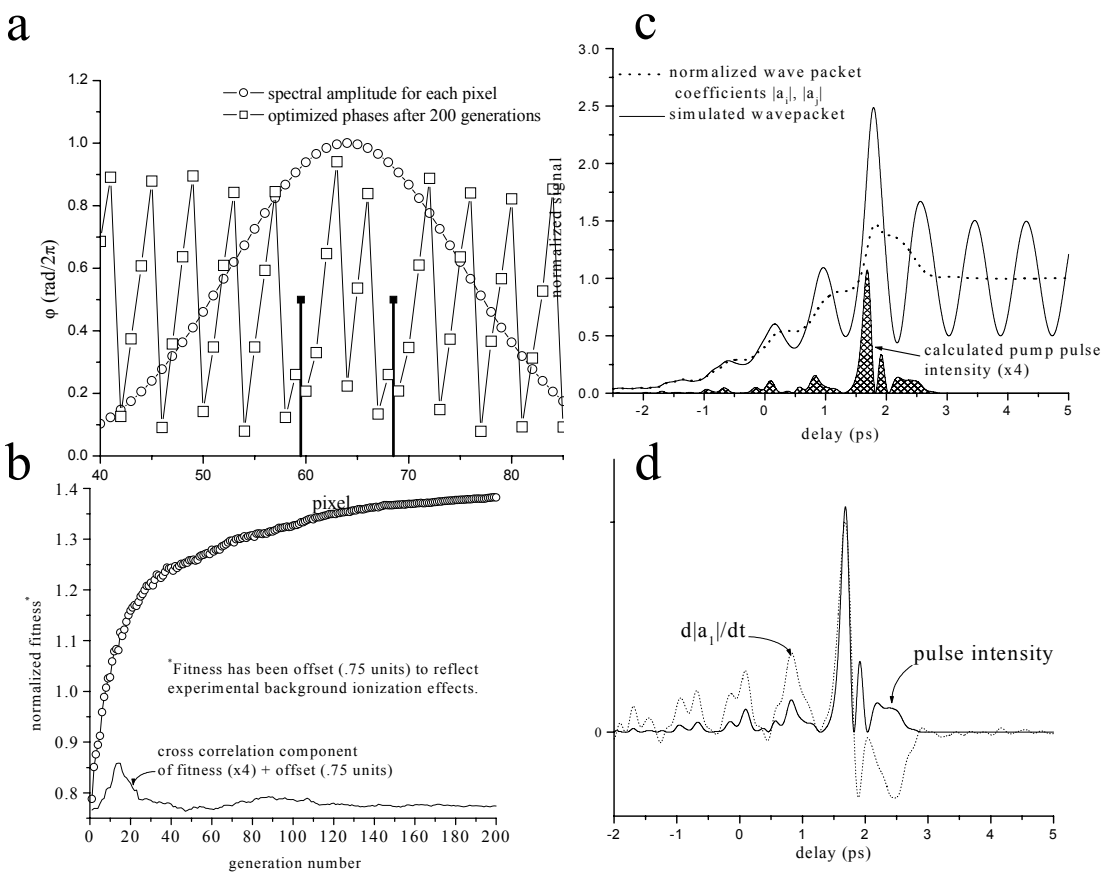

Figure 3.11. Model optimization results. Panel (a): optimized phases (□) as modeled by Eq. (4) after 200 generations. Resonant transitions are marked by solid vertical lines, and the spectral intensity is indicated by the dotted line. Notice the linear phase applied across most of the pulse, except in regions near the resonant transitions. Panel (b): progression of the average fitness (○) during the optimization (scaled to reflect experimental background effects in Li_2) and four times the average multiphoton component of the fitness (solid line), offset by 0.75. The average long time fitness was not a component of the observed fitness and is simply a measure of the long time wave packet amplitude and phase. Panel (c): wave packet coefficients $|a_1|$ and $|a_2|$ (dotted line), four times the optimized electric field intensity (shaded region), and a simulated wave packet (solid line). The coefficients have been normalized to their values at $t=\infty$, and the pulse intensity has been normalized to reflect its correct contribution to the calculated fitness at the optimized time delay. Both coefficients follow the same buildup path, obscuring one in the figure. Notice the very low light intensity at the optimized time. Panel (d): optimized pulse intensity at 200 generations (solid line), with the derivative of the absolute value of the wave packet coefficient (dotted line). Notice that immediately after the optimized time the wave packet coefficients are driven down to their final values.

packet states: $\varphi_1(1.8\text{ ps})-\varphi_2(1.8\text{ ps}) = \varphi_1(\infty)-\varphi_2(\infty)$. This behavior closely mimics the result found in the experimental optimization in Li_2. One important result obtained in this modeled optimization is that the laser pulse intensity at 1.8 ps is virtually zero, as can be seen in Fig. 3.11c. Instead, its peak intensity is found at 1.73 ps. Note that even though there cannot be a multiphoton burst contribution to the photoionization at 1.8 ps delay, the signal exceeds by 50% what would be predicted assuming a simple temporal pulse shift coupled with the normal wave packet oscillation amplitude at long time delays. The difference is the time dependent wave packet amplitude coefficients.

In this model, the wave packet amplitude coefficient buildup is in direct competition with the multiphoton effect, with the coefficient buildup dominating the calculated photoionization signal. Figure 3.11b shows that even though the multiphoton term plays a role early in the optimization with a maximum contribution at generation 16, it is later overwhelmed by the wave packet oscillation term. Experimentally, a -70 fs time shift of the peak intensity from the optimized time is difficult to resolve, especially given that our experimental cross correlations are convolutions of the shaped pulse with an unshaped pulse with a width of up to 180 fs. Also, the experimental optimization was concluded at 30 generations, at which point it is reasonable to expect that the multiphoton effect may not have been fully suppressed yet. Regardless, this calculation does show that the optimal pulse shape has low intensity at the optimized pump-probe delay.

The average fitness for the modeled optimization also shares several common traits with the experimental optimization of Li_2 photoionization,

including an initial quick rise attributable to a wave packet phase shift followed by a slower further rise to the optimum. To illustrate, when the modeled fitness is fitted with a double exponential decay function, two lifetimes of 7.2 and 60 generations can be seen. This is similar to the experimental average fitness in Li_2, which also shows a quick initial rise followed by a slower decay, with a double exponential rise fit with lifetimes of 5 and 35 generations (Fig. 3.11). The evolution of the model and experiment show qualitatively similar behavior, suggesting a similar mechanism of optimization.

Given that this model calculation qualitatively reflects the Li_2 system, hypotheses regarding the excited state coefficient evolution can be put forward. In the calculation, before the optimized time delay, most of the pulse intensity goes into building up the amplitude of the coefficients, as shown in Fig. 3.11d. Immediately after the optimized time, there is a π phase shift of the carrier frequency of the pulse, with all subsequent light intensity driving the coefficient amplitude down. This is made possible by correctly timing the buildup attributable to non-resonant frequencies. In other words, the phases of non-resonant oscillations in $|a_{pu,i}|$ are optimized so that, collectively, they come into phase at 1.6 ps and quickly dephase just after that.

3.8 t=0.0 ps Optimization

The previous sections showed that indeed it is possible to optimize the phase of a coherent oscillation as well as transient population transfer type processes. Even in the case of the model optimization, whose solution shows little noise, the nature of the optimized phase mask seems somewhat hidden by the linear part of the applied phase mask. To try to reduce this difficulty, an optimization was performed to get the greatest photoionization signal at t=0.0 ps. As in the previous sections, the launch state of $(v_A, J_A)=(11,28)$ was used so that a wave packet consisting primarily of $(v_E, J_E)=(9, 27)$ & (9,29) gets optimized.

Figure 3.12 shows the optimal phase mask found by the EA while monitoring the photoionization at t=0.0 ps. For the positively and negatively detuned frequencies, there is a clear phase shift of approximately 1.2π radians around each resonance. This phase shift is a result of the EA finding an optimal population transfer condition. Additionally, right at each resonance, there is approximately the same phase. Since the size of the resonant spot on the SLM is about two pixels, the exact phase of the resonant frequency can not be known exactly in this case, but it is approximately π for each resonance. Additionally, there is a significant jump in the optimized phase around pixel 75. This is attributed to a competition between optimizing the phase of the quantum beat while simultaneously optimizing the transient wave function coefficients. This will be studied in more detail in the next chapter.

Figure 3.13 shows the pump-probe trace corresponding to the optimal phase mask compared to a pump-probe trace with an unshaped pump pulse. Also

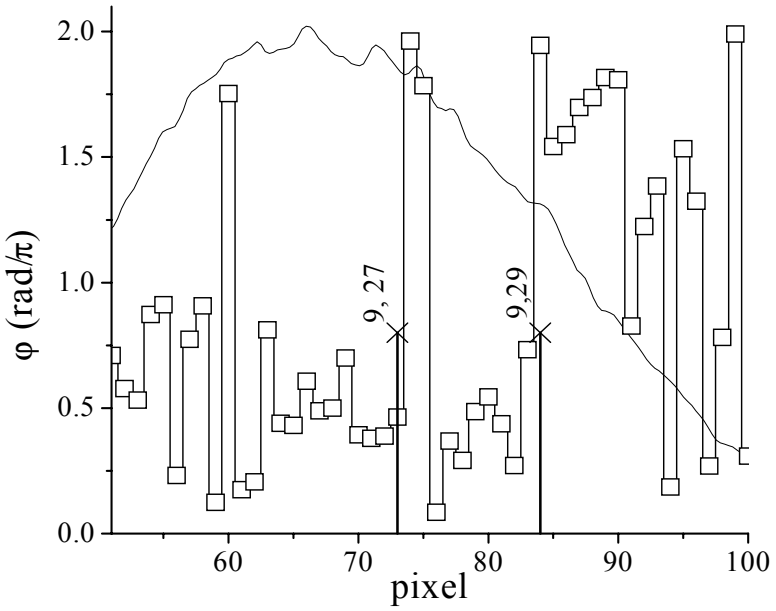

Figure 3.12: Phase mask (□) found by EA when optimizing photoionization at t=0.0 ps. Resonances are marked (×), and the laser spectrum is noted by the solid curve. Note the phase shifts of the frequencies to the left and right of the resonant frequencies is approximately 1.2π radians.

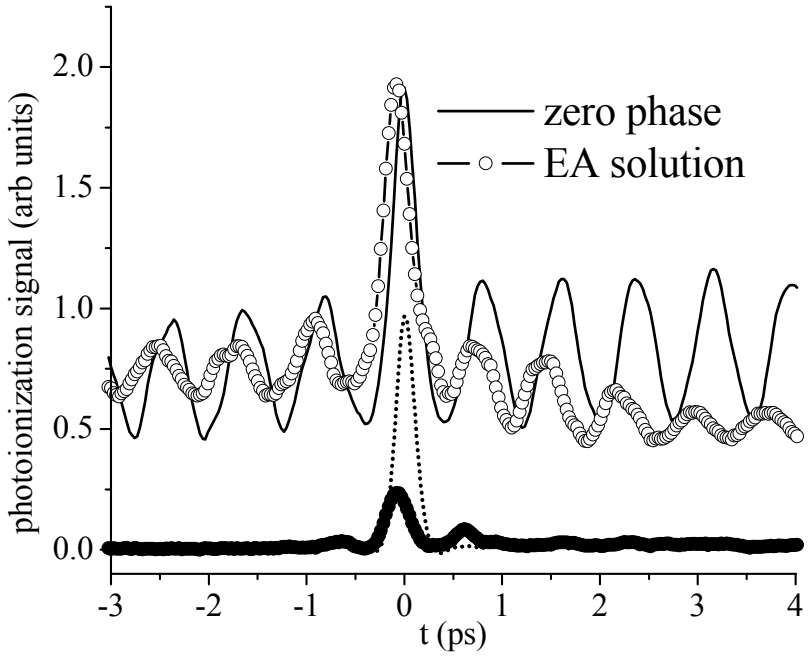

Figure 3.13: Optimized photoionization with cross correlations. The top traces show the optimized photoionization (○) pump-probe trace along with an unshaped pump-probe trace (solid line). Below are cross correlations with the unshaped probe pulse for the optimized pump pulse (●), and the unshaped pump pulse (dotted).

shown in the lower part of the figure are cross correlations with the probe pulse of the optimized and unshaped pump pulses. The photoionization shows a large peak at the optimized time, as should be expected from earlier work. The peak at t=0.0 ps barely exceeds that found in the transform limited case, but there are some interesting traits to the optimized dynamics. First, even though the photoionization does show a maximum similar to the transform limited case, the background offset and the coherent oscillation amplitude are both smaller for the optimized case. Since the optimization considers the photoionization at only one time, the physical requirements for optimization only "see" an optimal transient state. In this case, the transient coefficient is optimized at the cost of the final state amplitude.

The cross correlation measurements (Fig. 3.13, heavy line) also show an interesting feature. The optimized cross correlation shows that the amplitude at t=0.0 ps is only approximately one quarter that in the transform limited case. Even so, the photoionization remains strong. In the optimized case, it could be argued that the transient effects exceed the transform limited case even with this low peak intensity. This observation hints at the power of using transient processes to control dynamics, as will be explored in the next chapters.

Unfortunately, at t=0.0 ps, the actual mechanism for the optimized photoionization is unclear, since at that time, the shaped pulse is simultaneously a pump pulse as well as a probe pulse. A mechanism for simultaneous optimization of the probe pulse can be imagined, introducing some ambiguity into the photoionization mechanism. At the very least, we should expect minimization of

diffraction of the light at those frequencies of light that are resonant with the primary autoionizing Rydberg states in the probe section of the pulse[47]. Also, we should expect that the phase difference between the resonant probe regions for states (9, 27) and (9, 29), respectively, should be approximately zero[48]. These considerations complicate the optimization, so a means to eliminate the pump-probe ambiguity at t=0.0 ps has been used, and it will be examined in the following chapter.

Chapter 4

Weak Field Population Control

4.1 Introduction

Coherent control remains a primary goal of ultrafast laser dynamics studies [1,2]. Research so far addresses several key categories, such as the use of resonant frequencies to control quantum wave packet interferences [2-5] and novel pulse shapes to control multi-order processes [2,6-10]. Optimization of coherent control has been achieved using various types of learning algorithms [8,11-13] [see previous chapter], but the nature of the mechanisms for the optimal results is not always readily apparent. This chapter will identify a class of pulse shapes that enhance the population transfer from a single state to multiple excited states, providing a basis for understanding the nature of optimal pulse shapes for both population transfer and quantum interferences in the superpositions. Pulse shapes that have been shown to enhance transient excited state population in a two level system will be applied to multiple excited states. All experiments will be analyzed using first order perturbation theory.

Much work has been devoted to the field of population transfer dynamics in the continuous wave regime [14], but only recently have well-established population transfer theoretical tools been applied to the wide bandwidth inherent to ultrafast spectroscopy [13,15-18]. For example, it has been shown that chirped pulses can be used to enhance population transfer dynamics in a multiphoton process [15,19] or even transiently in a single photon process [13,17]. It has been

shown that optimal enhancement of multiphoton dynamics can be achieved not by chirped pulses, but by applying constant phases to *blocks* of nonresonant frequencies relative to resonant frequencies [13,16,18], based on the t=0.0 ps optimization described in the previous chapter. By using a frequency domain analysis, the optimal pulse shape is shown to depend primarily on frequencies that are near resonant, as will be discussed in detail in a later section.

This chapter considers the simultaneous control of both time dependent population transfer dynamics and superposition state quantum interferences using analytically optimal pulse shapes, in comparison to simple chirped pulse shapes and near transform-limited pulses. Of interest are the effects of resonant and nonresonant frequencies involved in the excitation of superposition states. By independently controlling not only quantum interferences between wave packet states, but also the population transfer dynamics to each state, the coherently controlled ionization yield at specific time delays is more than double that produced by a transform limited pulse in a two-state superposition pump-probe experiment. A two-color ultrafast laser experimental system, with pulse shaping, is used to isolate the coherent population transfer dynamics of a two-level superposition in Li_2 molecules. The criteria for independent control of the coherent population transfer dynamics and quantum interferences are established. Extensions to more than two states are also discussed.

Simultaneous coherent control of two well-defined excited states unifies concepts concerning the dynamics between interfering superposition states and population transfer dynamics to individual states. As long as the interfering states

are sufficiently separated in energy from each other, the population transfer dynamics to each state can largely be independently controlled. Additionally, the relative phases of the multiple states are controlled during the process of population transfer. In the following sections, a theoretical framework for these experiments is first presented, followed by a summary of experimental considerations. Finally, experimental results are presented and discussed in the next section, along with a quantification of the limitations of enhancing photoionization using various pulse shapes. The degree to which the population transfer for two states can be independently controlled is quantified in that final section.

4.2 Theory

In the weak field limit, first-order time-dependent perturbation theory can be used to describe a single photon absorption. The excited state amplitude coefficient for a single state is described in the time domain [20]:

$$c_n(t) = \frac{\mu_{eg}}{i\eta} \int_{-\infty}^{t} \varepsilon(t) \exp(i\omega_{eg} t')dt' , \qquad (4.1)$$

where μ_{eg} is the dipole moment matrix element between the excited and ground states, $\varepsilon(t)$ is the electric field as a function of time, and $\omega_{eg} = (E_e - E_g)/\eta$ is the transition frequency. Using similar logic to earlier work [16,18,21], this excited state amplitude can be approximated for positive time *t* by the frequency domain expression

$$c_n(t) = \frac{\mu_{eg}}{i\eta}\left\{\tilde{\varepsilon}^*(\omega_{eg}) - \frac{i}{2\pi}\wp\int_{-\infty}^{\infty}\frac{\varepsilon(\omega)\exp[i(\Delta)t]}{\Delta}d\omega\right\}, \qquad (4.2)$$

where $\tilde{\varepsilon}^*(\omega_{eg})$ is the amplitude of the electric field at the transition frequency, $\varepsilon(\omega)$ is the amplitude of light at frequency ω, $\Delta = \omega - \omega_{eg}$ is the detuning, and $\wp$ is the Cauchy principal value. The first term in Eq. (2) represents the resonant contribution to the excited state amplitude, and the second term represents nonresonant contributions. As *t* approaches infinity, the second term averages to zero, and Eq. (2) reduces to the resonant component; however the second term does not necessarily average to zero for small *t* (*i.e.*, within the pulse width). In the absence of any phase manipulation (*i.e.,* transform limited pulses), the nonresonant term will be greatly diminished for all *t*, since the Δ term for $\omega>\omega_{eg}$ is π out of phase relative to $\omega<\omega_{eg}$ [18]. Additionally, the $i/2\pi$ leading factor of the nonresonant term places the nonresonant contribution $\pi/2$ out of phase with the resonant term. This phase relationship suggests that to bring all frequency components into phase at small *t*, an additional $+\pi/2$ and $-\pi/2$ phase must be added to the nonresonant frequencies above and below ω_{eg}, respectively. Additionally, the $1/\Delta$ dependence of the nonresonant term shows that the most influential frequencies will be those with the smallest detuning. These results may then be generalized to multiple excited states.

The $1/\Delta$ dependence of the nonresonant wavelengths lends itself to the possibility that frequencies with a large Δ can be manipulated with minimal influence on the excited state coefficient dynamics. This will allow for the manipulation of multiple states, provided that the energy separation between

states, Δω, is great enough that all frequencies near one state have little effect on any other states. For a two-state superposition, a lower limit of the degree to which the population transfer to state *i* can be independently controlled, I_{PTi}, is quantified as

$$I_{PT_i} = 1 - 2n\left|\int_{\Delta\omega/2}^{\pm\infty} d\Delta' \varepsilon(\Delta_i')/\Delta_i'\right|^2, \tag{4.3}$$

where Δω is the difference in energy between the superposition states ($\Delta\omega=\omega_i-\omega_j$), the second limit of integration (±∞) has the same sign as Δω, and $\varepsilon(\Delta')$ is the amplitude of the electric field at a specific detuning. The factor of 2 accounts for destructive interference, and *n* normalizes the expression so that the second term reaches a maximum of 1. Physically speaking, I_{PTi} is a measure of the cumulative intensity of all nonresonant contributions to a particular population at a specific time relative to the ideal case (*i.e.*, single control channel). In the case where two states have degenerate energies (*i.e.*, Δω=0) with a uniform energy spectrum, I_{PT}=0, the states can not be independently controlled. On the other hand, in the limit of Δω=±∞, the second term goes to zero, and the states are completely independent of each other. This analysis assumes a regime where the spectrum is divided into an arbitrary number of "control channels," with a specified bandwidth devoted to the control of each state. The spectrum is divided into two or more regions, and the integrated value of $\varepsilon(\Delta_i')/\Delta_i'$ inside the control channel for state *i* is compared to $\varepsilon(\Delta_i')/\Delta_i'$ outside of its control channel. Increasing the number of states involved in a control scheme will likely decrease the spectral width of the control channel for any state, decreasing the degree to

which that state can be independently controlled. In the discussion below, we use "control channel" to refer to large blocks of wavelengths surrounding each resonant transition and "resonant control channel" or "resonance" to refer to very small bandwidth regions centered on each resonant transition.

Lithium dimer (Li_2) is used as a model system to investigate the extent to which nonresonant frequencies can be used to control multiple excited state coefficients with a single pulse. The relevant potential energy curves in Li_2 are shown in Fig. 2.1 [22-24]. From a single launch state, two rovibrational states (v_E=9, J_E=27 & 29) are accessible within the bandwidth of the pump laser, creating a time-dependent wave packet. A probe pulse ionizes the coherent superposition at various pump-probe time delays to obtain the signal. For parallel pump and probe polarizations (referred to as "parallel probe"), the presence of multiple rotational states in the wave packet produces a coherent superposition state with oscillations at a frequency equal to the energy difference between the states [25] [see Fig. 4.1]:

$$S(t) \cong \left|pr_1\right|^2 \left|c_1(t)\right|^2 + \left|pr_2\right|^2 \left|c_2(t)\right|^2 + 2\left|pr_1 pr_2\right| \left|c_1(t)c_2(t)\right| \cos\left[\Delta\omega t + \Delta\varphi(t)\right] \quad (4.4a)$$

where pr_1 and pr_2 are constants related to the probe step (not discussed here); the energy separation, $\Delta\omega$, is 42 cm^{-1} (1.5 Thz); and $\Delta\varphi$ is the relative phase between the wave packet states at time t. In contrast, for a probe polarization oriented at the magic angle (~55°) with respect to the pump polarization ("magic-angle probe"), the coherent oscillation is completely suppressed, so

$$S(t) = |pr_1|^2 |c_1(t)|^2 + |pr_2|^2 |c_2(t)|^2. \quad (4.4b)$$

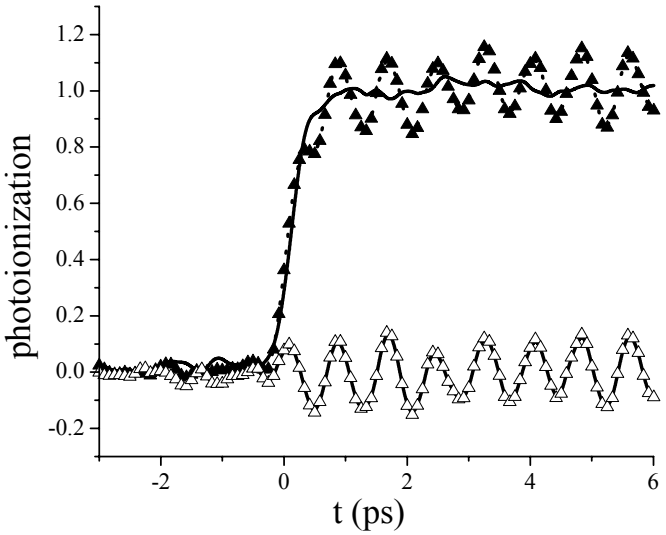

Figure 4.1: Pump-probe traces at parallel (▲) and magic angle (solid line) pump-probe polarizations, along with the difference (△) between the traces for unshaped pump pulses. These traces correspond to the total, incoherent, and coherence portions of the signal, respectively, with the raw signals normalized to an average value of 1.

This suppression is possible because the coherent oscillation is rotational in nature.[6,24] Hence, by manipulating the probe polarization, we can select whether the signal reflects a full wave packet trace or simply the ground to excited state population transfer dynamics. Furthermore, by subtracting the magic-angle probe signal from the parallel probe signal, we are left with just the coherent oscillation piece

$$S(t) = 2|pr_1 pr_2||c_1(t)c_2(t)|\cos(\Delta\omega t + \Delta\varphi). \quad (4.4c)$$

The probe step consists of an ultrafast pulse of a different color than the pump pulse [26]. This aspect of the signal was not considered above for simplicity. The color of the probe pulse is chosen so that the probability for a probe-pump (*i.e.,* t<0) ionization pathway is below the noise level, allowing time dependent ionization to occur only at positive time delays. There is a constant background component to the photoionization signal at all time delays, and this has also been subtracted out of the signals. Hence, the observed photoionization signal only shows the time dependent coefficient buildup behavior and the quantum interference of the superposition state as described in Eq. (4.4).

4.3 Experiment

The lithium sample is contained in a heat pipe at 1050 K and is photoionized by a three step excitation process. An overview of the laser system is given below, but details can be found in previous work [13,26], and in chapter 2. In this experiment, a narrow bandwidth continuous wave (cw) laser, an ultrafast amplifier system, and an optical parametric amplifier (OPA) are used, and all but the OPA are pumped by a 27 W argon ion laser. The frequency of the

cw laser is tuned to a specific $A^1\Sigma_u^+ \leftarrow X^1\Sigma_g^+$ resonance (606.954 nm) of Li_2, producing a pure launch state (v_A=11, J_A=28) on the first excited electronic state. The ultrafast regenerative amplifier is seeded by a 76 MHz oscillator to produce 180 fs [full width half maximum (FWHM)] ultrafast pulses at a 200 kHz repetition rate, near the 800 nm central wavelength with 8 nm (FWHM) bandwidth. These ultrafast pulses are split into two beams, with 25% of the light becoming the pump pulse and 75% of the light frequency doubled to pump the OPA. The resulting 15 mW OPA output is a train of nearly transform limited pulses with a 200 fs FWHM pulsewidth and a central wavelength of 640 nm. The OPA output is variably time-delayed relative to the pump pulse via a precision delay stage. This OPA wavelength is used since in the pump-probe regime, it yields a strong photoionization while producing very little photoionization in the probe-pump regime [see Fig. 2.1].

To shape the pump pulse, it is sent through a dispersion free pulse shaper [27,28]. In the pulse shaper's Fourier plane, a liquid crystal spatial light modulator (SLM) is used to shape the spatially dispersed pump light by independently attenuating and/or applying phase to 128 individual frequency components (SLM pixels) of the pump light. The central frequencies imaged onto the SLM pixels are separated by approximately 4 cm^{-1} with a single frequency spot size of approximately 1.7 pixels. Normally, the 8 nm FWHM pulses are imaged onto the SLM to achieve a bandwidth of 40 pixels FWHM. Pixellation and finite spot size effects limit the temporal pulse shaping to be within a window of about ± 4 ps around time zero.

The cw laser, pump, and probe pulses intersect in the interaction region in the center of the heat pipe. The ions are produced between two parallel plates separated by 1 cm with a 10 V potential applied across the interaction region. The cw light is optically chopped, and the resulting current is detected with a lock-in amplifier that is synchronized to the cw modulation.

To study the effects of nonresonant frequencies, two classes of pulse shapes have been used to enhance transient photoionization effects, shown in Fig. 4.2. The first class, which has previously been studied in the context of a single resonance [17] ("chirp-type spectrum"), has a quadratic phase applied across the frequency spectrum around each resonance with the form $\varphi(\omega)=c\Delta^2 + \varphi_k$, where $\Delta=\omega_i-\omega$ is the detuning from the nearest resonance, and φ_k is a constant phase [see Fig. 4.2a]. The constant phase, φ_k, is applied to the entirety of one of the control channels to control the phase of the wave packet interferences. Here, the time delay is adjusted by varying the magnitude, *c*, of the quadratic phase. An optimal phase mask for population transfer comprises the second class, called the "phase-jump spectrum"; this phase mask involves the application of $\pi/2$ and $-\pi/2$ radians above and below resonance, as established in several recent works [see Fig. 4.2b] [13,18]. The resonant portion of the control channel is defined here as a block of two pixels (~8 cm^{-1} FWHM) centered on a specific transition, chosen to avoid attenuating the long time delay signal by diffraction [13]. So, in effect, "resonance" actually refers to the smallest practical bandwidth achievable by our pulse shaper around each transition. To vary the timing of the optimal photoionization, a linear phase versus wavelength is added to the nonresonant

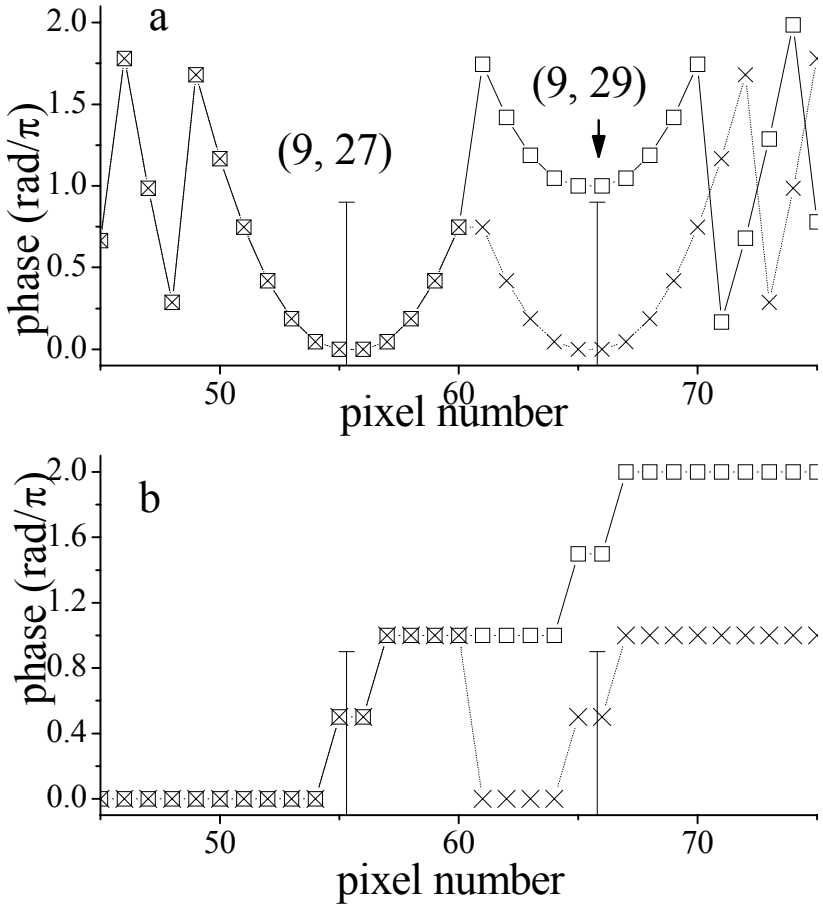

Figure 4.2. Phase mask classes used in this chapter. In both panels, quantum state resonances (v_E=9, J_E=27 & 29) are marked with vertical lines. Relative phase offset of 0.0 and π radians between control channels are represented by crosses (X) and squares (□), respectively. Panel a: Chirp-type spectra. The degree of quadratic phase, c, is defined by $\varphi(\text{pixel}) = c \times (\Delta_{\text{pixel}})^2$ where Δ_{pixel} is the separation in pixels from the nearest resonance. Panel b: Phase-jump spectra. A phase of $+\pi/2$ and $-\pi/2$ is added to the frequencies above and below resonance, respectively. A linear phase of $\varphi(\text{pixel}) = c \times \Delta_{\text{pixel}}$ is added to the phase masks to induce a time shift in the population transfer (not shown). The phase on pixel 56 is always the same as that on pixel 55, and the phase on pixel 66 is always the same as that on pixel 65.

portion of the phase-jump phase profile. As in the case of the chirp-type spectrum, the relative phase of the wave packet states using the phase-jump spectrum is manipulated by adding a constant phase to only one of the control channels.

4.4 Results and Discussion

This section will first analyze the ability to control quantum beats while applying a previously studied chirp-type phase mask around each state, but extended to a quantum superposition. Next it will be shown that the phase jump spectrum gives a much greater enhancement in the transient photoionization. It will further be shown that the timing of the peak photoionization for the phase jump spectrum can be much more precisely controlled than the chirp-type spectrum. Finally, the nonresonant contributions to the photoionization will be compared to a simple model to quantify the degree to which the quantum states in the superposition can be independently controlled.

To demonstrate the separability of the population transfer dynamics from the wave packet oscillations, we first examine the previously studied case of the chirp-type spectrum, with results for the two states at the magic angle [Eq. 4.4b] and parallel probe minus the magic angle [Eq. (4.4c)], shown in Fig. 4.3[49]. The population transfer dynamics in the upper part of the figure show several traits of the buildup produced by a strictly chirped pulse. After time zero, there is a peak in the excited state population followed by a short period of ringing. After just a few picoseconds, this ringing decays, leaving a constant value for the

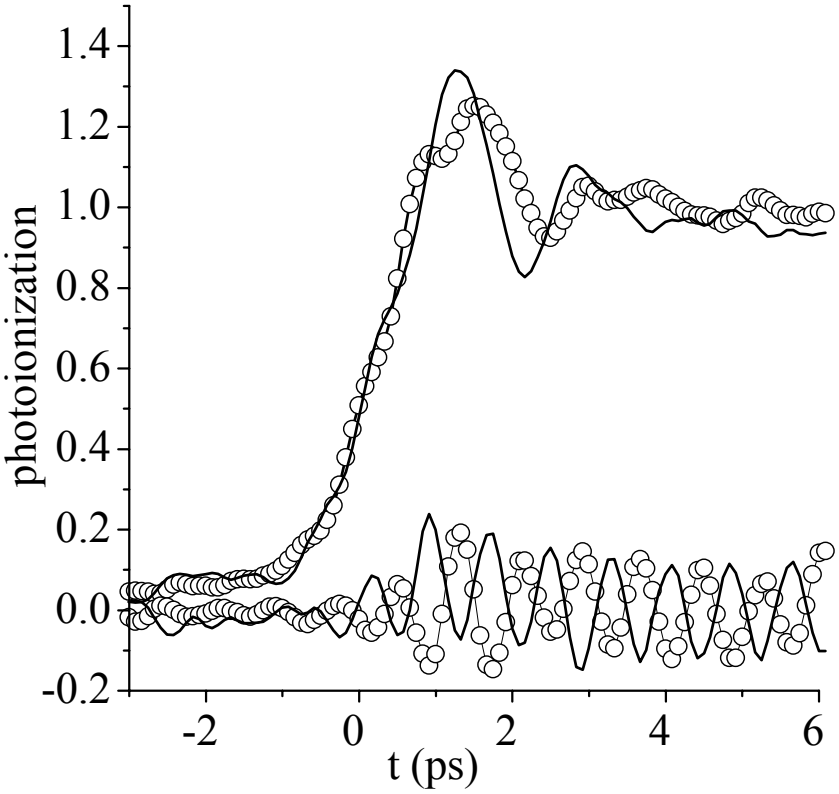

Figure 4.3. Chirp-type pump spectrum transients. The upper solid line and circles (○) represent the magic-angle probe transient for π and 0 radians relative phase between control channels, respectively, and a chirp factor of 0.2. The lower solid line and circles (○) represent just the coherent oscillations produced with the same phase masks as above.

excited state population. Notice that these traits are present for both zero and π relative phase between the control channels, and in both cases there is a peak in the excited state population around a planned delay time of 1.2-1.3 ps, depending on the degree of chirp, in this case 0.2 chirp factor. The coherent oscillations, which are simply the difference between the parallel and magic-angle probes, are also predictably controlled. Clearly, a π phase shift of one coherent oscillation relative to the other can be induced, which is simply a result of adding π phase to only one of the resonant control channels. Additionally, around 1.2 ps, the amplitude of the coherent oscillations passes through a maximum, as expected from Eq. (4.4a). The combination of the population transfer dynamics and the wave packet interferences produces a clear peak in the photoionization signal at 1.2 ps despite the slightly decreased population transfer using zero phase offset between control channels.

The analysis of the chirp-type spectrum above establishes that both the population transfer dynamics and wave packet interferences can be independently controlled. This section now explores more optimal phase masks to maximize the photoionization due to the population transfer dynamics in conjunction with the interference of two states at specific short pump-probe time delays.

Several magic angle and parallel pump-probe data are summarized in Fig. 4.4. A pump-probe transient obtained with the phase-jump spectrum of Fig. 4.4 clearly shows an enhancement in the excited state population, in addition to the proper phasing of the coherent oscillation at t=0, shown in Fig. 4.4a. In these signals, the background signal has been subtracted out, and the remaining

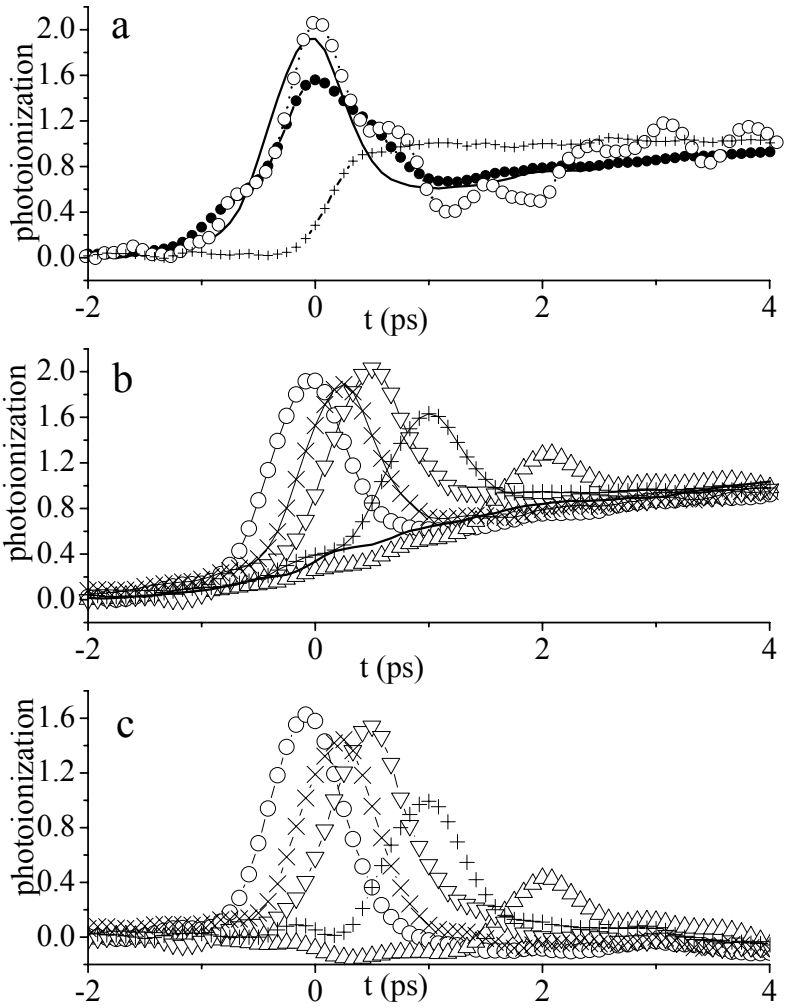

Figure 4.4. Phase-jump pump spectrum transients. Panel a: Magic angle probe traces produced using zero phase offset (●) and π phase offset (solid line) between the control channels, and parallel probe photoionization signal (○) for zero control channel phase offset. A trace produced by an unshaped pump pulse with magic angle probe (+) is included for reference. Panel b: Population transfer traces adding varying degrees of linear phase to nonresonant frequencies with π phase offset between wave packet resonances. The nonresonant contributions were timeshifted to have peak photoionization occur at 0.0, 0.25, 0.5, 1.0, and 2.0 ps (○, X, ▽, +, and △, respectively). The solid line represents an attempt to shift the nonresonant contribution to a time beyond the capabilities of the experimental apparatus, resulting in a purely resonant excitation effect. Panel c: Nonresonant effects on the population transfer at various time delays. Traces were generated by subtracting the purely resonant contribution of the population transfer trace from the total population transfer signal (same symbols as in panel b). photoionization signal has been normalized to the signal at t=∞, which has been shown to

depend only on resonant wavelengths and hence is constant in these studies[25]. Two

population transfer traces (magic-angle probe) are shown, along with a total wave packet signal (parallel probe) that is designed to have a maximum in the quantum beat at the same delay (0.0 ps) as the maximum in the population transfer. The population transfer traces use phase masks with 0 and π relative phase between two control channels, and the full wave packet signal is set to have 0 relative phase between the two control channels [the X's in Fig. 4.2b]. Both population transfer traces show a peak at the same pump-probe time delay, with the case of π relative phase between control channels [the □'s in Fig. 4.2b] having the larger peak amplitude.

Of all relative phases between control channels of the phase-jump class, the case of zero relative phase is the least optimal for population transfer. This is so because all of the wavelengths between the two wave packet states in one control channel maximally destructively interfere with the buildup of the other control channel. For example, the light on pixels 57-60 maximally and destructively interferes with the buildup of state (9,29), where the control channel includes pixels 61-128. Even so, the wave packet interference produces a global maximum in the photoionization at 0.0 ps pump-probe delay. A net gain in the photoionization relative to a non-interfering condition can always be achieved as long as the wave packet interference amplitude exceeds one minus the degree of independent control, or when $|pr_1 pr_2||c_1(t)c_2(t)|>1-I_{PTi}$ from Eqs. (4.3) and (4.4). Note that for a multiple state superposition, $1-I_{PTi}$ increases, but simultaneously multiple coherent oscillations can constructively interfere, counteracting the decrease in degree of independent control inherent to the smaller control channel sizes of a multiple state system.

In Fig. 4.4b several population transfer traces are shown for the phase jump spectra with varying amounts of linear phase added just to the nonresonant frequencies; these traces are generated using only π relative phase between the wave packet resonances. The peak height and time for each trace is noted and will be discussed later. Evident in this figure is that for each trace there is a slow, monotonic buildup (>4 ps) of population attributable to resonant (and very near resonant) frequencies coupled with a much shorter timescale population transfer attributable to nonresonant frequencies. By subtracting the resonant portion of the traces from the full traces, purely nonresonant effects can be analyzed [see Fig. 4.4c]. The time-shifted nonresonant contributions to the population transfer show peak widths between 750 fs and 790 fs FWHM. This data will be used later to quantify the degree to which the superposition states can be independently controlled.

The phase-jump spectrum permits a higher degree of coherent control than the chirp-type spectrum by obtaining a greater enhancement in the population transfer and by allowing more precise timing of the peak of the photoionization signal [see Fig. 4.5]. Figure 4.5a shows the peak excited state populations as a function of time for the two pulse shape classes. At short times, the phase-jump spectrum doubles the excited state population, whereas the chirp-type spectrum shows a maximum of 30 percent improvement of the photoionization signal. The

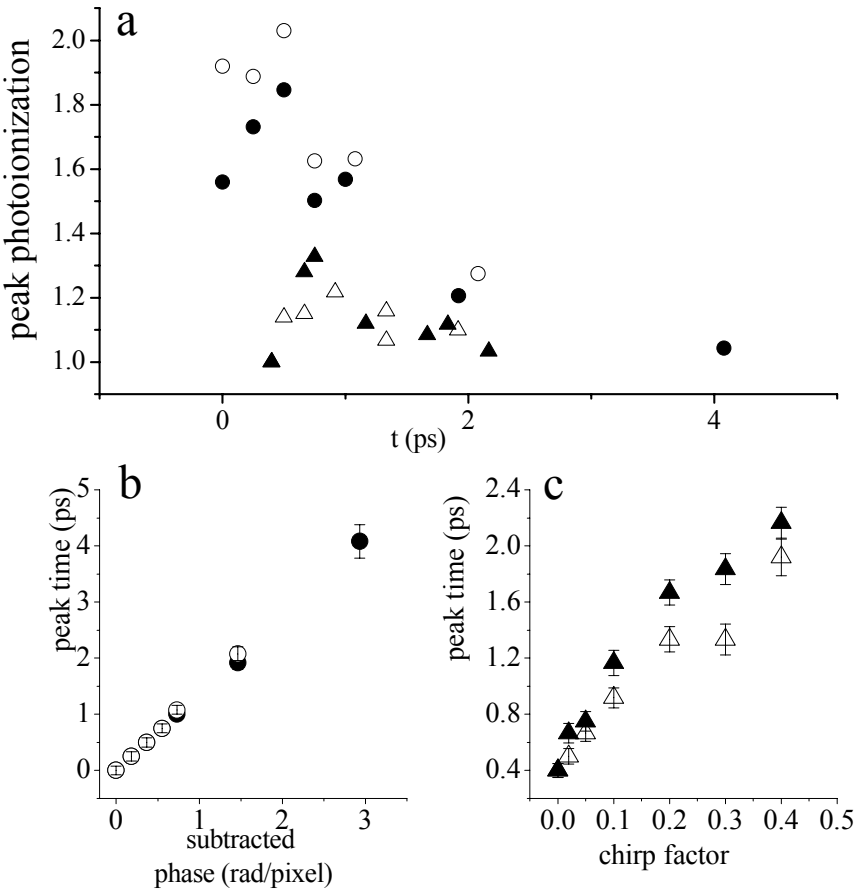

Fig. 4.5. Comparison of control capabilities using the phase-jump spectrum versus the chirp-type spectrum. In all panels, peak photoionization was monitored for various degrees of chirp type pulse shapes (triangles) and time shifted phase jump pulse shapes (circles). Filled symbols denote 0 relative phase between control channels, and open symbols represent π relative phase. Panel a: Peak photoionization comparison as a function of designed peak time delay. Data is collected by analyzing peak heights as shown in Fig. 4.4b, for example. The peak photoionization for the unshaped spectrum (*i.e.,* degree of chirp = 0) is represented by the chirp type spectrum data point at 0.4 ps and is normalized to 1. Panel b: Peak times as a function of degree of linear phase added to the standard phase-jump spectrum. Panel c: Peak times as a function of the degree of quadratic phase applied around each resonance for the chirp-type spectrum.

phase-jump spectrum shows greater population transfer enhancement than the chirp-type spectrum because the phase-jump shape assures that all non-resonant contributions come into phase simultaneously. This is in contrast to the chirp-type situation, in which only certain nonresonant contributions are in phase at any one time. For the phase jump spectrum, the timing of the peak of the photoionization signal can be controlled precisely, as shown in Fig. 4.5b. Note that in this regime the time delays of the peak photoionization signals are chosen by time-shifting the nonresonant contributions to the population transfer by simply adding a linear phase to the basic phase-jump pattern, based on the relation $\Delta t = d\phi/d\omega$. Relative to the phase-jump spectrum, the timing of the peak population transfer in the chirp type spectrum is not controlled as successfully. Notice in Fig. 4.5c that the peak timing follows a roughly linear relationship with the degree of chirp, but the deviation from a linear relationship is substantial. This can partially be attributed to wrap-around effects (*i.e*. the phase can only be defined modulo 2π) and "overlap" between the separate shaping channels of the phase mask. For example, the truly quadratic phase for the control channel around state (v_E, J_E)=(9,27) is defined to stop at pixel number 60, but with chirp factor c=0.2 and π relative phase between wave packet states [see Fig. 4.2b], pixel 61 fits well onto the quadratic progression. This in essence extends the size of the control channels. While this will be true for some chirp factors, it will not be true for others, accounting for the scatter in Fig. 4.5c.

The mechanism for the increase in population transfer for the phase jump spectrum can be attributed to off resonant Rabi oscillations. In the weak field limit, the Rabi frequency $\Omega(\Delta) = \left\{\Delta^2 + \left[\mu_{eg}\varepsilon\left(\Delta + \omega_{eg}\right)/\eta\right]^2\right\}^{1/2}$ reduces to $\Omega(\Delta)=\Delta$, since

$\left[\mu_{eg}\varepsilon\left(\Delta+\omega_{eg}\right)\right]^2 << \Delta^2$ for values of Δ with non-negligible electric field amplitudes [14]. Additionally, given that the amplitude of any nonresonant oscillation is proportional to $\varepsilon(\Delta+\omega_{eg})/\Delta$ [29], the total of all nonresonant contributions to the excited state populations can then be formulated as $c(t) \propto \int_{-\infty}^{\infty} d\Delta\left[\varepsilon\left(\Delta+\omega_{eg}\right)/\Delta\right]^2 \sin^2\left(\Delta t/2+\phi(\Delta)\right)$. Notice the similarity of this representation to Eq. (4.2). To bring all of these sine waves into phase at t=0, a phase mask with $+\pi/2$ and $-\pi/2$ radians applied to the positive and negative detuned wavelengths, respectively, must be implemented. At the resonant wavelength (*i.e.*, where $\Delta=0$), the optimal phase will be intermediate between the positive and negative detuning, or zero degrees. Thus we have the same optimal phase pattern as predicted by Eq. (4.2). In contrast, for the chirped phase pattern, not all nonresonant Rabi oscillations come into phase simultaneously. Rather, there is a series of partial recurrences in time; this is observed as a ringing in the signal.

To quantify the degree to which the two states in the experiments described here can be independently manipulated, a model based upon Eqs. (4.1) and (4.2) is implemented. This model accounts for the nonresonant and resonant contributions to the signal and is summarized in Fig. 4.6. Equation (2) is used to account for the nonresonant contributions to the population transfer:

$$c_n(t) = \frac{\mu_{eg}}{h}\sum_p \frac{\varepsilon(\omega_p)\exp[i(\Delta_p)t - i\varphi_p]}{\Delta_p}, \qquad (4.5)$$

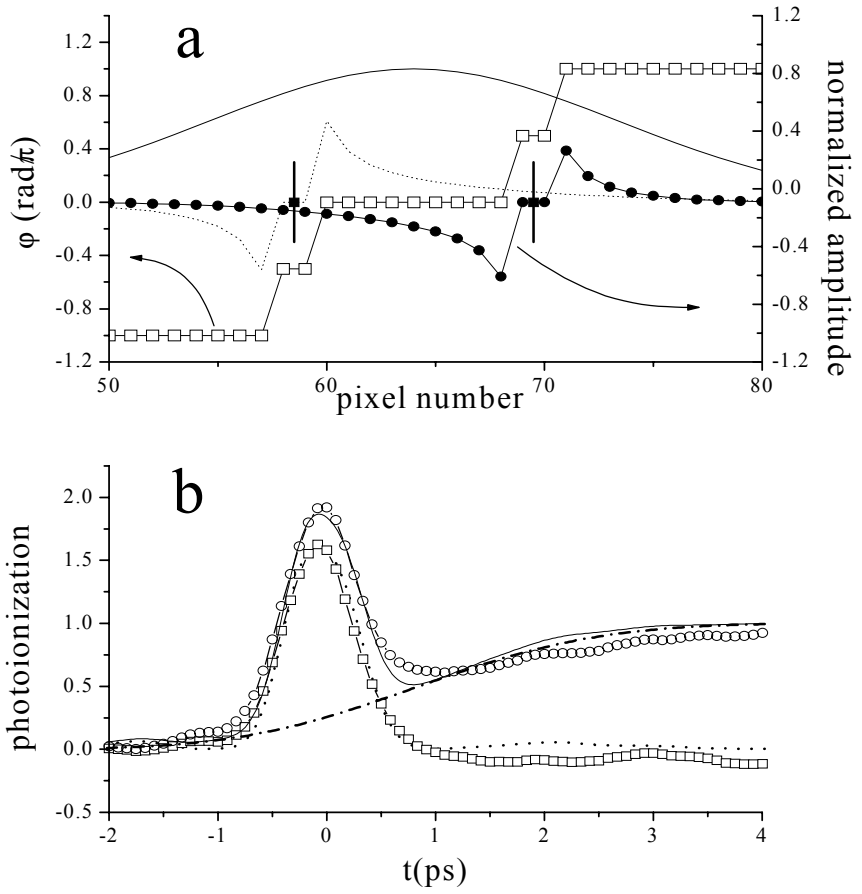

Fig. 4.6: Comparison of model results with experiment. Panel a: phase (□) and amplitude (●) [$\varepsilon(\omega_p)/\Delta_p$ from Eq. (4.5)] of the oscillations created by each pixel used to generate the nonresonant contribution to the model population transfer dynamics. Resonances are marked with vertical lines, and the electric field spectrum is given by the solid line. A second state (dashed line) is included for reference. Panel b: Comparison of model and experiment. The experimental nonresonant (□) and full population transfer traces (○) are compared to the model nonresonant (dotted line) and full population transfer (solid line) traces. The model resonant contribution is given by the dot-dashed line.

where the summation is over all pixels (p) of the SLM, with each pixel representing light of a specific frequency ω_p and phase φ_p. In essence, each pixel creates an oscillation with frequency Δ_p and amplitude $\varepsilon(\omega_p)/\Delta_p$. Transform limited pulses with Gaussian spectral widths equal to experimental observations are assumed, giving $\varepsilon(\omega_p)$, and the quantum states are assumed to be symmetrically located under the spectral envelope. In Fig. 4.6a, the values of $\varepsilon(\omega_p)/\Delta$ and φ_p are plotted. The amplitude of the light at the two pixels around each resonance is assumed to be zero here, but it is accounted for in the resonant portion of the model. The signal is then computed as a convolution of the excited state population, $|c_n(t)|^2$ with a 180 fs FWHM Gaussian probe pulse. The model population transfer dynamics fit very well with the experimental data, as shown in Fig. 4.6b. Using this model to quantify the influence of nonresonant frequencies, Eq. (4.2) shows that each state can be controlled up to 90% independently (*i.e.* I_{PTi}=0.90).

The resonant contribution to the signal is modeled using Eq. (4.1). The electric field is assumed to be transform limited with a bandwidth for excitation equal to approximately 10 cm^{-1} FWHM, which corresponds to the light imaged onto two pixels. Each quantum state is assumed to be located at the central frequency of its respective narrow bandwidth region to best mimic experiment and to minimize computational artifacts related to the singularity at Δ=0. This component of the modeled signal shows a slow, monotonic increase in the excited state population, just as one would expect from a several picosecond transform limited pulse. When the resonant and nonresonant components of the model are added together, they closely follow the experimental signal, as shown in Fig. 4.6b. A similar analysis was performed on the results using phase jump spectra with 0 radians relative phase, with similar outcomes, further supporting the

validity of this model. In future work, the effects of changing the energetic spacing between states will be used to experimentally verify the bandwidth considerations presented earlier.

We have shown the ability to independently implement the coherent control of both the population transfer coefficients and quantum interferences to two states in a superposition. Additionally, we have shown that the optimal pulse shape for transient population transfer in the weak field regime is characterized by nonresonant wavelengths that are shifted by $\pi/2$ and $-\pi/2$ radians relative to the resonant wavelengths. Using a simple model based upon the assumption that an ultrafast transition can be described by a collection of driven oscillators, we have quantified the degree to which the two states in the superposition can be independently controlled. This work should be instrumental for designing coherent control pulse schema and for understanding solutions found by various learning algorithms.

Chapter 5

Dynamic Phase Control

5.1 Introduction

The study of coherent control to manipulate molecular systems has generated numerous tools that can be useful for directing a system under optical, especially ultrafast, excitation[12, 13, 22, 26, 32, 50-57]. The tools of coherent control may be applicable to quantum computing, where superpositions of quantum states, or qubits, are used to perform computational operations[58]. Crucial to being able to perform quantum operations is the ability to manipulate individual states within qubits. Basic computations have been performed on spin systems using Nuclear Magnetic Resonance with considerable success[59-62]. Optically manipulated systems using trapped atoms and ions also show promise for quantum computation by using narrow bandwidth lasers to resonantly control particular transitions between states[63, 64]. Wide bandwidth, ultrafast pulses have been proposed as a means to implement quantum computational operations using the relatively dense states inherent to single quantum dots and even molecules[32, 54-57]. Given the relatively short decoherence times (<100 ns) of these more complex systems, the use of ultrafast laser sources is valuable to perform sufficient numbers of operations for meaningful computations. This chapter explores a mechanism for using ultrafast pulse shaping techniques to manipulate individual states in a molecular superposition, specifically multiple

rotational states in an excited electronic state of the lithium dimer. As an example of using nonresonant frequencies to control the amplitude of molecular rotational states, a transient Z-gate is implemented. Using an ultrafast pulse with sufficient bandwidth to encompass resonant transitions to two excited states, one state of the two state superposition will have its sign unchanged while the other will undergo a sign inversion. The operation is transient in nature, so it can not be used for actual computation, but the results illustrate new possibilities of using optical pulse shaping techniques for individual state manipulation.

In the previous chapter, it has been shown that resonant frequencies can be used to control the phases of states involved in a wave packet[7, 48], and it has also been shown that nonresonant frequencies can be used to transiently manipulate the absolute amplitude of resonant transitions, even in the weak field [33, 65]. One additional aspect of transient, ultrafast control of wave packet phases has not been demonstrated: *i. e.* the transient phase of a wave packet can be controlled by using nonresonant frequencies. As in any first order process, though, the final wave packet phase and amplitude at long times are determined by the resonant frequencies, as is expected[12]. This will be demonstrated by observing the coherence only portions of the signal as written out in Eq. (4.4c)

We show in this chapter that the wave packet phase can be induced to undergo a π phase shift at time zero relative to long times. Assuming that one contributing state in the superposition has a constant phase at all times, the signal shows a change in sign because of a transient sign inversion of the second state. This dynamics is accomplished by summing resonant and nonresonant

contributions with the same sign for one state while summing resonant and nonresonant contributions with opposite sign for the other. The amplitudes of the relative contributions of each effect are manipulated so that the nonresonant contribution dominates at short times for the opposite sign but disappears at long times. This process of inverting the sign of one state of a superposition while leaving the second unaltered is characteristic of a quantum computational Z-gate, which in this case is constructed in a transient fashion.

This example of controlling the dynamic phase of a wave function in the weak field regime provides a rather clear illustration of the limitations and possibilities of precise control of molecular systems. As long as the intensity of the electric field is weak enough to disregard intensity dependent Rabi oscillation effects, pure phase shaping of the ultrafast pulses fully controls the dynamics of the effects observed. In Sec. 5.2, a theoretical framework for these experiments is presented using first-order perturbation theory. In Sec. 5.3 is presented a categorization of the resonant and nonresonant effects that are used as tools in these experiments. Finally, experimental results are presented, discussed, and quantified in Sec. 5.4.

5.2 Theory

This chapter develops a method to induce a transient sign change in one state of a two state superposition, or wave packet, using language consistent with the formalisms of quantum computing. The wave packet consists of two states that are excited coherently, so that:

$$\Psi'(t) = c_0(t)|0\rangle + c_1(t)|1\rangle + c_2(t)|2\rangle, \qquad (5.1a)$$

where $c_0(t)$ is the launch state wavefunction amplitude, $c_1(t)$ and $c_2(t)$ are the complex excited state wavefunction amplitudes to be described below, and |0>, |1> and |2> are the time dependent rovibrational wavefunctions [*i. e.* $|1(R,\theta,t)\rangle = |1(R,\theta)\rangle e^{i\omega_1 t}$] in the superposition [see Fig. 5.1]. The detection scheme is only sensitive to |1> and |2>, so the effective wave packet can be reformulated as

$$\Psi(t) = c_1(t)|1\rangle + c_2(t)|2\rangle . \qquad (5.1b)$$

As described previously[33, 48], the photoionization signal using parallel, linear pump and probe polarizations can be written as

$$S(t) \cong |pr_1|^2 |c_1(t)|^2 + |pr_2|^2 |c_2(t)|^2 + 2|pr_1 pr_2 \| c_1(t)c_2(t)| \cos[\Delta\omega t + \Delta\varphi(t)] , \quad (5.2)$$

where the only change from Eq. (4.4a) is the explicit time dependence of $\Delta\varphi(t)$. Since the multiphoton ionization pathway from the launch state (pr_0) is weak, $pr_0 << pr_1, pr_2$, so all launch state terms are left out of the signal, and the time dependent signal only shows the dynamics of the excited states.

In these experiments, the probe step consists of an ultrafast pulse of a different color (645 nm) than the pump pulse (801 nm) [33] so as to avoid any ambiguities in the contributions to the signal when the probe comes before the pump. With the 645 nm probe pulse, the probability for a probe-pump (*i. e.,* t<0) ionization pathway is below the noise level, allowing time dependent ionization to occur only at positive time delays. This allows the transient populations and coherent oscillations to be measured reliably around t=0.

In Eq. (5.2), the $c_n(t)$ factors have the same functional form as Eq. (4.2), with nonresonant contributions to the coefficient being $\pm\pi/2$ out of phase with

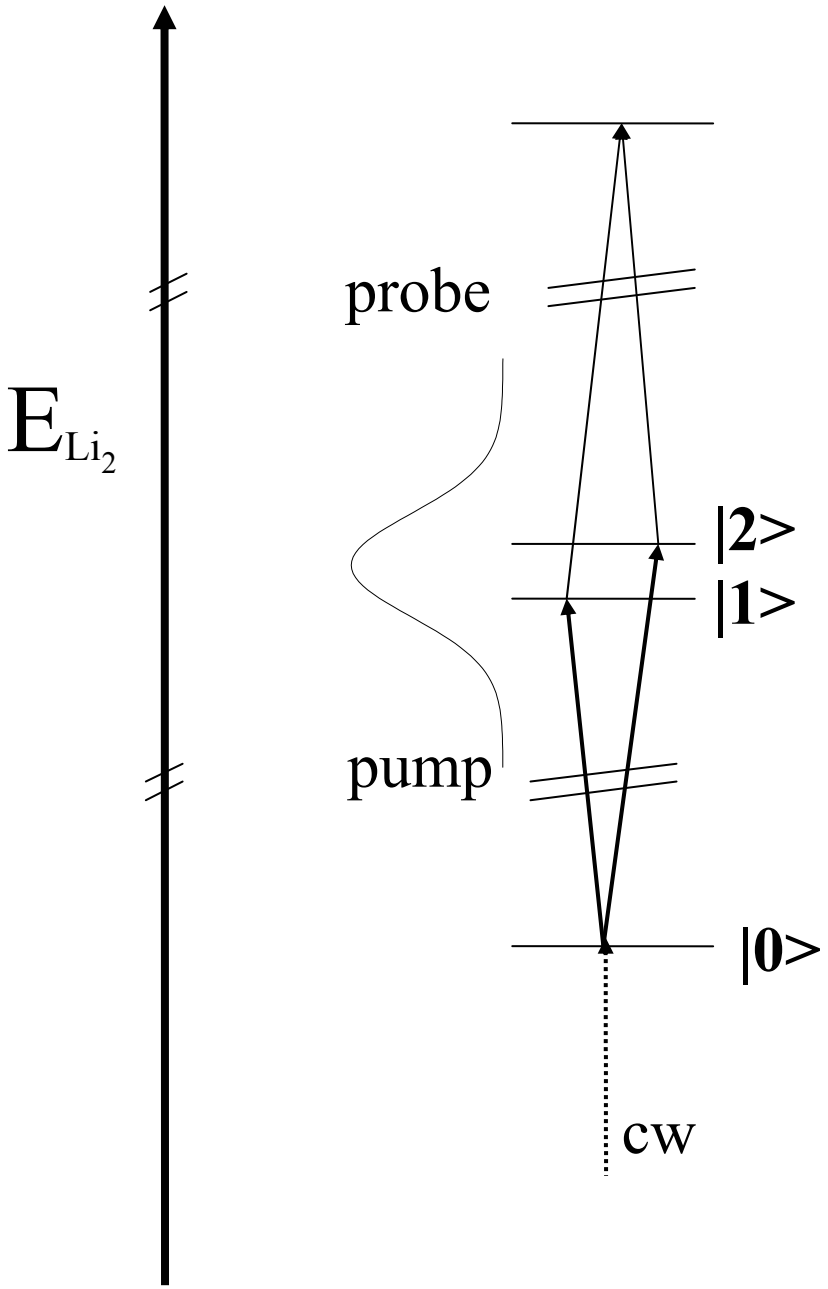

Figure 5.1. States involved in excitation scheme. A cw laser excites from the X electronic state to a pure launch state (state |0>) on the A electronic state. A wide bandwidth 801 nm ultrafast pump pulse excites a superposition of states (states |1> and |2>) on the E electronic state, which is subsequently ionized by a time delayed 645 nm ultrafast probe pulse.

respect to the resonance and with a $1/\Delta$ dependence. Notice that these effects result in a complex amplitude $c_n(t)$, which under the conditions imposed in these experiments will remain primarily real. The manner in which the various contributions interact is explored in the next section where it is demonstrated how to change the wavefunction sign.

In this chapter, a transformation of the qubit in Eq. (5.1b) is mathematically equivalent to a quantum computational Z-gate. Using a matrix formulation, the action of the ultrafast pulse on the prepared superposition transforms the system as a single qubit Z-gate:

$$\begin{bmatrix} c_1(f) \\ c_2(f) \end{bmatrix} \approx \begin{bmatrix} 1 & 0 \\ 0 & -1 \end{bmatrix} \begin{bmatrix} c_1(i) \\ c_2(i) \end{bmatrix}. \tag{5.3}$$

First, a superposition is prepared such that at t=0.0 ps, the two excited states have amplitudes of opposite sign so that $c_1 \approx 1$, and $c_2 \approx -1$. The electric field then drives the system so that the sign of c_2 changes, leaving $c_2=1$. Although this transformation can be analyzed in terms of a series of three correlated pulses (*i.e.* pulses with a defined relationship between the carrier frequency phases), it will be explained in terms of the spectral contributions to the signals, as given in Eq. (4.2).

5.3 Experiment

In the experiments described in this chapter, the experimental setup is the same as chapter 4. What are varied are the pulse shapes that are investigated as well as the analysis of the data. As a result, this section will focus on the basics of different

types of excitation mechanisms and pulse shapes, as if they were simply experimental tools.

To investigate phase mask effects, the available spectrum is defined as consisting of two spectral channels separated at the energetic midpoint between the two resonant transitions. A global phase offset can be added to the channel for state |2> in order to control the long time wave packet phase. Within each channel, *i. e.* for each state, resonant and nonresonant contributions to the excited state wave function coefficient are independently controlled. See Fig. 5.2 for one phase mask that is used to add the resonant and nonresonant contributions of the excited state coefficients along with the corresponding observed time domain evolution. In Fig. 5.2a, it is shown that a small bandwidth region around each resonance (~8 cm^{-1} each) is assigned a phase halfway between the positive and negative detuned nonresonant frequencies. The effect of these narrow bandwidth regions is a monotonic increase in the excited state coefficient, as shown by the triangles in Fig. 5.2b , taken with magic angle probe so there are no wave packet recurrences. This will be referred to as the resonant contribution. The applied π phase shift between positive and negative detuned frequencies around each resonance compensates for the intrinsic spectroscopic π phase shift of the nonresonant contributions above and below the resonances. This allows the nonresonant contributions to cooperate on short timescales, as seen by the circles in Fig. 5.2b. The solid line in Fig. 5.2b gives $|c_1(t)|^2 + |c_2(t)|^2$, which has been normalized. Assuming that the crosstalk between control channels for the two coefficients is insignificant [see previous chapter][33], which is achieved when

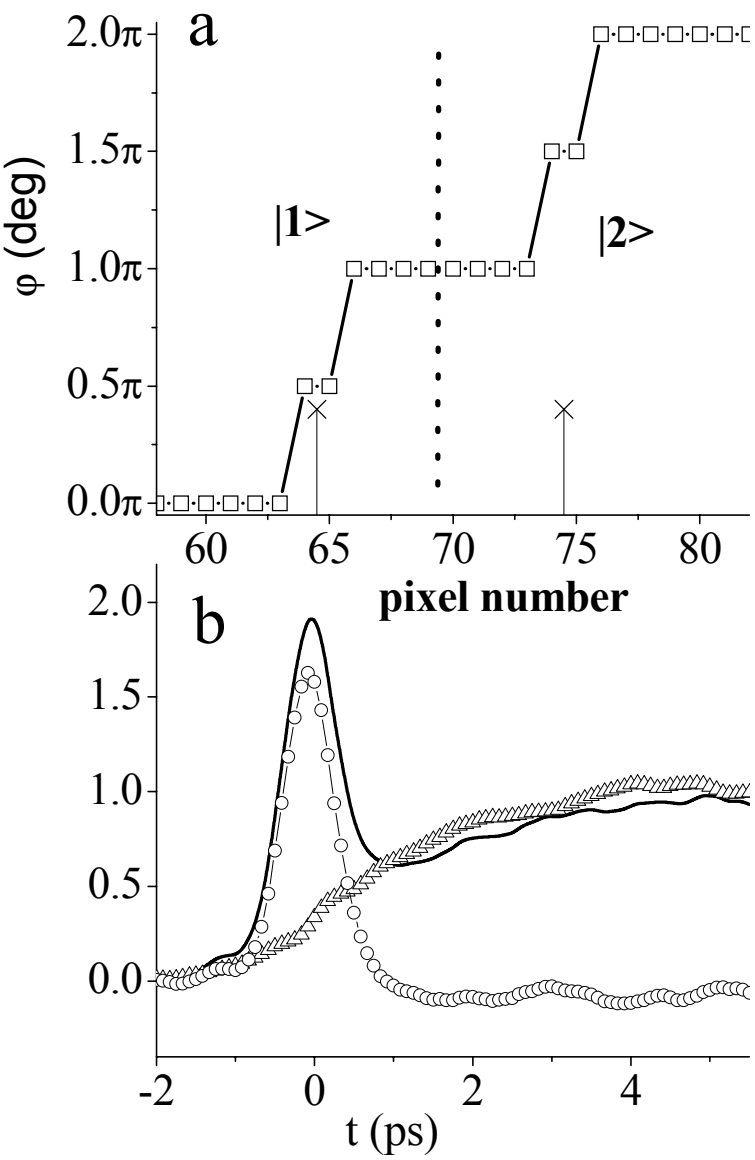

Figure 5.2. Phase shaped population transfer traces. Panel a: Phase mask used to maximize population transfer at t=0.0 ps. The applied phase mask is given by (□), and resonances are marked with (X). The applied phase masks near each resonance (*i. e* .in each channel) are identical, assuring that both states follow the same excitation pathway. Panel b: Magic angle traces (to suppress the rotational quantum beats) using the applied phase mask of panel a. The solid line represents the total population transfer signal, the (△) shows the resonant only contribution, and the (○) gives the nonresonant contribution, which is just the difference between the two traces.

the two resonances are spaced far apart energetically, $|c_1(t)| \approx |c_2(t)|$. By taking the square root of the signal and renormalizing, a measure of each coefficient is obtained. This signal shows that at the times of interest in this paper, t=0 and t=∞, $|c_1(t)|$ = 1.4 and 1.0, respectively. This information will be used later to quantify the manipulations of coefficient $c_2(t)$.

Figure 5.3 is a schematic diagram of the signed *amplitude* [*i.e.*, $c_n(t)$, not $|c_n(t)|^2$] of the excited state coefficients. The traces in Fig. 3a-b are calculated from parameters of the square root of the cooperative signal as described above. Given that these contributions add to yield the amplitude of $c_n(t)$, the resonant and nonresonant effects within each channel can be subtracted as well as added. This is done by multiplying either the resonant or nonresonant contribution by -1. Fortuitously, in the complex plane, multiplication by -1 is identical to the addition of π phase, which is accomplished by the application of π phase to the appropriate pump wavelengths. As can be seen in the modeled coefficients in Fig. 5.3b, simply subtracting the nonresonant contribution from the resonant gives a value of -0.7 for $c_2(0)$. In these experiments, state |1> is manipulated to be a sum of the resonant and nonresonant contributions with the same sign, while state |2> consists of a sum of contributions with opposing signs. Since the coefficient for |2> reflects a difference, the absolute amplitude of this negative coefficient can be increased in one of two ways: by increasing the negative part or by decreasing the positive part. Here, the positive contribution due to the resonant frequencies has been time shifted by 1.0 ps by applying a simple linear phase mask to the resonant regions [solid line in Fig. 5.3a] with the nonresonant contribution unaltered. To

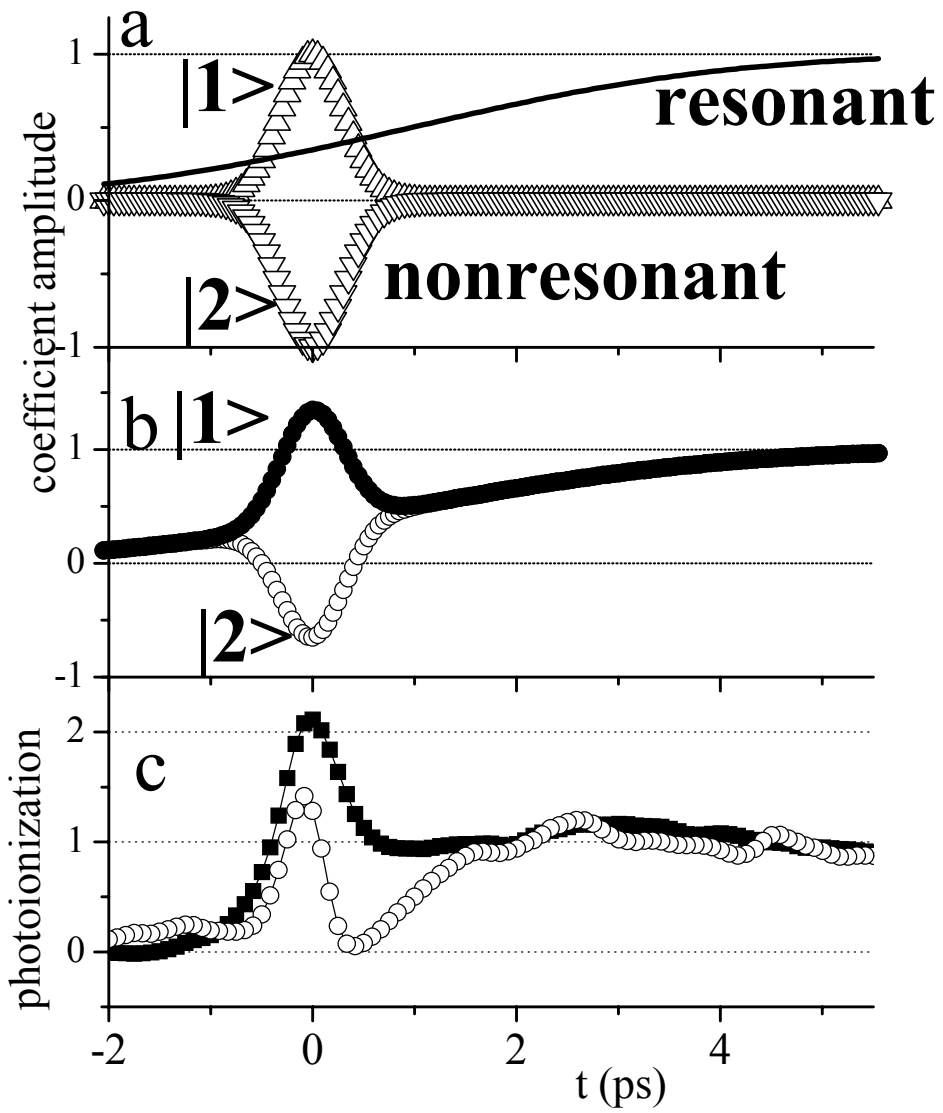

Figure 5.3. Resonant/nonresonant interaction scheme for inducing sign inversion. Panel a: Calculated resonant and nonresonant contributions to the population transfer. The solid line is the resonant contribution time shifted by 1.0 ps. The (△) and (▽) reflect the nonresonant contribution for states |1> and |2>, respectively, when inducing a sign inversion. Panel b: Total excited state coefficient evolution using contributions from panel a. The (●) show the time evolution for state |1>, and (○) shows the time evolution for state |2>. Panel c: Experimental photoionization traces for a single state with a phase mask that adds resonant and nonresonant contributions (■), and a phase mask that subtracts the resonant and nonresonant contributions (○). Note that the photoionization correlates with the square of the amplitude coefficients.

demonstrate the effects experimentally, each type of phase mask was applied to a pulse exciting the v_E, J_E=7, 39 state, and the results are shown in Fig. 5.3c. The light near state v_E, J_E=7, 41, spaced over 62 cm^{-1} away, was attenuated to make sure that it was not excited. Excitation with the additive phase mask shows the expected transient peak at t=0.0 ps. Excitation with the subtractive phase mask shows the photoionization goes nearly to zero at 0.42 ps. It is at this time that the sign of the coefficient inverts and the phase quickly changes. These traces show the total photoionization, so they actually reflect $|c(t)|^2$, but it is quite clear from the data that the subtractive phase mask changes the coefficient sign of this isolated state.

5.4 Results and Discussion

To serve as a reference, a case where the dynamics of the population transfer is controlled identically for both states involved in the wave packet is shown in Fig. 5.4 {see [33]}. Here, the resonant and nonresonant contributions to the signal are added together with the same sign for both states |1> and |2>. The upper part of Fig. 5.4a shows that there is a peak in the excited state coefficients at t=0.0 ps. The difference between the full signal and the excited state coefficient signal yields purely the coherence signal, which is shown as the circles in the lower part of Fig. 5.4a. This is obtained from parallel and magic angle pump-probe polarization signals, respectively. Notice that the coherence signal only appears after the excited state coefficients become nonzero (*i.e.* after t=-1.0 ps), and that it has an overall constant temporal phase of π radians.

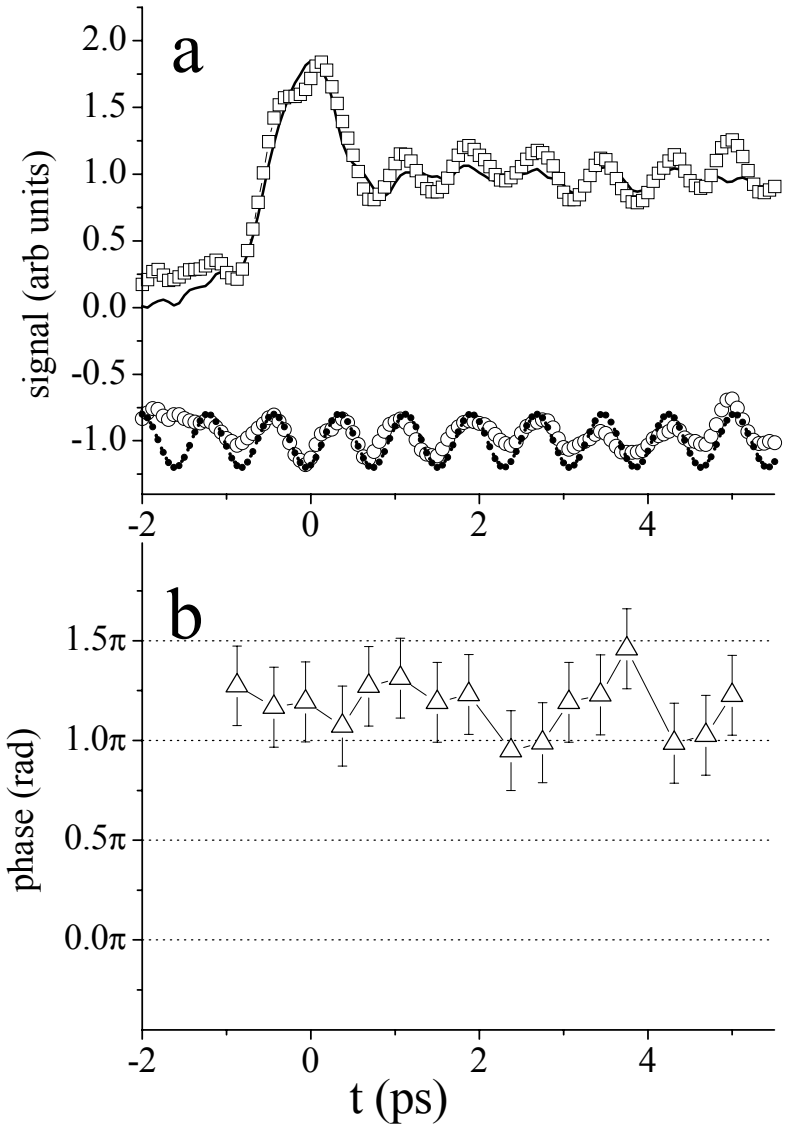

Figure 5.4. Phase evolution using the same phase mask for each resonance. Panel a: Pump-probe signals using phase mask of Fig. 5.2. Total signal (□) and population transfer (solid line) traces are shown on the top. Also shown is the coherence-only signal (○) as well as a single cosine fit (dotted line). The coherence-only signal and fit have been vertically offset for visibility. Panel b: Instantaneous wave packet phase. The maxima and minima of the coherence-only signal are compared to the fit to generate the instantaneous phase. The wave packet phase remains relatively constant from the onset of the signal until long times.

To show that the phase of the wave packet oscillation remains constant during the population transfer process, the signal up to 6.0 ps pump-probe delay was compared to a cosine wave that is generated to fit the coherence signal between t=6 ps and t=30 ps. The signal is fit only at times after 6 ps to avoid potential uncertainties introduced by a changing wave packet phase during the population transfer process. The maxima and minima of the coherence signal are compared to the fit, and the time offset of each peak relative to the fit is used to determine the instantaneous phase, plotted in Fig. 5.4b. As is evident in Fig. 5.4b, the phase shift of the experimental trace is centered around $1.16\pi \pm 0.25\pi$ (maximum range) radians over all time delays up to 6 ps. This comes as no surprise, since no effects have been introduced to change the instantaneous wave packet phase.

The case of subtracting the nonresonant contributions from the resonant contribution is the main point of this paper and is shown in Fig. 5.5. The phase mask that is used to induce a sign change in state |2> is shown in Fig. 5.5a. Note that the phase applied to the nonresonant contributions around |1> is not changed from the additive case, as shown in the previous section. In contrast, the phase applied to the nonresonant contributions around |2> is inverted; the nonresonant contributions have an additional π phase shift relative to the resonant ones, which is equivalent to a multiplication by -1, as explained previously. The corresponding signal traces from Fig. 5.5b show the expected population peak around t=0.0 ps, just as when the contributions were added together. Note that this trace must remain positive, since the observed signal is a sum of squares for

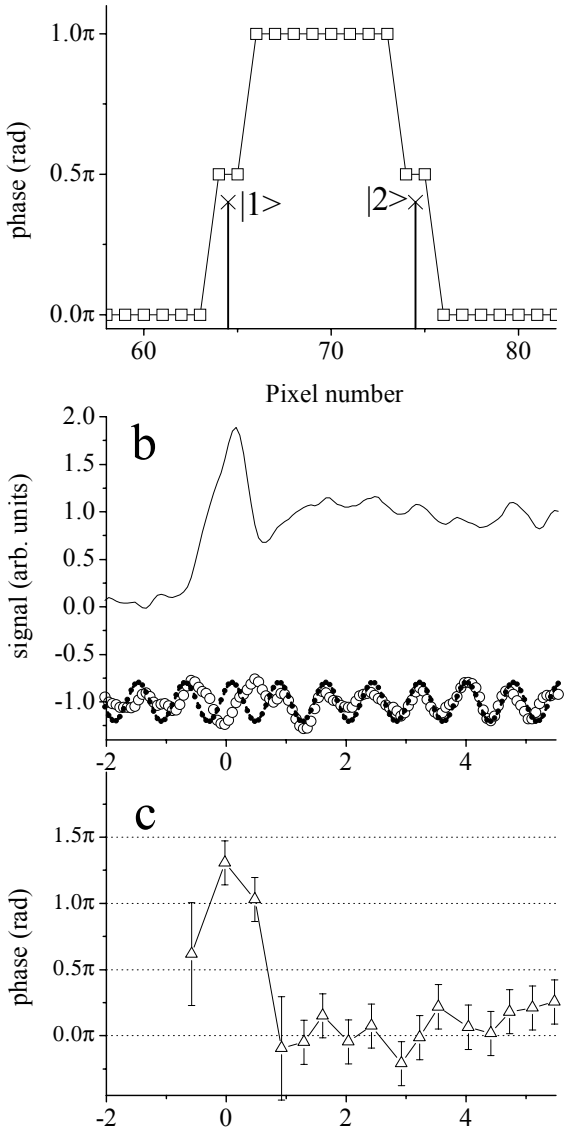

Figure 5.5. Sign inversion wave packet data. State |1> is programmed to behave the same as in Fig. 5.4, but state |2> is programmed to change sign. Panel a: Phase mask applied to induce sign inversion. The applied phase is given as (□), and the resonances are given by (X). Notice that the relative phase between resonances is 0.0 radians. Panel b: Pump-probe signals using the phase mask of panel a. Population transfer (solid line) trace is shown in addition to the coherence-only signal (○) as well as a single cosine fit (dotted line). The coherence-only signal and fit have been vertically offset for visibility. Panel c: Instantaneous wave packet phase from onset of excited state population. The wave packet phase undergoes a π shift from t=0.0 ps to t>1.0 ps.

both states |1> and |2>. A critical difference in this case occurs in the coherence only portion of the signal, which contains information about the wavefunction sign. In Fig. 5.5b it is apparent that around t=0.0 ps, the quantum beat portion of the signal exhibits a phase of ~π even though the relative phase between the resonant frequencies is 0.0 radians. The instantaneous phase graph of Fig. 5.5c displays a π phase shift in the region around t=0.0 ps relative to t>2.0 ps. This shows that there is indeed a temporally dynamic phase of one state in the wave packet relative to the other. In fact, it shows that the sign of one state has changed temporarily relative to the other.

A full discussion of the effects seen here can not be made without a brief mention of the nonidealities at play in this pulse shaping scheme. As was mentioned earlier, the resonant contribution to the signal was shifted to a more positive time to minimize the interactions between it and the nonresonant contributions. An example when the nonresonant contribution to the signal is not shifted in time is shown in Fig. 5.6. It is quite clear in this figure that the phase deviates substantially from either 0 or π phase. The dynamics at play here are highly sensitive to the positions of the resonances relative to the cutoffs between those spectral regions treated as "resonant" and "nonresonant." Within the "resonant" portion of the bandwidth, there are variable amounts of positive and negative detuned wavelengths that have no compensating phase added. The net effect of this is that the instantaneous phase of the nonresonant contribution is not necessarily zero or π. When this nonideality interacts with the transiently prepared state, there can be a large shift in instantaneous phase, as demonstrated

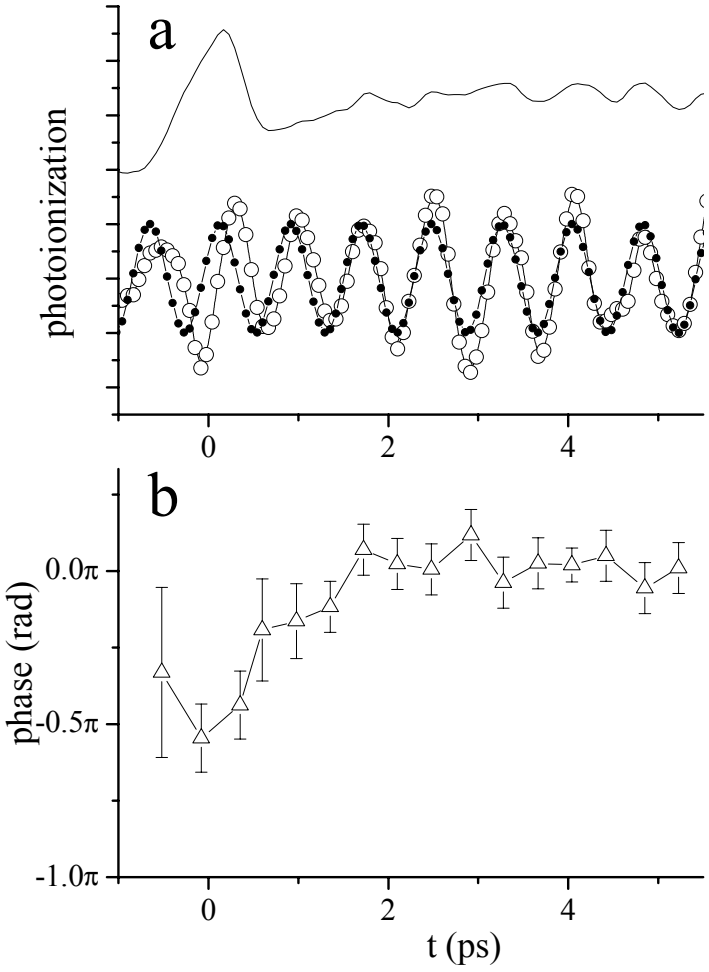

Figure 5.6: Sign inversion wave packet data without time-shifting the resonant contribution. All symbols are the same as Fig. 5.5. Notice the deviation in instantaneous phase away from 0 or π phase at short times. Also notice that the oscillation amplitude fails to approach zero between 0.0 and 2.0 ps.

in Fig. 5.6b. For this reason, the instantaneous phase is most predictable as the resonant and nonresonant contributions are separated in time.

Around t=0.0 ps, when the sign of the wave function for state |2> is inverted from that expected for the purely resonant phases, there is a certain degree of destructive interference in the contributions to the signal. By performing Wavelength Subtraction Spectroscopy (WSS) with the shaped pulses, a measure of the relative contributions of the various spectral contributions can be made. The traces shown in Fig. 5.7 illustrate destructive interference at play around t=0.0 ps for state |2>. The data were acquired by setting the pump-probe delay to a specific time delay, either 6.0 ps or 0.0 ps, with either unshaped or shaped pulses, respectively, and attenuating the light imaged onto one pixel at a time. The circles in Fig. 5.7 show the WSS spectrum for unshaped pulses at a pump-probe time delay of 6.0 ps. The trace shows a narrow bandwidth of contributing pixels, as one would expect since resonant frequencies determine the ultimate behavior of each state at long times in the weak field limit. The approximately two-pixel bandwidth is primarily an effect of spot size on the pulseshaper and not intrinsic transition bandwidth.

The squares show the spectral contributions to the signal at t=0.0 ps for both states |1> and |2> using the phase mask of Fig. 5.5a. The overall lineshape for state |1> only partially reflects the $1/\Delta$ behavior expected from Eq. (4.2), but it unambiguously shows an increase in the contributing bandwidth. The increase in effective bandwidth is attributed to the application of $\pm \pi/2$ phase to positively and negatively detuned frequencies. The spectral asymmetry is a result of a

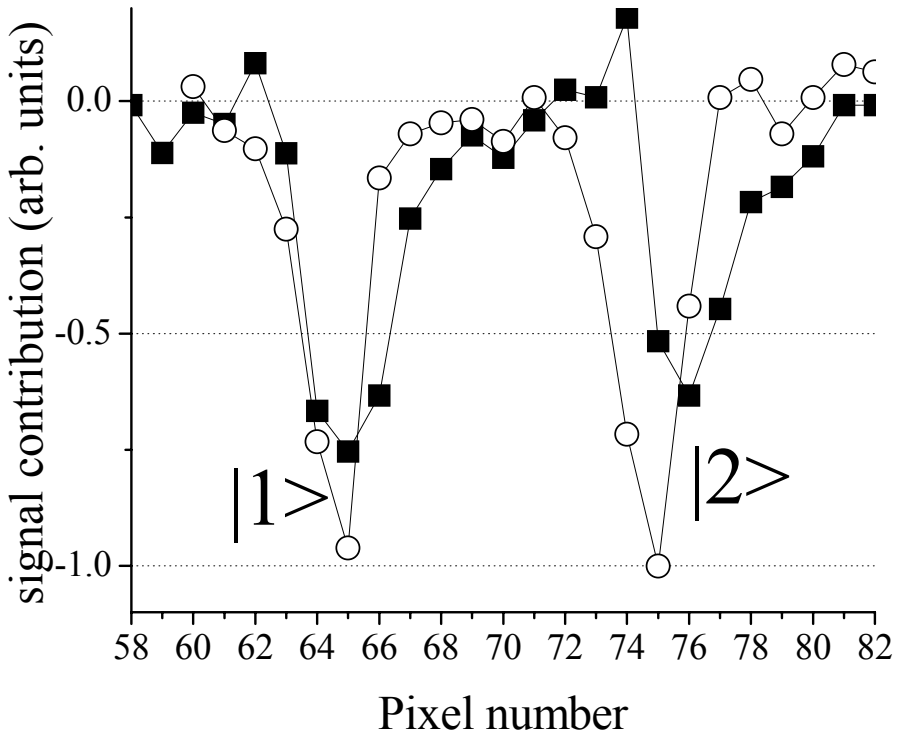

Figure 5.7: Wavelength Subtraction Spectroscopy traces for shaped and unshaped pulses. Here, the signal reflects the change in photoionization relative to background. The (○) is the WSS photoionization spectrum for an unshaped pulse at a fixed pump-probe delay of greater than 6.0 ps. The observed linewidths represent the resolution of the pulse shaper. The (■) show the WSS photoionization spectrum for the phase mask of Fig. 5.5a at a fixed pump-probe delay of 0.0 ps. The (■) spectrum around pixel 65 shows the effect of adding resonant and nonresonant contributions, and that around 75 represents subtracting resonant from nonresonant. Note the increased linewidth of the shaped pulses, and the increase in signal while blocking pixel 74.

combination of diffraction effects in the SLM and an asymmetric laser pulse spectrum. The WSS spectrum at t=0.0 ps for state |2> similarly shows that there is an increase in the contributing bandwidth relative to the long time delay. More interestingly, the results show that blocking the resonant wavelength actually increases the signal at t=0.0 ps, indicating a destructive interference. Even though the lineshape remains ambiguous, the increase in signal by blocking the resonant frequency on pixel 74 relative to the baseline is unambiguous. Since the wave packet signal at long times consists of recurrence oscillations with a phase offset of approximately zero, the resonant contribution to the signal can be concluded to have a positive sign relative to state |1>. This suggests that the total wave function coefficient for state |2> around t=0.0 is negative, in agreement with the wave packet phase data.

The results can be quantified in terms of the Z-gate representation as in Eq. (5.3), with the initial state taken to be the superposition at t=0.0 ps, and the final state taken to be the superposition at t=∞:

$$\begin{bmatrix} c_1(f) \\ c_2(f) \end{bmatrix} = \begin{bmatrix} \dfrac{res_1(\infty)}{res_1(0)+nonres_1(0)} & <.1\times res_1(\infty) \\ <.1\times res_1(\infty) & \dfrac{res_2(\infty)}{res_2(0)-nonres_2(0)} \end{bmatrix} \begin{bmatrix} c_1(i) \\ c_2(i) \end{bmatrix}, \qquad (5.4a)$$

where $res_i(t)$ and $nonres_i(t)$ are the resonant and nonresonant contributions to state i at time t. The off diagonal elements are a result of cross-talk between control channels which have previously been quantified with respect to the resonant contribution to the coefficients[33]. These off diagonal elements are essentially a measure of the degree to which the dynamics of each state can be independently

controlled. The diagonal elements of Eq. (5.4a) can be taken directly from the experimental data. The first diagonal element is determined to be 0.71, based upon the data from Fig. 5.2. The second diagonal element can be determined from the coherent oscillation amplitude shown in Fig. 5.5. Around t=0.0 ps, the peak-to-peak amplitude of the coherent oscillation is approximately 1.1 times greater than that at long time delays. Given that the coherent oscillation amplitude is proportional to $|c_1||c_2|$, and that $|c_1| \approx 1.4$, then $|c_2(t=0)| \approx 0.79|c_2(t=\infty)|$. This gives a value of -1.3 for the second diagonal element of the transient Z-gate matrix, to yield an experimental transformation of

$$\begin{bmatrix} c_1(f) \\ c_2(f) \end{bmatrix} = \begin{bmatrix} 0.7 \pm 0.2 & < .1 \\ < .1 & -1.3 \pm 0.2 \end{bmatrix} \begin{bmatrix} c_1(i) \\ c_2(i) \end{bmatrix}. \qquad (5.4b)$$

Ideally, as long as a phase of $\pm \pi/2$ is applied to the various nonresonant contributions to the wave packet, there will only be an addition or subtraction of those components relative to resonance, so the matrix components in this case can be assumed to have very little imaginary component. In other words, all contributions to the signal have been manipulated to have phases of either zero or π, which lie along the real axis of the complex plane. Experimentally, we observe the phase to be centered around zero or π, but limitations in the instantaneous phase detection introduce substantial error, see Fig. 5.5.

The instantaneous wavefunction phase could be better controlled and determined if the energy spacing between states were greater. The ability to control one state versus another increases as the state spacing increases as a result of the intrinsic $1/\Delta$ Rabi oscillation amplitude of Eq. (4.2)[33]. In the current

case, state |1> is used for a type of heterodyne detection of the phase of state |2>, where the first state is used to serve as a reference for the second. The interference between |1> and |2> permits effective viewing of the phase of state |2>, but only at the maxima and minima of the interference signal, giving a data point every $2/\omega_{12}$ ps, where the state spacing ω_{12} is given in units of THz. With the current state spacing of 42 cm^{-1}, one data point is retrieved every 0.3 ps, which is nearly half of the timescale over which the phase of state |2> changes from π to 0 radians. Increasing the state spacing, or increasing the coherent oscillation frequency, will provide a more accurate probe for how the phase change occurs. Additionally, a more rapid coherent oscillation will provide a more accurate amplitude of the coherent oscillation.

In this chapter, we outlined a system for temporarily switching the relative sign of one state in a superposition while keeping the sign of a second state constant. We showed that this can be done by simply using weak field, phase shaped ultrafast pulses. Additionally, we showed, using established spectral techniques, that the resonant and nonresonant contributions to a specific transition can be programmed to add together or to work in opposition on short timescales. This work expands upon established methods for controlling transient processes in molecular systems and presents a case where both the phase and amplitude of an excited state depend upon more than resonant frequencies.

Chapter 6

Strong Field Population Control: Theory and Experiment

6.1 Introduction

Ultrafast lasers have come to be used all over the world to study chemical and physical dynamics on the shortest of timescales. With the short timescales inherent to ultrafast lasers often comes high peak laser power. This can sometimes be problematic, since a system response to a strong field, such as that produced for a short time by an ultrafast laser, can cause interesting, or confounding, effects. Among these effects are multiphoton absorption[6, 20, 23], transition saturation effects[66], ultrashort X-ray generation[26, 67], or even nuclear fusion[68, 69]. Before the advent of ultrafast lasers, studies into strong field dynamics with nanosecond lasers have illuminated several of the same processes now also observed by ultrafast lasers[5], and there have even been examples of coherent control using cw lasers[36].

The study of wave packet dynamics and coherent control has a fairly broad base with respect to weak field processes where the outcomes are conveniently described using perturbation theory[9, 12, 17, 18, 70, 71]. There is a well established formalism for describing the response of molecules in the stronger field regime using the dressed state approach[36]. Somewhere in between these two regimes lies what would be considered stronger than perturbative, but which is not conveniently described using the dressed state approach. This chapter will investigate this middle ground, first theoretically and then experimentally.

One of the major goals of the analyses and experiments described here is to verify the complete depopulation of a single state in a molecule. This has been shown in many types of regimes, with and without pulse shaping[5, 36, 72]. Besides dynamic processes such as population inversion in lasers, stable population inversion can be seen in isolated systems with the application of a single pulse, producing Rabi oscillations in an excited state population[5]. Besides simple atomic systems, this effect has been observed or predicted in complex systems such as semiconductor quantum dots or molecules[52, 73]. With a little bit higher fields and even rudimentary pulse shaping, full population transfer to an excited state via Rapid Adiabatic Passage or to a third state with stimulated Raman via adiabatic passage (STIRAP) has been demonstrated on numerous systems[36, 66, 72, 74-79]. Often, in these cases, the systems are characterized by a single resonance or a series of resonances that are well separated in energy.

One way the theory and experiments in this chapter will expand upon this previous groundwork is that all transitions are embedded within the spectrum of a single broadband laser pulse, introducing a level of richness only recently addressed[23, 75, 80, 81]. Another is that these experiments are rotationally resolved, allowing a precise level of bookkeeping. Since the theory and experiments described here focus on second and third order coherences (*i. e.* involving two or three photons, respectively), some similar types of coherences can be created using various four wave mixing techniques[39, 82]. Two traits separate these experiments, however. First, these experiments will show evidence

for a *depopulation* of states, and second, these methods can be extended to study an arbitrary order of coherence without any intrinsic changes in methodology.

The successful development of this higher order pumping could be a means for easily selecting rotational quanta by coherent control. It is also a good model system for studying moderately dispersed processes such as population transfer among several vibrational states in a real molecule[24, 83, 84]. In fact, the system described here simply represents the dynamics at play for a single rotational state in a typical ground state ensemble—this study provides a basis for understanding the limitations of population transfer within an ensemble of rotational states. The techniques described in this chapter create what is essentially a rotational analog to vibrational ladder climbing[72, 78, 84-87]. In essence, the lessons learned here can eventually be used to generate highly excited rotational states, but with state specificity. One other important application of the lessons learned here is the potential for manipulating quantum information systems. In some material systems (such as trapped ions), series of unshaped population inverting pulses are used to switch qubit states, but an alternate method of population switching based upon ladder climbing with chirped pulses is presented here[63].

This chapter will only focus on the requirements that need to be met to measure state-resolved population transfer. We study an optically coupled system consisting of a progression of J values for a single vibrational level on each of two electronic states, so that the total wavefunction consists of a superposition of optically excited J states on the $A^1\Sigma_u^+$ and $E^1\Sigma_g^+$ electronic potential energy

curves. Experimentally, to measure populations, quantum beating between states will act as the primary sensor. One difficulty with excitation by higher fields is that the strong excitations on a theoretically isolated system may induce *too many* transitions. To see state resolved population transfer within the coupled system requires that the finite starting population not spread out among many different rotational states in the coupled system via optical pumping. This process of spreading out of wave function via optically induced $\Delta J=\pm 1$ transitions will be referred to as wavefunction dissipation. This wavefunction dissipation reduces the amplitude of a single observed quantum beat between two states since each individual state will have a reduced population, even if no population is lost out of the target coupled system. A second requirement for observation is that population not get optically excited out of the coupled system; this will be referred to as wavefunction depletion since the population in the coupled system decreases. In a molecule exposed to strong field laser pulses, processes such as multiphoton ionization and excitation to continuum states can play a significant role in population losses. Besides dissipation and depletion effects, certain physical phenomena such as the spatial beam profile and molecular alignment make observing oscillations in population as a function of electric field strength difficult[88-90], since these effects introduce inhomogeneities in the overall transition strength.

This chapter will begin with a theoretical treatment of the background issues required to consider strong field dynamics. The first section focuses on calculations related to the effect of field strength on the populations in the coupled

system. The calculations will start with a simple model, with the model complexity increasing step by step to account for experimental nonidealities. It will be shown that as the field strength increases, the degree of dissipation of the population over various J states increases to create a superposition of many J states at surprisingly low field strengths. Next, the influence of a spatially nonuniform electric field, as expected by a Gaussian beam, will be addressed, as well as the effect expected from using a specific probe beam profile. The reduction in the visibility of molecular Rabi oscillations because of alignment effects will also be discussed. Following this theoretical section, the field strength dependence of rotational quantum beats will be analyzed, and an example of wave packet dissipation will be shown. Depletion mechanisms are proposed, and a means to overcome this via spectral filtering is tested. The possibilities of controlling time and field strength dependent dynamics will be considered in both the theoretical and experimental sections with a simple case of implementing a Rapid Adiabatic Transfer Passage (RAP) using a chirped pulse[91], with the secondary goal of finding a population transfer scheme that shows robustness with respect to electric field strength.

6.2 Theory

This section will focus on the interactions between an electric field and two optically coupled progressions of J states. The goal of this theoretical section is to define and then control wavefunction dissipation. First, the theoretical formalism will be established, followed by an analysis of the response to a strong

ultrafast laser pulse of a system with numerous (~15) transitions embedded within the laser bandwidth. Here, the term strong refers to a breakdown of the normal weak field assumption that the population in the launch state remains near unity. Instead, the observed population of the launch state goes through a series of decaying oscillations as the total wavefunction dissipates to larger and larger numbers of J states on the A and E potentials. This will be followed by an analysis of expected trends in electric field strength dependence assuming selected probe pulse characteristics and alignment issues.

6.2.1 Spatially uniform fields

The dynamics used to model the system under the assumption of a spatially uniform laser intensity are summarized below. First, it is assumed that a pure launch state is used (v_A,J_A=11,28), as in all previous chapters. Disregarding depletion of the population out of the $A^1\Sigma_u^+(v_A=11)$ and $E^1\Sigma_g^+(v_E=9)$ vibronic states, the time dependent wave function has the following form:

$$\Psi(t) = \sum_{j=-J_0}^{\infty} c_j(t)\left|v_j J_j\right\rangle \Big/ \sum_{j=-J_0}^{\infty}\left|c_j(t)\right|^2 . \qquad (6.1a)$$

where each wavefunction $\left|v_j J_j\right\rangle$ represents one of the rovibrational wavefunctions shown in Fig. 6.1, and $c_j(t)$ represents the amplitude of each wavefunction. It is instructive to note that all odd J states are on the E electronic potential, and all even J states are on the A electronic potential. All J quantum numbers are offset relative to the launch state of J=28, so the summations go from -28 to ∞. To reduce calculation times, the summations are over J=22-34, and P

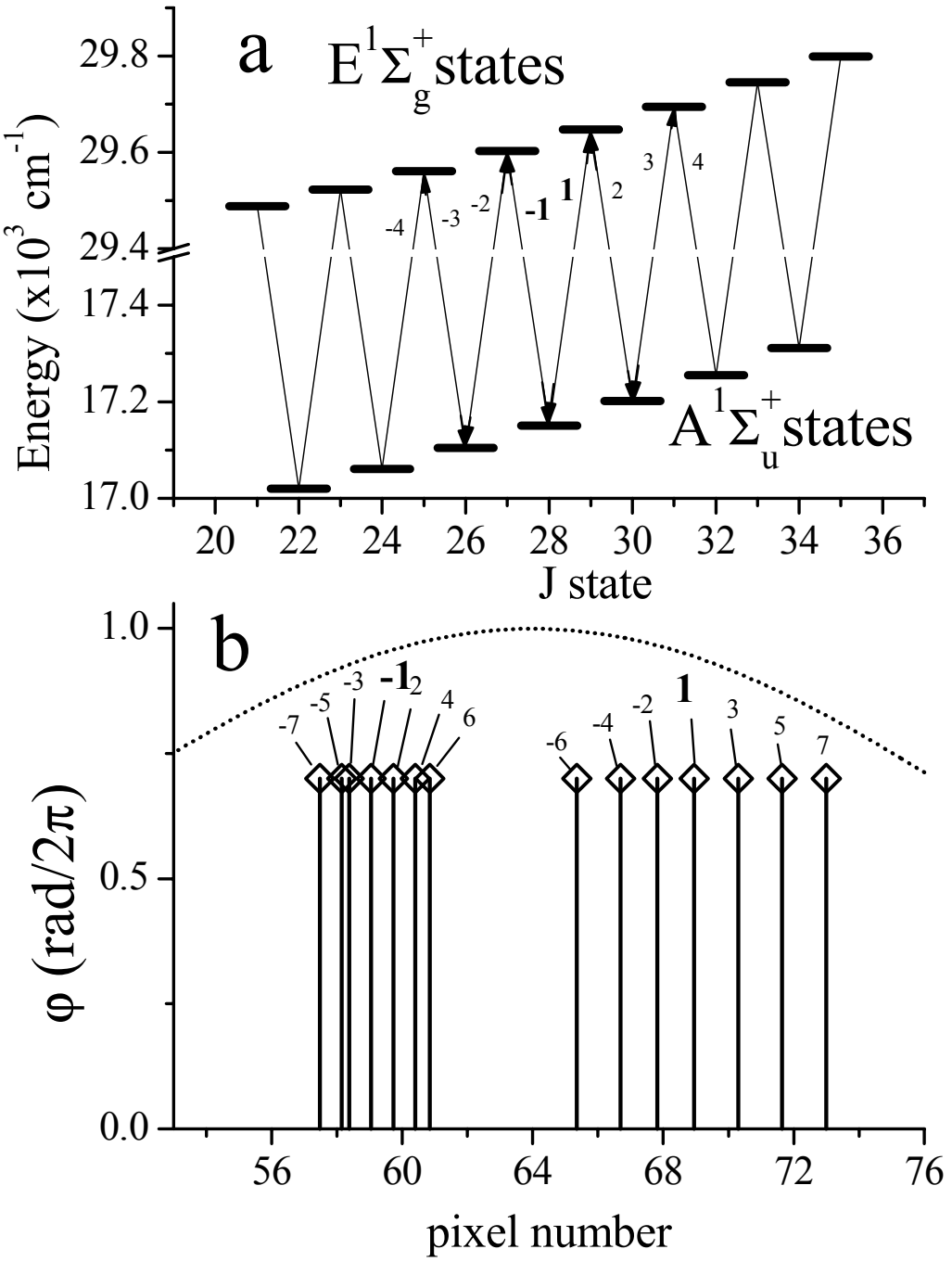

Figure 6.1: Summary of resonant frequency positions. Panel a: Energy levels considered in this theoretical treatment. Resonant transitions are notated by their greatest proximity from the launch state of J=28. For example, a transition between J=31 & 32 is noted 4 (32-28=4) regardless of whether it is a "pump" or "dump" process. Panel b: Resonance locations as imaged onto the SLM. The dotted line represents the Gaussian spectral envelope.

and R branch pump (and dump) transitions are notated relative to their greatest proximity to the J=28 state in J space. In all of the calculations presented here, the wavefunction fails to dissipate to the J limit, justifying the J space truncation. Each of the coefficients $c_j(t)$ are calculated as

$$c_j(t) \propto i \int_{-\infty}^{\infty} dt \varepsilon(t) \sum_k c_k(t) \sigma_{jk} e^{i\omega_{jk}t} \tag{6.1b}$$

where the summation is over all states k, $\varepsilon(t)$ is the electric field, σ_{jk} is the transition moment, and ω_{jk} is the resonant frequency between any two of the coupled states. With a typical minimum pulse length of ~150 fs compared to the optical cycle of ~2.87 fs, the slowly varying envelope approximation is applied, giving a temporally varying electric field as

$$\varepsilon(t) \approx N_{FS} |E(t)| \cos[\omega(t)t + \phi(t)]. \tag{6.1c}$$

where $|E(t)|$ is the pulse envelope, and N_{FS} is a field strength normalization parameter, to be described below. The time dependence of the frequency and the phase has been made explicit to account for pulse shaping situations. Since only P and R branch transitions are strongly allowed between the A and E states, the oscillator strength varies only slightly with J (<5% for m_J=0)[92], so if we assume that all states are in m_J=0, $\sigma_{jk} = \delta(j, k=j\pm1)$. Following the first few calculations, the m_J dependence of the transition dipole will be made explicit. With the J_A=28 launch state, this selection rule establishes that all even J states are on the A state, and all odd J are on the E state. The exploitation of the $\Delta J=\pm1$ selection rule simplifies the above scheme to 14 coupled differential equations. For a two level system, this dynamical model reduces to the classic Rabi formula:

$$|c_e(t)|^2 = 1 - |c_g(t)|^2 = \int d\Delta \left[1 - \left(\sigma_{eg}\varepsilon(\Delta)/\Omega_{eg}\right)^2 \sin^2\left(\Omega_{eg}t\right)\right] \qquad (6.2a)$$

$$\Omega_{eg} = \sqrt{\Delta^2 + \left[\sigma_{eg}\varepsilon(\Delta)\right]^2}\,, \qquad (6.2b)$$

where $\Delta=\omega_{eg}-\omega$ is the detuning away from resonance, and σ_{eg} is the transition moment from the ground to excited state[93].

In the dynamics modeled here, we express the electric field as outlined in the literature[34], and summarized in Eq. (3.1a), with a central wavelength of 801.7 nm and a Gaussian bandwidth of 9 nm, imaged onto the SLM over 35 pixels with a single frequency spot size of 1.7 pixels, with all extents expressed as FWHM (see Fig. 6.1). In many of the calculations and experiments in this chapter, the system dynamics as a function of the normalized field strength, N_{FS} from Eq. (6.1c), are explored. The excitation pulses are normalized so that for a two level system [i.e. $\sigma_{28,29}=1$, all other $\sigma_{jk}=0$, see Eq. (6.2)] with an unshaped pulse, the time integrated product of $\varepsilon(t)\sigma_{28,29}t=\pi$ holds for $N_{FS}=1$. The unit N_{FS} is used instead of *pulse area* to avoid confusion with the beam size (see [5]). Given that several of the calculations and experiments involve phase and amplitude shaped pulses, N_{FS} for a shaped pulse is expressed in terms of the unshaped *parent* pulse. This allows the comparison of shaped and unshaped pulses.

In contrast to the two state calculation, when all of the strongly allowed transition moments ($\sigma_{J,J\pm1}$) are set to 1, the wavefunction will dissipate to an increasing number of rotational states as N_{FS} increases. Figure 6.2 shows the results of this dynamical model as applied to this system for an unshaped input pulse. In this calculation, probe beam and alignment effects have not yet been

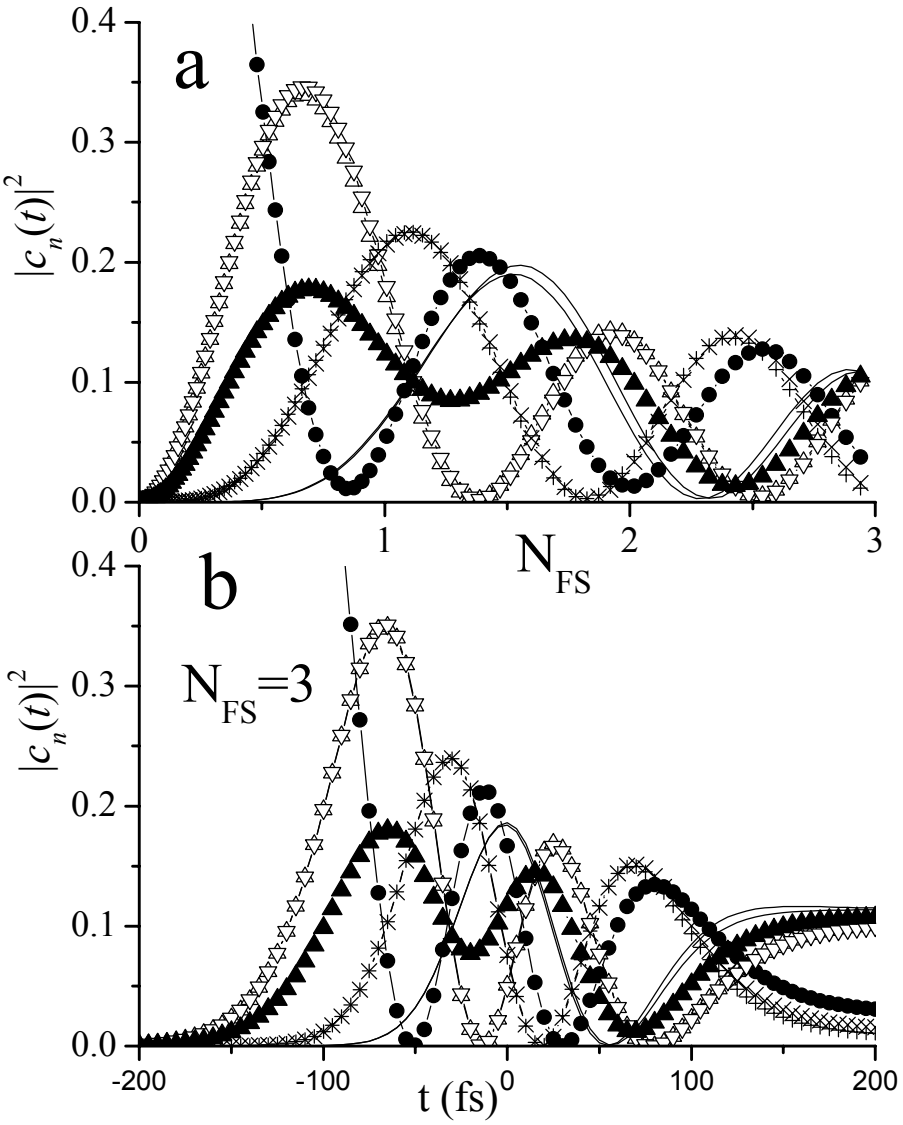

Figure 6.2: Dissipation of wavefunction over various J states for m_J=0. An unshaped spectrally Gaussian pulse is used, and the populations are normalized. In both panels, the launch state (●), ΔJ=±1 (△,▽), ΔJ=±2 (+,×), and ΔJ=±3 (solid lines) are included, along with the average of the shown E state populations (▲). Panel a: The t=∞ population distribution as a function of field strength normalization parameter N_{FS}. Panel b: The time evolution of the J-state distribution as a function of time for N_{FS}=3. Notice in both panels how states at +J and –J are approximately the same.

implemented. The population transfer in this unshaped case shows similar dynamics as a function of both time and N_{FS}, demonstrating oscillating populations. First, the launch and $\Delta J = \pm 1$ states show an immediate onset of oscillatory behavior, with a phase shift between the two, and the oscillations for the $\Delta J = \pm 2$ and ± 3 states show a delayed onset of oscillations. This approximately means that starting with $\Delta J = 0$, population goes to $\Delta J = \pm 1$, then to $\Delta J = 0, \pm 2$, then to $\Delta J = \pm 1, \pm 3$, etc., all via $\Delta J = \pm 1$ transitions. The J states more remote from the launch state (not shown) show a similar delayed onset of population followed by the expected oscillatory behavior. Since all even states are on the A state, and odd states on E, this will produce oscillations in the population between electronic states, with almost complete inversion at high field strengths as all of the even (and odd, respectively) oscillations come into phase at the same field strengths. One interesting observation here is that the oscillation frequency for electronic inversion is twice that for an isolated two state system. Of course, this is easily explainable because in the full model, each state gets depopulated via two channels, namely the P and R branch transitions.

The observed signal is slightly more complicated than a simple observation of populations, since the observable is actually a quantum interference, or coherence, between states that share a common final state[33, 48]. In the experimental system, photoionization occurs via a weak excitation to a narrow band of incoherently autoionizing Rydberg levels, converging on the v=0 vibrational state of the ion[47]. Although multiphoton ionization out of the E state has been observed, the primary coherence producing mechanism involves a

single photon. To observe a wave packet, this means that the observed wave packets will have a $\Delta J=2$ component (i.e. $J_E=27$ interfering with $J_E=29$), as these states share the common final state of the average J between the interfering state via the $\Delta J=\pm 1$ single photon ionizing probe, which is accessible by half of the population from each of the interfering states. Similar arguments suggest that the primary wave packets seen on the A state will have a $\Delta J=2$, even though they are photoionized with at least two photons of the probe pulse which has a selection rule of $\Delta J=0, \pm 2$[6, 94]. As applied to Fig. 6.2, these beats will follow pairs of populations that satisfy the ΔJ interference requirements for a common final state. In an analysis of beat amplitudes as a function of pulse amplitude, the oscillatory behavior will be seen, with beats on the A and E states having a phase shift in their oscillations, like individual populations on the A and E potentials. At lower pulse amplitudes, this behavior will be more complicated, but the qualitative trend remains.

As will be discussed later, the ability to observe wave packet dynamics in the high field requires little dissipation of population within the coupled system of interest. One potential method for minimizing this dissipation is to attenuate wavelengths of light that do not participate in the dynamics that one wants to investigate. For this reason, it is useful to quantify the importance of various spectral contributions to the signal. To perform this, WSS spectra were calculated for a variety of pulse amplitudes in a two level system, shown in Fig. 6.3. The bottom of the figure represents the excited state population as it would appear in our current setup with the sequential attenuation of light on single pixels. As

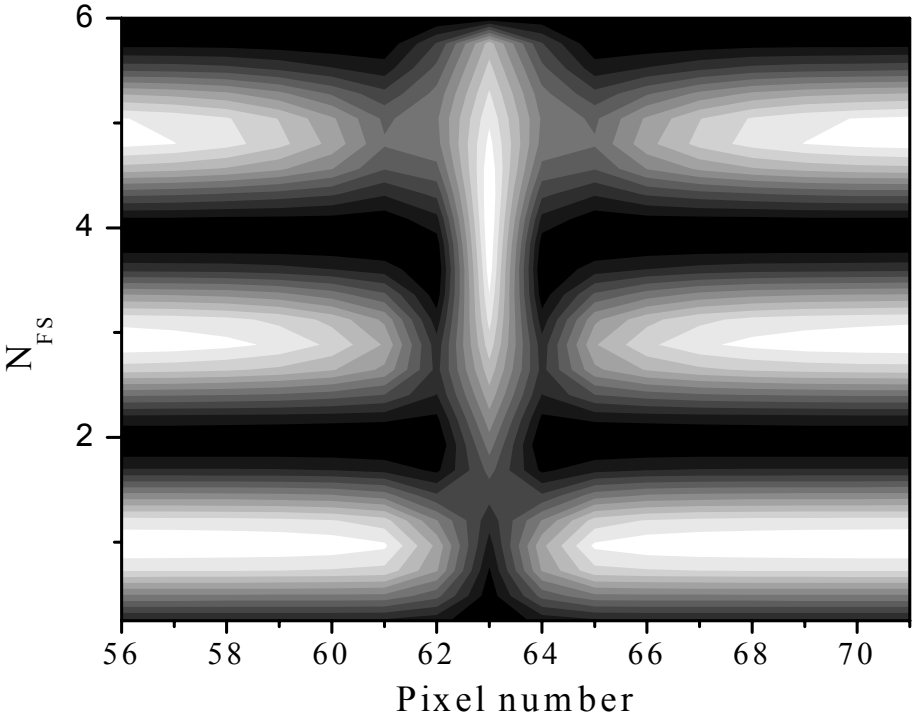

Figure 6.3: Calculated WSS spectrum as a function of normalized field strength for a two level system. Here, N_{FS} is equivalent to the total pulse area multiplied by π. The figure shows the WSS spectrum based on the experimental traits of the pulse shaping setup, with a single resonance centered on pixel 63. White indicates excited state population. The population inversion seen while blocking pixel 63 indicates a nonresonant Rabi oscillation. Note how, at the lowest powers, a notch in the excited state population appears when blocking the pixel 63.

highly nonresonant frequencies are attenuated, we see no significant change in the excited state population: Rabi oscillations in the excited state population are observed. As the resonant frequency is blocked (pixel 63), the population inversion occurs at N_{FS}= 4 instead of at N_{FS}=1, indicating that the Rabi oscillations have a frequency of approximately 8 instead of 2. This is primarily a result of some resonant frequencies being imaged onto pixels adjacent to that where the spectrum is centered. To try to get a more refined sense of what is happening near resonance, sub-pixel resolution on the SLM was assumed. This calculation confirms that at relatively low powers, the population transfer dynamics can be considered almost as resonant processes. Unless the electric field amplitude exceeds 4π, the effective bandwidth for each transition remains below 4 pixels. This suggests the possibility of attenuating frequencies more than 4 pixels from any resonance without concern for significantly changing the energy dependent dynamics. Of course, as should be expected from previous chapters and other published work[6, 8], the highly nonresonant wavelengths become more important if the pulses are phase shaped, as will be addressed in future work not included here.

6.2.2 Alignment effects

An additional mechanism for limiting the visibility of Rabi-type oscillations is attributed to alignment effects, or m_J effects. In all of the calculations in this and the previous section, it was assumed that m_J=0, which is not necessarily the case. The presence of multiple m_J states in the initial

wavefunction will result in two different types of effects: dispersion of Rabi oscillation frequencies and a tendency to drive population toward high J. The dispersion of Rabi oscillation frequencies stems from the polarization of the excitation laser. Defining the laboratory coordinate relative to the excitation laser polarization, the transition strength for a parallel transition, such as between the A and E states, decreases as $|m_J|$ increases[92]. In order to study this, the above model was modified to fully account for the presence of multiple m_J states:

$$\Psi(t) = \sum_{j=-J_0}^{\infty} \sum_{m_J=-j}^{j} c_j(t) \left| v_j J_j m_J \right\rangle \Big/ \sum_{j=-J_0}^{\infty} \left| c_j(t) \right|^2 \qquad (6.3)$$

where all terms are the same as Eq. (6.1) except the m_J quantum numbers are explicit. The coupled equation scheme of Eq. (6.1c) does not change except that σ_{jk} is futher modified by Clebsch-Gordon coefficients coupling the various rotational states. It should be noted that intrinsic to the transition strengths is the requirement that $|m_J| \leq J$, so a transition from $J,m_J=29,29$ to $J,m_J=28,29$ has a transition strength of zero, since the 28,29 state does not exist. Since the time or N_{FS} dependence of population evolution show similar dynamics for an unshaped Gaussian pulse (see Fig. 6.2), the time evolution of the population dynamics will be shown here and inferred to reflect the N_{FS} evolution.

If multiple m_J states are populated, there will be multiple m_J dependent Rabi oscillation frequencies, as seen in Fig. 6.4. Shown is the evolution of the launch state population for three selected m_J from a uniform distribution of m_J states under an excitation by a field with N_{FS} equal to 2 with the transition dipole moment and electric field polarizations parallel to $m_J=0$. At short times, all m_J

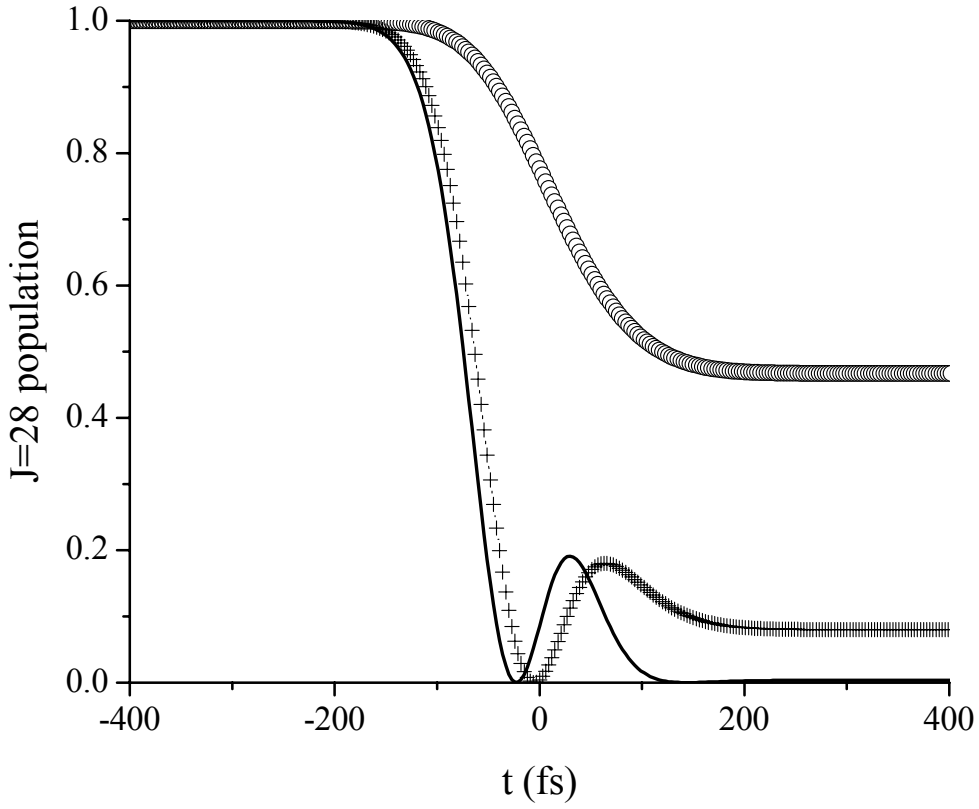

Figure 6.4: Evolution of J=28 population for various m_J states under excitation with a laser field with N_{FS}=2. m_J quantum numbers of 0, 14, and 28 are represented as the solid line, (+) and (○), respectively.

states are equally populated, but at longer times the m_J distribution clearly deviates from uniform. To describe the nature of the evolution of the m_J distribution, a measure of alignment (*Al*) for a specific J follows:

$$Al_J(t) = \sum_{m_J} m_J \left| c_{J,m_J}(t) \right|^2 \Big/ J \sum_{m_J} \left| c_{J,m_J}(t) \right|^2 \qquad (6.4)$$

where the $c_{J,mJ}(t)$ coefficients describe J, m_J states, and the *J* in the denominator is included since the approximate angle of a single m_J state depends on *J*. Assuming that the total observed population is an incoherent sum of m_J states, the presence of this distribution will reduce the depth of modulation of any observed Rabi-type oscillations and cause the molecules to come into and out of alignment as a function of time or N_{FS}[89, 90].

Figure 6.5 summarizes the population evolution as a function of time for J=28 and N_{FS}=2. In Fig. 6.5a, the limiting case of a uniform m_J distribution case shows a significant decrease (~20%) in the observed depth of modulation of the oscillations in population. In experiment, the cw and probe lasers are most sensitive to small $|m_J|$ for the same reasons cited above, in effect sampling small $|m_J|$, so the calculation was also performed assuming an additional alignment inducing laser. The time dynamics of the J=28 population initially prepared by a weak field cw launch laser shows a depth of modulation of ~95% of the m_J=0 case, also shown in Fig. 6.5a. A second weighting laser (such as an ultrafast probe) will further sample small $|m_J|$, but subsequent calculations take a conservative approach and assume a single m_J sampling laser. Pulse shaping strategies can be put into effect to account for this effective spread in m_J dependent transition strengths, and they will be analyzed in section 6.3.2.

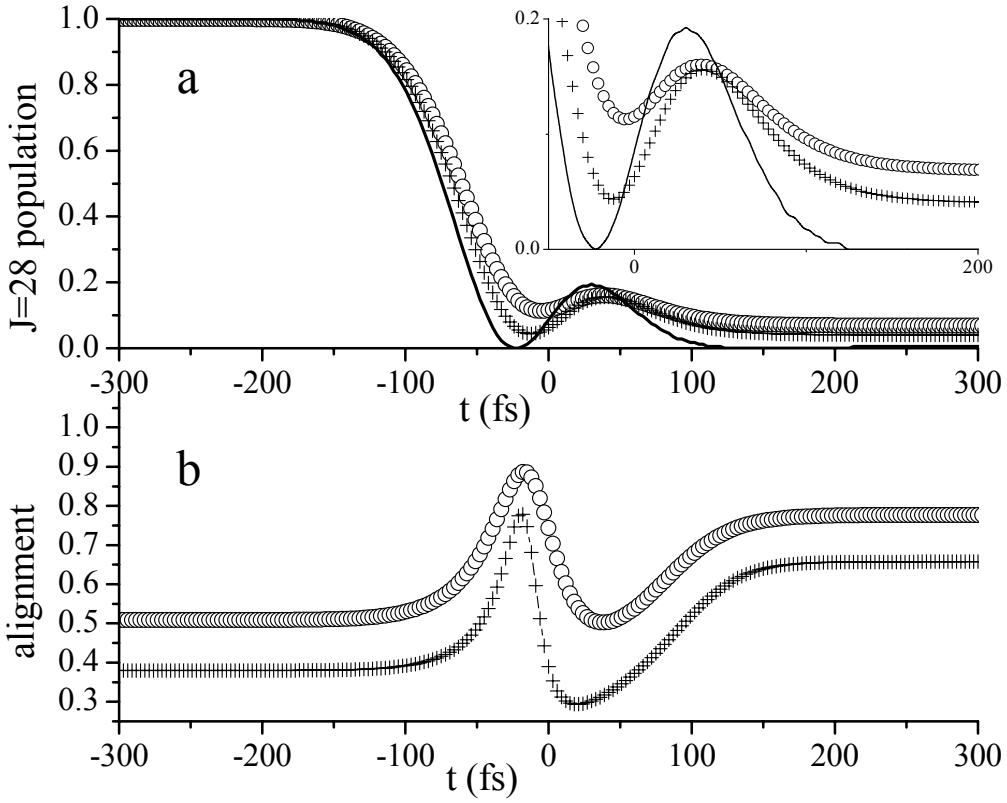

Figure 6.5: Effects of alignment on total population in J=28 state. Panel a: total J=28 population as a function of time for N_{FS}=2. Circles represent the population with a uniform distribution of m_J starting states. Plusses represent the J=28 population assuming the presence of a mechanism that samples the m_J space—such as a single weak probe pulse. The solid line shows the evolution of the m_J=0 state. All populations have been normalized to a starting population of 1. The inset expands the peak around t=50 fs. Panel b: alignment as a function of time for J=28 state. Circles and plusses indicate the same conditions as in panel a. In the sampled case, the alignment more closely approaches zero, which is explained by preferentially sampling low $|m_J|$ states. The peaks around -20 fs represent times when population has been transferred out of the low $|m_J|$ states, leaving primarily high $|m_J|$.

In accounting for the total m_J distribution, an interesting alignment trait comes out of the calculation. Consider the J=28 launch state, for example. Early in the evolution of its population, the first $|m_J|$ states to be taken out of its total population will be parallel small, leaving large $|m_J|$, as is shown in Fig. 6.5b. For N_{FS}=2, the alignment, as defined by Eq. (6.4), goes through a maximum at t=-20 fs, in effect creating an incoherent rotation, or wobble, as the incoherent sum of m_J states oscillates between a parallel and perpendicular net alignment. Even in the presence of a low $|m_J|$ weighting laser that preferentially aligns the population parallel to the laser polarization, this wobble still exists at short times.

Alignment effects can also influence the preferred direction (+J instead of –J) of a transition with linear laser polarization, since we expect a selection rule of $\Delta m_J=0$. Given this selection rule and the basic degeneracy limitation that $|m_J|\leq J$, choosing a launch state of J=28 imposes the condition that $|m_J|\leq 28$ for $J\geq 28$ and $|m_J|\leq J$ for $J<28$, referred to here as population "degeneracy filtering". Figure 6.6 shows that high J states are favored in this rotational system due to these degeneracy effects using spatially uniform pulses. The time dynamics for the $\Delta J=\pm 3$ (*i.e.* J=25&31) states under excitation with an N_{FS}=2 pulse is shown in Fig. 6.6a, with the J=25:J=31 population ratio equaling 0.81. This ratio is very close to the ratio of the J state degeneracies between the states, but it should be noted that the population ratio does not rigorously have to match the ratio of J state degeneracies. For example, after excitation using N_{FS}=2 the $+\Delta J$:$-\Delta J$ population ratios for the $\Delta J= \pm 1, \pm 2, \pm 3, \pm 4, \pm 5, \pm 7$ states are 0.97, 0.95, 0.81, 0.90, 0.98,

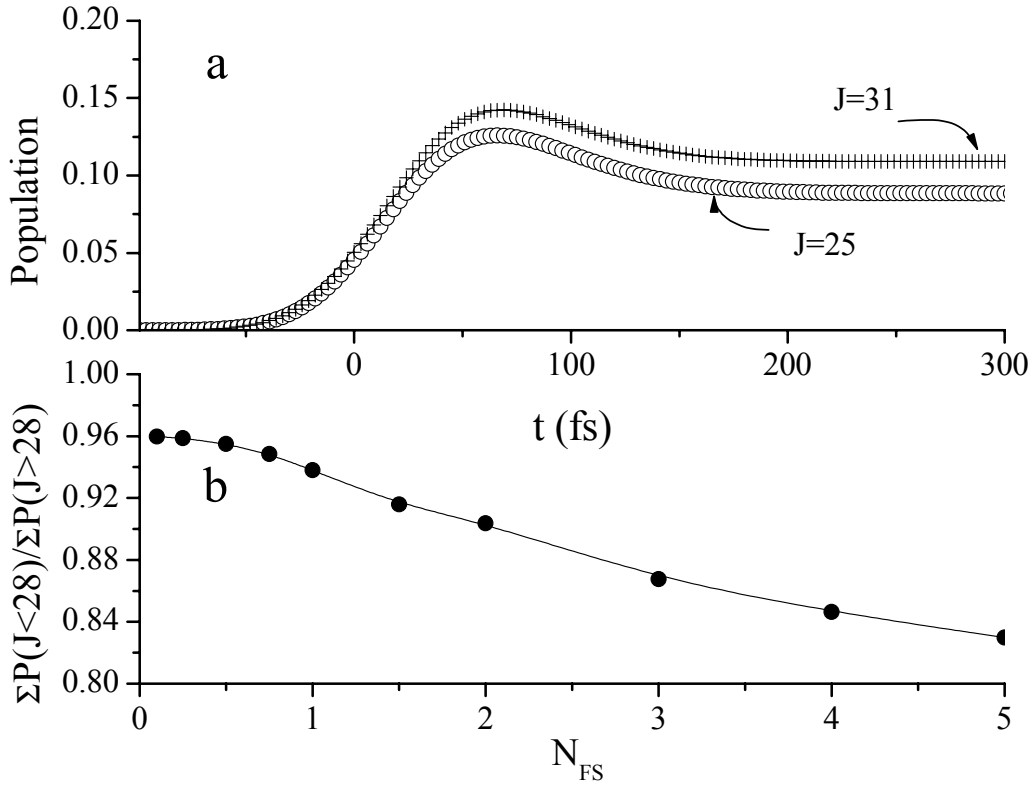

Figure 6.6: Degeneracy dependent selectivity for high J vs low J. Panel a: population evolution for J=25 (○) and J=31 (+) for a pulse amplitude with N_{FS}=2 and an initially uniform m_J. The final J=25:J=31 population ratio is about 0.8. Panel b: Ratio of the sum of all J state populations below the launch state versus those above the launch state as a function of pulse amplitude N_{FS}.

0.98, and 0.94, respectively. This deviation is primarily a result of the fact that this degeneracy filtering is occurring where $|m_J|$ is large, and hence has a relatively weak transition probability. As the optical transitions become stronger, the population ratio for those states with low J versus high J will decrease [$\Sigma(J<28):\Sigma(J>28)$], as shown in Fig. 6.6b. Plotted is the ratio of the sums of populations for J<28 versus J>28, where it is shown that increasing N_{FS} increases the selectivity to higher J. In the figure, the low to high J ratio for low N_{FS} approaches .965 and reaches 0.84 at N_{FS}=5. At lower N_{FS}, the ratio is fairly insensitive to changes in the field amplitude since the primary states to be involved in a transition will have small $|m_J|$. The ratio of low to high J approaches the average ratio of degeneracies between the low and high J states, 0.75, only at the highest powers. This can only occur in a system that can be saturated, such as this case of a 15 J state model, illustrating a limitation of this model at the highest powers. In the experimental system, since J can approach infinity, saturation will not occur, so the ratio of populations will remain above the ratio of J state degeneracy. Additionally, our experimental laser fields only approach the equivalent of N_{FS}=~2, reducing the importance of this effect.

6.2.3 Spatially Inhomogenous Fields

In the above analysis, a single value of N_{FS} represents the strength of the electric field. In experimental situations, a single value often fails to describe the electric field[88]. In a typical case, the laser beam used to excite any transition is not uniform, rather spatially Gaussian. In our gas phase sample, the nonuniform

beam excites molecules in different regions of space. The molecules respond as if the excitation comes from a number of independent lasers with varying powers since the molecules are basically uncorrelated with respect to our method of signal detection. For this reason, the spatial extent of our laser beam will be made explicit in further calculations. Since our signal is a result of a pump-probe process, the excitation produced by the pump laser gets spatially sampled by the non-uniform probe pulse, so that pulse will be included in the calculations.

The spatial cross section of a Gaussian beam is described by the following:

$$|\varepsilon(R)| = N_{FS}|\varepsilon_0|\exp\left[-(2/\ln 2)(R-R_0)^2/FWHM^2\right] \qquad (6.5)$$

where $N_{FS}\,|\varepsilon_0|$ is the normalized electric field amplitude at the center of the beam, the spatial extent R is relative to the center of the beam, and FWHM is the full width at half maximum of the beam radius. This effective field amplitude then gets plugged into Eq. (6.1c) and Eq. (6.2) giving a spatially dependent Rabi frequency. Since the signal has spatial dependence, each of these frequencies gets weighted by a radial factor R. Now the time dependent wave function of Eq. (6.1a) contains an R dependence, and the overall signal is related to it:

$$S(t) \propto \int_R R dR \left|\Pr(R,t)\Psi(R,t)\right|^2 \qquad (6.6a)$$

$$\Psi(R,t) = \sum_{j=-J_0}^{\infty} c_j(R,t)\left|v_j J_j\right\rangle \Big/ \sum_{j=-J_0}^{\infty}\left|c_j(R,t)\right|^2, \qquad (6.6b)$$

Above, Pr(R t) simply refers to a spatial sampling condition fulfilled by the spatially inhomogenous probe pulse, and all summations are relative the launch state J_0=28. In this particular subsection, alignment effects will be ignored to

more accurately illustrate spatially specific effects. Additionally, the detected signal is an incoherent integral over R since the ions are detected via an incoherent autoionization of weakly excited Rydberg states[47], so there will be no evidence for spatial coherences in R when taking the modulus squared of the wave function. The R coordinate will only act as a weighting factor.

In experiment, the probe pulse is approximately spatially Gaussian of the same size as the pump, but this assumption carries with it a few caveats. The calculated dependence of the Rabi oscillation visibility versus the size of the beam in the probe step for a two level system is given in Fig. 6.7. In these calculations, the diameter of the probe pulse changes relative to the pump pulse, but the integrated flux remains constant, as if the probe is focused relative to the pump. As the probe size decreases, the observed excited state population behavior evolves from a monotonically increasing type dynamic to a more oscillatory type dynamic. This simply results from sampling a smaller range of field amplitudes of the pump pulse as the probe size decreases. The limit of excitation with a uniform field would look similar to the smallest probe size, except that probe size would not affect depth of modulation of the Rabi oscillations. On the other hand, using a detection scheme that does not sample a small volume in the pump beam would resemble the large probe limit, with virtually no depth of modulation of the N_{FS} dependent Rabi oscillations. An example of such a detection scheme would be in an experiment studying laser induced fluorescence with a single photon excitation.

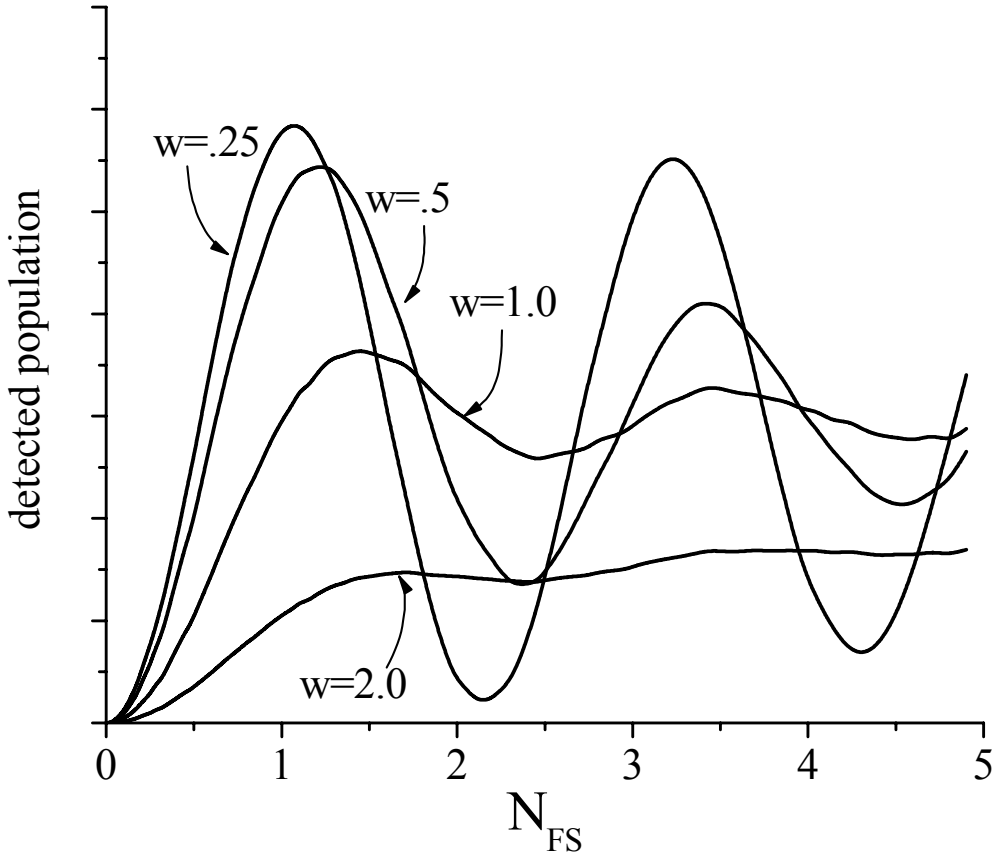

Figure 6.7: Rabi oscillation visibility for various probe sizes. The probe is assumed in all cases to have a constant fluescence, but changing relative focusing conditions. The detected signal is further assumed to be linear in probe power. The full width at half maximum of the probe is given by w in units of the pump width.

To demonstrate the possibilities for using pulse shapes to control the dynamics of population transfer in this particular system, we examine chirped pulse excitation as a function of N_{FS}. The form of the basic wavefunction now contains aspects of Eq. (6.6b) and Eq. (6.3):

$$\Psi(R,t) = \sum_{j=-J_0}^{\infty} \sum_{m_J=-j}^{j} c_j(R,t) \left| v_j J_j m_J \right\rangle \Big/ \sum_{j=-J_0}^{\infty} \left| c_j(R,t) \right|^2 , \qquad (6.7)$$

where both alignment and beam inhomogeneity effects have been taken into account. In these calculations, an alignment inducing (or m_J sampling) cw laser is assumed. For a probe, a beam with the same spatial extent as the pump is assumed, and a single photon is used to photoionize all E (odd J) states, and two photons are used to photoionize all A (even J) states. In experiment, the A state is photoionized via a two-photon process at approximately 75% of the efficiency of the E state since its signal reflects a smaller sampling region of the excitation region [see Fig. 6.10]. To account for this, the spatially integrated observed population for the A state is set to be 70% of an equally populated E state.

Figure 6.8 shows several states' population dependence on N_{FS} using an excitation pulse with a chirp of 4500 fs^2. This chirp was chosen for its energetic robustness relative to other chirps not shown here. This figure deviates substantially from the example of excitation with transform limited pulses. First, recurrences in observed populations no longer exist except at fairly high N_{FS}; instead the population transfers to the $\Delta J=2$ state for a large variety of N_{FS}[86]. In fact, at specific N_{FS} values, there is essentially full population transfer between the launch and final states, but it is not completely visible in the presence of a nonuniform excitation pulse. The populations of the $\Delta J= \pm 1$ states show signature

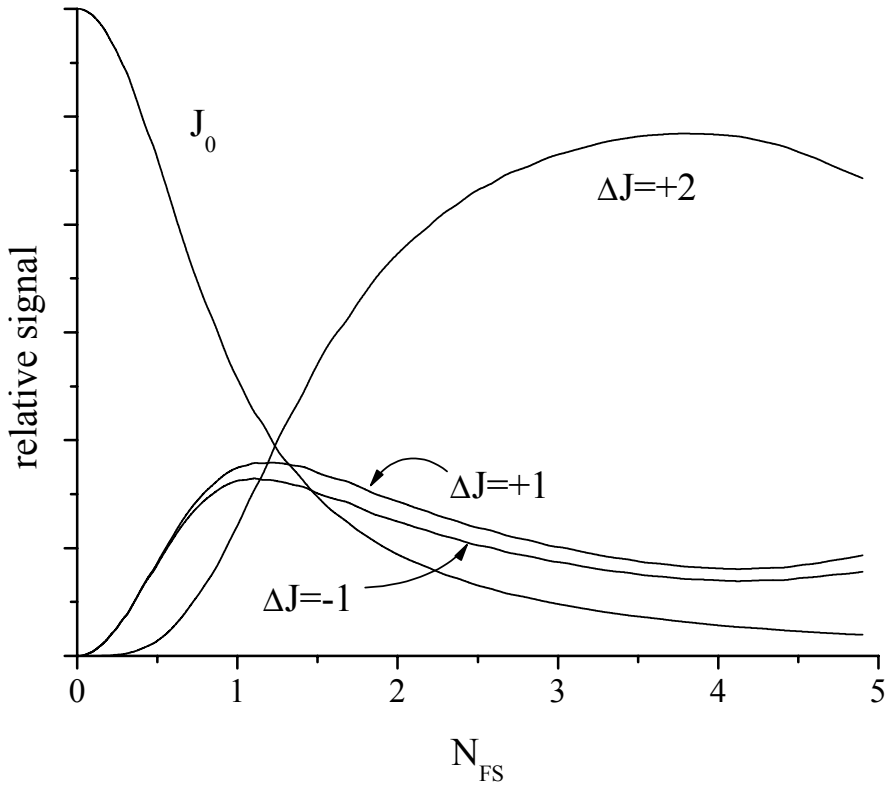

Figure 6.8: Calculated populations as a function of normalized field strength for positively chirped pulse. J_0 indicates the launch state of J=28. Note that all even J states lie on the A electronic state and odd lie on the E electronic state. The chirp is set to 4500 fs^s. The ΔJ=-2 state is essentially zero at all N_{FS}. The E (odd) and A (even) states are probed by a beam with the same diameter of pump with 1 and 2 photons, respectively.

dynamics of going through a maximum at fairly low N_{FS} then slowly decaying to near zero, with a small recurrence at very high N_{FS}, and the ΔJ=-2 state gets very little population transferred to it at all times shown here. Again, the only reason the ΔJ=±1 populations do not go to zero is that the electric field is not uniform. In the case of a uniform electric field, the amplitude of all states except ΔJ=2 will go to zero over a wide range of energies. The mechanism behind this energetically robust process is that there are two sequential Rapid Adiabatic Passage events that are separated in time because of the overall chirp of the excitation pulse[52, 66, 71, 72, 78, 86]. This effect has been shown in theory and in atomic excitation where only a single pathway is possible[95], and theoretically with respect to vibrational excitation[81]. Inverting the sign of the chirp will reverse the time ordering of the wavelengths in the pulse, subsequently inverting the Rapid Adiabatic Passage events, giving final state selectivity (not shown).

6.3 Experimental Observations

The goal of this section is the show dissipation of the wave function from a single rotational pair into a much more complex set of states, and then to control the dissipation. Next, it is shown that different quantum beats have different electric field amplitude dependence, reflecting the order of the beats. Finally, a sequential Rapid Adiabatic Transfer dynamical scheme is implemented. Selectivity between final state populations is shown to depend on the sign of the chirp.

To accomplish the experiments described here, the only change to the experimental setup relative to experiments described in previous chapters is that the pump and probe beams pass through a 25 cm focal length lens just at their input to the heat pipe. This gives a spot size of approximately 100μm FWHM. For the pump beam, the average power in the heat pipe is approximately 200 mW. Given a pulse duration of approximately 200 fs, and with a repetition rate of 200 kHz, the peak power density is approximately ~10^{11} W/cm^2, several orders of magnitude greater than the weak field experiments described in earlier chapters. As it has been shown in the previous calculations, many of the effects that we expect to observe depend primarily on resonant wavelengths. This allows us to attenuate much of the nonresonant pump light, resulting in a peak power closer to $1x10^{10}$ W/cm^2. Still, this intensity will adequately induce Rabi oscillations as described above.

As the power of the pump pulse increases, higher order states become populated at the expense of the population in the launch state. One way of observing this is to identify quantum beats at new frequencies, as summarized in Table 6.1, and shown in Fig. 6.9. In Fig. 6.9, the quantum beat spectrum for two different pump energies using the J_A=28 launch state clearly shows the population of a new set of states when the peak pump power increases. The high field trace shows not only the quantum beat between the J_E=27&29 states, but also a set of beats between J_A=28&30 and J_E=29&31. The J_E=29&31 beat require at least a third order process to populate the J_E=31 state, so its appearance at higher fields

Beat frequency (cm^{-1} . ± 0.7 cm^{-1})	Electronic state	J states	Beat Order*
39.8	E	29-31	4
42.5	E	27-29	2
43.8	A	30-32	6
44.8	E	25-27	4
46.9	A	28-30	2
50.0	A	26-28	2
53.1	A	24-26	6

Table 6.1: $\Delta J=2$ Quantum beat frequencies for J_A=24through 32.

*Beat order is defined as the sum of the $|\Delta J|$ of the states involved in the quantum beat relative to the launch state. From Eq. (6.7), this means that the beat order is defined relative to N_{FS} instead of pulse intensity.

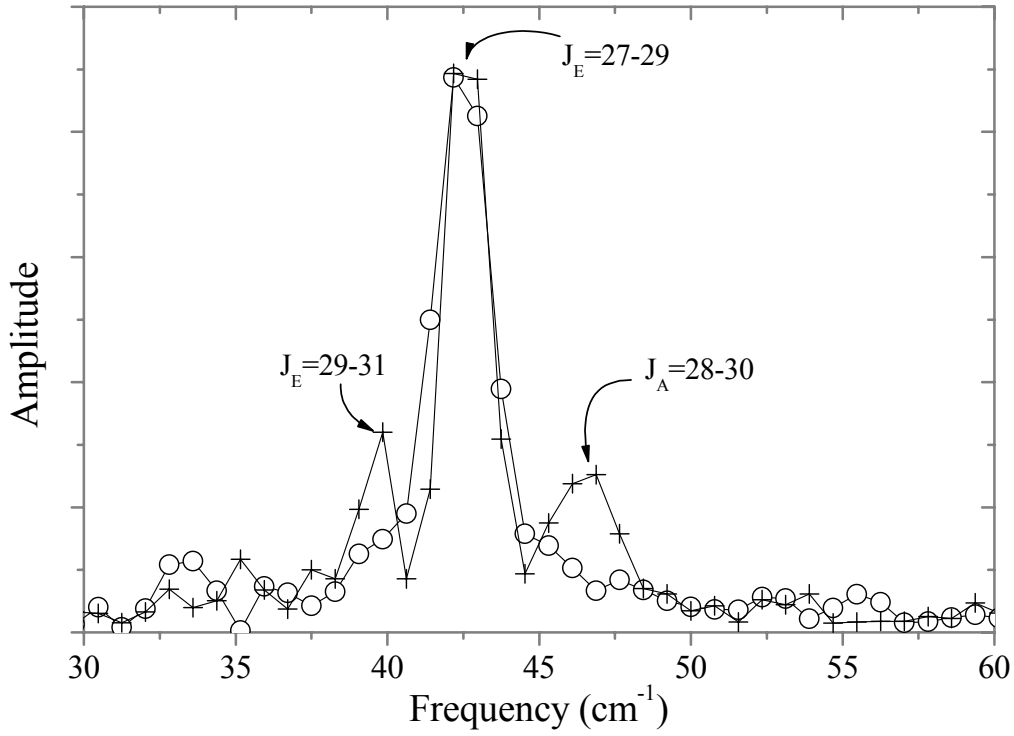

Figure 6.9: Fourier Tranforms for quantum beats at two different peak field strengths. The (○) represent the FT for a peak pump power of ~10^8 W/cm^2 (unfocused beam), and the (+) represent the FT for a peak pump power of ~10^{11} W/cm^2. Notice the appearance of new beats in the stronger field case. In the low power case, the A state beats were not observed due to insufficient probe power to drive multiphoton ionization. At the high power case here, the low J beats (J_E=25-27 and J_A=26-28) are minimal due to spectrally weak probe light at the frequencies that photoionize these states, *i.e*. the optimal pulse for E ←A population transfer is slightly suboptimal for low J photoionization.

should come as no surprise. An additional quantum beat at 44.8 cm^{-1} between J_E=25&27 on the E state is sometimes present, but is not observed here for two reasons: the probe spectrum favors the higher J quantum beats, and the beat frequency slightly overlaps the J_A=28&30 frequency. Also, the lack of the J_A=26&28 beat at 50 cm^{-1} suggests that photoionization yield for low J is small. This occurs here because the wavelength to which the laser is tuned to optimally pump the states of interest is suboptimal for multiphoton ionization of the lower J part of the rotational manifold of states.

Quantum beats that are composed of states excited via high order process will show energy dependent dynamics that vary wildly from linear[66]. The quantum beats as we observe them consist of an interference between two states. As a reminder, the coherence term from Eq. 1.1 has a cosine term with a leading factor that contains the wave function coefficients for each interfering state:

$$\text{Coherence} \propto |pr_1 pr_2||c_1||c_2|\cos(\omega_{12}t+\varphi) \qquad (6.7)$$

where all terms have been previously defined. Of particular interest is the relationship between the coefficients c_n and the electric field amplitude. In the weak field, first, second, third, etc. order processes are related to the electric field to the first, second, third, etc. power. The quantum beat for a pair of first order states (i.e. J_E=27-29) goes as the electric field squared, so it is considered a second order beat. The primary type of quantum beat with the launch state on the A state will also go as the electric field squared, since it involves a product of a second order and a zero order state, giving a net second order process. As the transition strength moves out of the weak field, these simple assumptions become more

difficult to apply. Figure 6.10 shows the quantum beat amplitudes for three types of beats as a function of pulse amplitude.

To gather this data, first the spectrum was manipulated so that the only light to pass through the SLM was a narrow band of ±8 cm^{-1} around each resonance between the J_A=28 and J_E=27 and 29 states, enough bandwidth to encompass all first, second, and third order transitions [see Fig. 6.1b]. Next, the bandwidth allowed to pass was attenuated, and a pump-probe trace was taken for each pump intensity. Next, we performed a Fourier Transform of the time-dependent signal. The 42 cm^{-1} beat (J_E=27&29) shows an initial rise followed by a longer decay with a recurrence at the highest N_{FS}. The 47 cm^{-1} (J_A=28&30) beat shows similar behavior, except it shows no recurrence at the highest energies. If both of these beats are second order processes, they should follow the same trajectories vs. N_{FS} at the lowest powers. A third beat at 39 cm^{-1} (J_E=29&31) is shown in the figure. This beat clearly differs from the first two, verifying that this is indeed a fourth order beat as defined in Table 6.1. It shows a threshold at which the quantum beat appears, much like the threshold behavior of calculated third order populations in Fig. 6.2. At the point where the quantum beat appears, significant population has departed from the state of J_A=30 to create the third order (J_E=31) state.

The fact that the fourth order quantum beat starts to approach the same amplitude as the second order beats suggests that it is being produced in parts of the laser beam where the pulse area approaches 2π (see Fig. 6.7). This observation suggests that pulse shaping schemes may be applied to the system in

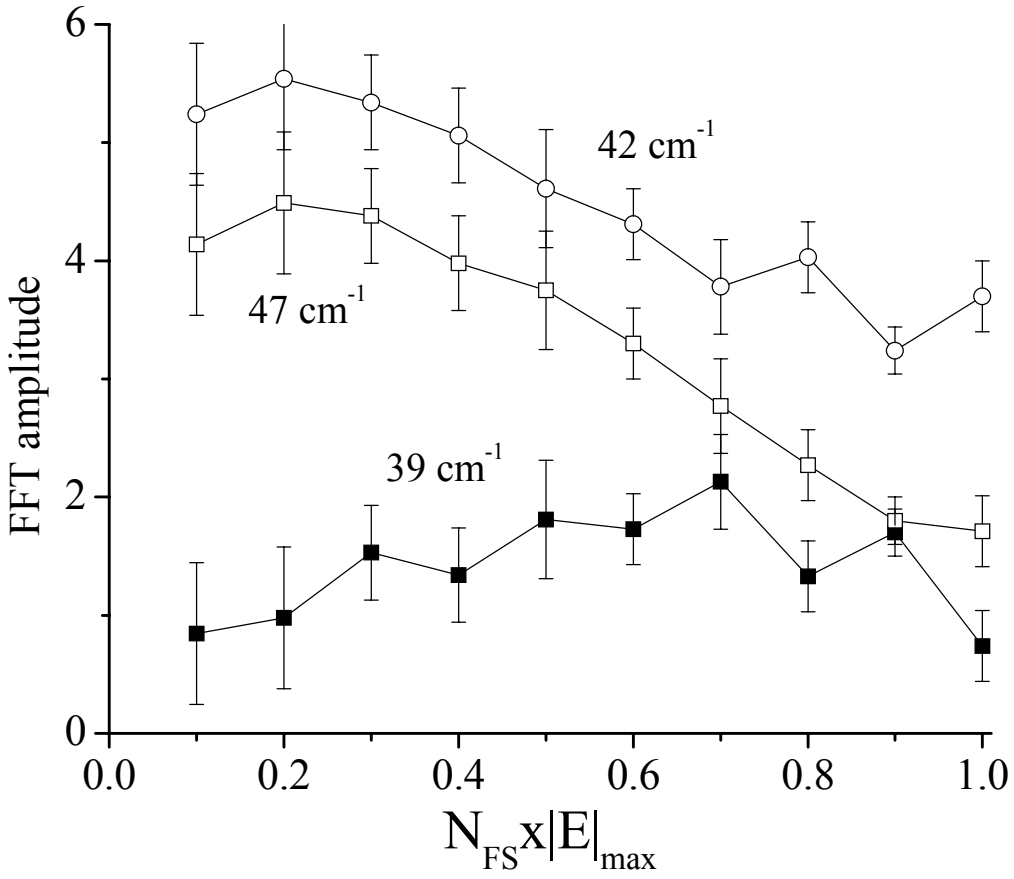

Figure 6.10: Field strength dependence of quantum beat amplitudes. A spectrum containing only first order resonances ($\omega_{\pm 1}\pm 8 cm^{-1}$) and nearby wavelengths was created by attenuating all light except for one window four pixels wide around each first order resonance. The relative electric field amplitude dependence of the quantum beats was then recorded. The 42 cm^{-1}, 47 cm^{-1}, and 39 cm^{-1} beats correspond to the coherences between J_E=27-29, J_A=28-30, and J_E=29-31, respectively.

order to control the population transfer to various states. To test the degree to which the populations can be transferred through the first order states, a sequential Rapid Adiabatic Passage pulse shape was tested[95]. To perform this test, the input pulse was attenuated outside a band that contained all of the resonant transitions [see Fig. 6.11]. The light that was able to pass was chirped by the application of a quadratic phase in the frequency domain. The net chirp amounted to ±4500 fs^2, as in the calculation of Fig. 6.11.

The result of the application of this pulse is illustrated in Fig. 6.12. Figure 6.12a shows a Fourier Transform of the recurrence signal for a pulse with zero phase as well as for positively and negatively chirped pulses; all traces have the same intensity spectrum. The unshaped case shows second and fourth order beating. In contrast, the positively chirped case shows a very large quantum beat corresponding to a second order beat (J_A=28&30). Also observed is a sixth order beat (J_A=30&32) at 43.75 cm^{-1}. The second order J_E=27&29 beat is almost completely attenuated, indicating that the second (and fourth) order *states* are populated at the expense of the first order *states*. Here, the beat at 46.9 cm^{-1} is identified as an A state beat since there is a large beat involving the ΔJ=32 state, which is very far removed in J space from the J=25 state involved in the E state

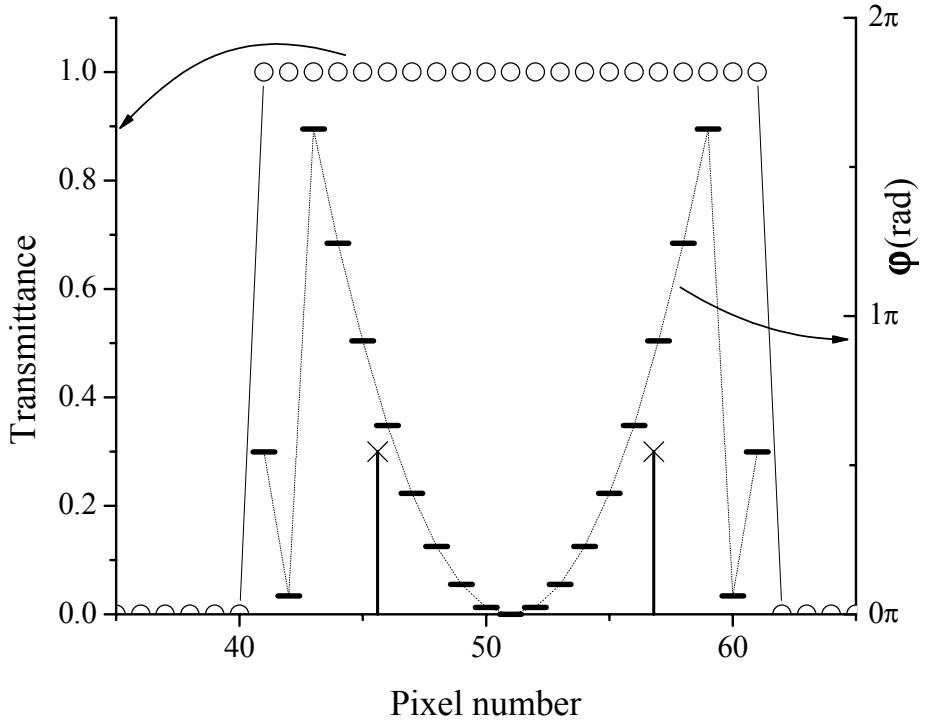

Figure 6.11: Phase and amplitude mask used to induce sequential rapid adiabatic passage events. A window of 84 cm^{-1}, centered to encompass all resonances up to 6^{th} order, allowed light to pass through the pulse shaper (○). Within that window, a chirp of 4500 fs^2 was applied (—). First order resonances are marked (×).

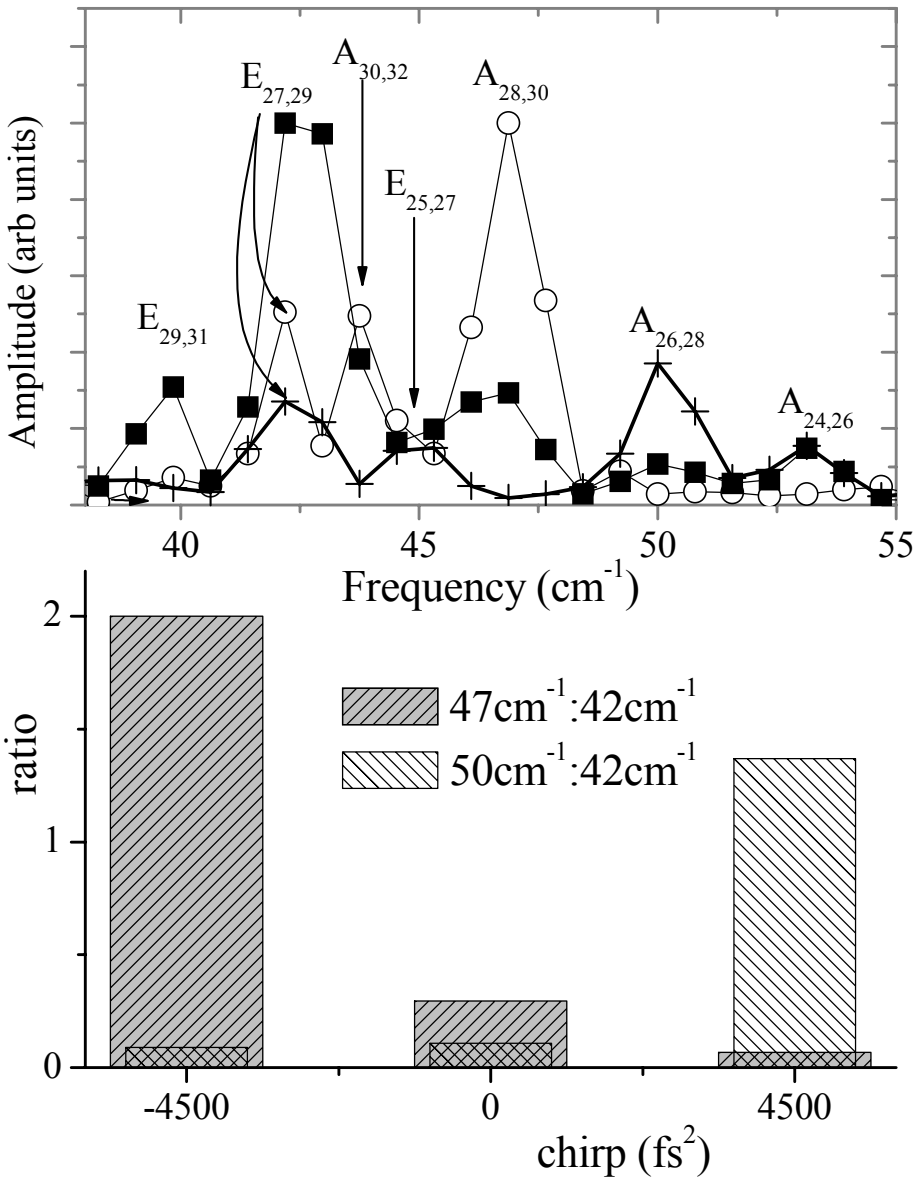

Figure 6.12: Implementation of Raman state selectivity based on the sign of chirp. Panel a: Fourier Transform of quantum beats for non-phase-shaped pulse (■), positively chirped pulse (○), and negatively chirped pulse (+). Quantum beats are labeled by their electronic state, as well as the J state quantum numbers. Panel b: Ratio of A state beats and the E state beat at 42 cm^{-1}. In both chirped cases, the ratio of A state beats is measured to be greater than 20, and is limited by the signal to noise ratio.

beat also at 44.8 cm^{-1}. Similar results, except with the opposite direction of the J transfer, is seen for negatively chirped pulses. For the negatively chirped case, the E state beat is reduced significantly, but the overall amplitude of the A state quantum beats is also small since the probe wavelength for small J is suboptimal, as in Fig. 6.9.

Fig. 6.12b contains a comparison of the amplitudes of various beats as the sign of the chirp is changed. It is quite clear that changing the sign of the chirp effectively selects the pathway being excited by the sequential Rapid Adiabatic Passage mechanism proposed above, with a selectivity between the Stokes and anti-Stokes quantum beats approaching unity. Also remarkably striking is the fact that the observed ratio of the A state quantum beats relative to the J_E=(27&29) beat approaches a factor of 2, even in the presence of the nonuniform laser beam. Based on the calculations of Fig. 6.8, this selectivity can only be reached at field strengths above 2π, and even at the maximum the ratio in the calculations only reaches 5. This number should be even lower in the experimental situation, since the A state beats are detected via a two-photon ionization, as opposed to the first order photoionization of the first order beats.

In addition to the ladder climbing technique described above, another technique has been developed by other groups that shows a high degree of robustness with respect to power: STIRAP[79]. In the STIRAP Λ excitation scheme—where there are two ground states and one excited state (e.g. only J_A=28 & 30, J_E=29 in the above model)—the three level system is "dressed" by two resonant excitation sources corresponding to the pump and dump frequencies. In

the case where the dump frequency slightly *precedes* the pump frequency, robust excitation of the Stokes state is seen. Unfortunately, in this experimental system, the dump then pump pulse order that corresponds to the excitation of the $\Delta J=2$ state is nearly identical to the pump then dump excitation to $\Delta J=-2$. This pathway ambiguity prevents the implementation of STIRAP in the previously described rotational system.

In these experiments, the degree of population transfer is not the observed quantity. Instead, the observed characteristics are coherences between states, as in Eq. (6.7); if all population were transferred to a single state, then the coherence would be zero. Still, it can be tentatively concluded that *most* of the population is transferred to the $\Delta J=\pm 2$ states as a result of the large amplitude of the second and sixth order beats. Also, the good agreement with the theoretical mechanism supports the conclusion that most population finds its way to the target states. Further experiments that are sensitive to individual populations, such as fluorescence detection, will verify these final state populations. One expected loss in quality of data by using fluorescence detection is the probe pulse beam sampling effect, as described in Eq. (6.7) will be lost. This can be overcome by carefully creating a spatially uniform electric excitation field, or by using a variant of Stimulated Emission Pumping to detect final state populations.

These experiments can also be improved by more carefully selecting the chemical system being studied to minimize loss mechanisms such as pump pulse multiphoton ionization. An attempt to overcome this in our current experiment by attenuating nonresonant wavelengths in the pump has shown some promise, but

more study is necessary to fully characterize the spectral extent to all multiphoton ionization pathways. We have shown that quantum beat amplitudes can be increased by up to 70% by attenuating nonresonant frequencies. A potential solution could be to perform these experiments on a system with a much higher ionization potential, or even to lower the energy of the launch state so that an additional photon of light is needed to reach the ionization continuum.

Chapter 7

Electronic wave packets

7.1 Introduction

Wave packet dynamics have been studied extensively on single electronic states (see previous chapters) and on multiple highly excited molecular Rydberg states[96]. Interactions between electronic states have also been observed in the context of observing unimolecular reactions such as dissociation[2, 4]. Yet the interactions between simultaneously propagating wave packets on intermediate energy electronic surfaces has received little attention[97-101]. Vast amounts of research have been undertaken to study interactions of electronic wave packets in atoms, but little has been addressed yet in molecules[102]. Calculations have addressed simple molecular systems such as H_2[97-99], and some experiments have been performed on the hyperfine splitting in molecular NO[101]. In all of these cases, the approximation can be made that the differences between interacting electronic states are small; all electronic states are approximately identical except for a total energy offset. Recently, experiments have been performed that control the angular momentum of electronic wave packets in atoms[103]. The primary reasons for this lack of study of electronic wave packets in molecules include the lack of efficient detection schemes or overall signal strength and lack of knowledge of the states[96]. In the case of Li_2, both of these conditions can be overcome. Much study has gone into the optimization of state resolved photoionization of Li_2, and significant excited state spectroscopy

has been performed, making the understanding of wave packets on highly excited electronic states possible[47, 104-110]. The experiments described in this chapter will examine an energetic region of Li_2 that is at the upper end of those states that have proven theoretically tractable using standard spectroscopic experiments coupled with ab initio theory, while at the same time is at the lower end of those states whose description using "top down" techniques such as multichannel quantum defect theory is valid.

Using ultrafast pump-probe spectroscopy, we observe quantum beating between rovibrational states on the $G^1\Pi_g^+$ and $F^1\Sigma_g^+$ electronic curves of Li_2. Using a narrow bandwidth cw laser, a launch state is prepared on the $A^1\Sigma_u^+$ electronic potential energy curve (v_A=11, J_A=28). From this launch state, a wave packet is prepared on these low lying Rydberg levels using the output from the OPA (λ_0 = 550 - 590 nm) and is subsequently probed by a second near IR ultrafast pulse (λ_0 = 800 nm). As the OPA wavelength is scanned, quantum beats between P, Q, and R branch rotational states for a progression of vibrational states on the G curve is observed. At a pump wavelength of 560 nm (G_e=35,000 cm^{-1}, IP=41490 cm^{-1}), in addition to rotational beating on the G curve (v_G=10-14, J_G=27-29), electronic beating between the G (v_G=13, J_G=27-29) and F (v_F=26, J_F=27) states is observed. As a result of the relatively low lying electronic states involved (n~4), there is a clear breakdown of the simplifying Δv=0 propensity rule for quantum beating in high lying molecular Rydberg wave packet work[96, 102], indicating a complex vibrational structure.

The fact that the interfering states occupy different electronic states with different angular momenta suggests a potential handle for controlling dynamics. It has been shown in atoms that states with higher angular momentum are more sensitive to external fields than those with less angular momentum[111]. Through this mechanism, electric fields can be used to Stark shift one electronic state relative to the other[112]. This process has been exploited in designing molecular wave packets based upon the splitting of an electronic fine structure within a series of states with identical angular momentum[113].

This first part of this chapter will be divided into several sections, including a summary of the experimental techniques and a general overview of the energetic region being studied followed by presentation of the experimental results. Quantum beating between rotational states for a progression of vibrational levels on the G $^1\Pi_g$ potential energy curve is shown as well as beating between states on the G and F$^1\Sigma_g^+$ potential energy curve. An analysis and discussion of the experimental results including prospects for improvements in the experimental scheme will be posited. This chapter will then conclude with a summary of some experiments performed to understand a spurious transient signal observed with excitation by 670-690 nm light.

7.2 Experimental and Theoretical Overview

The experiments here focus primarily on the observation of wave packet dynamics in two excited electronic states that are accessible from launch state $A^1\Sigma_u^+$, v_A,J_A=11,28 (E_{tot}=17,151 cm^{-1}). After preparation of this launch state, as

described in chapter 2, output from the OPA pumps accessible excited states, then ~800 nm ultrafast pulses photoionize those states pumped by the OPA output. The central wavelength of the OPA output is scanned over a range from 17,000 to 18,000 cm^{-1}, with a bandwidth of ~150 cm^{-1} FWHM. The pump-probe delay is scanned over a range from about 0.0 ps to greater than 30 ps. In the weak field, parallel polarization, non-transient limit, the coherent signal can then be expressed as a variation of Eq. (1.1):

$$S(t) \propto \sum_f \sum_m |\, a_{fm}\,|^2 |\, a_{mi}\,|^2 + \sum_f \sum_m \sum_{n>m} \left| a_{fm} a_{mi} a_{fn} a_{ni} \right| \cos\left(\omega_{nm} + \phi_{nm,f}\right), \quad (7.1a)$$

where *i, f*, and *m* (*n*) refer to the launch, final, and intermediate states, respectively. All other terms have previously been defined, but an additional detail pertaining to the a_n coefficients will be helpful:

$$a_{21} \propto \varepsilon(\omega_{21}) \left\langle v_2 J_2 \left| \hat{\mu}_{elec}(R) \right| v_1 J_1 \right\rangle, \quad (7.1b)$$

where 2 and 1 refer to the final and initial states of a particular single photon transition. Note that the transition dipole moment operator $\hat{\mu}_{elec}(R)$ is now dependent on both the specific pair of states in a transition and the vibrational coordinate *R*[105]. The implications of this are twofold: the transition dipole moment operator may lead to an element that can be controlled, and the FCF is more complex than a simple vibrational overlap[105].

Several bound electronic states are energetically accessible from the launch state with a pump pulse energy of 17,800 cm^{-1}[104, 107-110]. See Fig. 7.1 for the potential energy surfaces in the region examined here. Five singlet electronic states are bound with a total energy around 35,900 cm^{-1} total energy.

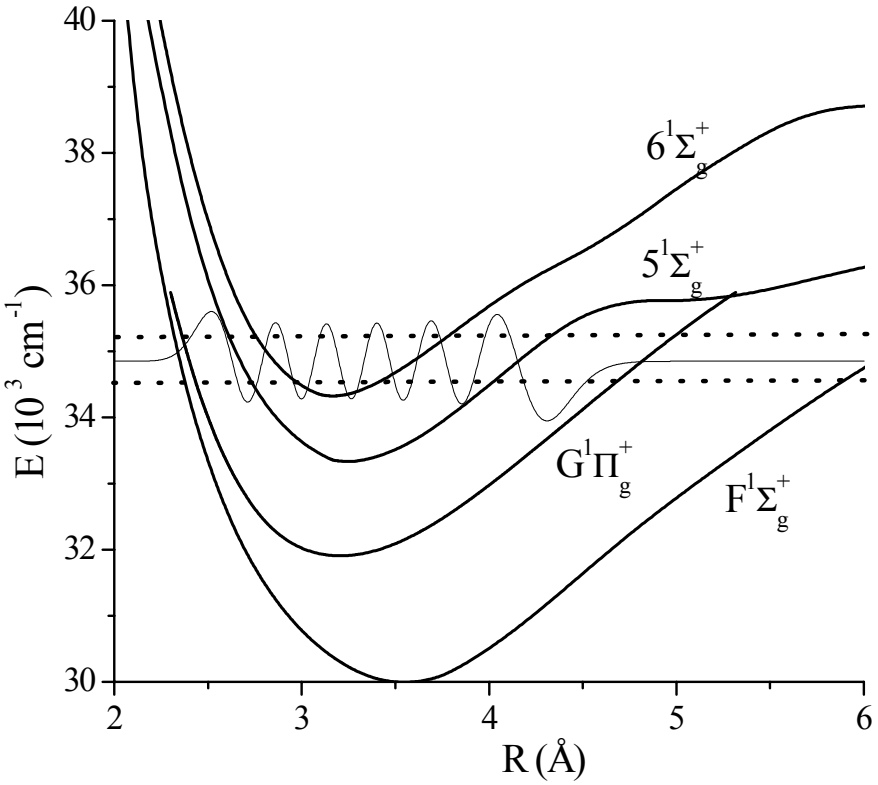

Figure 7.1: Potential energy curves in excitation region. Also shown is the launch state wavefunction superimposed on the relevant energy regions, as bounded by the horizontal dotted lines. The F, G, and 5 & 6 curves are taken from references [104], [109], and [108], respectively. At the relevant energies here, the low lying $E^1\Sigma_g^+$ state is bound by less than 500 cm^{-1}, so it is not included in the figure.

displaying the discrete wave packet dynamics that will be examined later. The The E $^1\Sigma_g^+$ state is bound, but is very near its dissociation limit (35,700 cm^{-1}) in the experiments examined here, and its near continuum behavior precludes it from $5^1\Sigma_g^+$ and $6^1\Sigma_g^+$ states are included in the figure, but with the v=11 launch state, the low lying vibrational levels that are accessible have small vibrational overlap with this launch state wavefunction. The inner and outer turning points of the $5^1\Sigma_g^+$ and $6^1\Sigma_g^+$ states fall within the spatial extent of the launch state wave function that is completely oscillatory. In contrast, the inner walls of the F and G potentials nearly touch, and overlap well with the inner part of the launch state wave function. In fact, calculations predict three orders of magnitude smaller vibrational overlap between the launch state and accessible states on the 5 and 6 states compared to accessible levels on the F and G states. This analysis is only a first approximation, neglecting overlap with the vibrational wavefunction of the final, autoionizing Rydberg state. Also, small deviations in the functional form of the transition dipole operator with respect to R can introduce uncertainties to the simple calculation referred to above, but for the large differences in vibrational overlap such as this, the above conclusions remain qualitatively valid.

Working from the assumption that only the F and G states play a role in the dynamics seen here, a portion of the spectrum of states that can be excited via strongly allowed transitions from the launch state is shown in Fig. 7.2. The F and G states are based upon fits to experimental data and are calculated according to the following expression[109, 110]:

$$E_{tot} = G_v + B_v[J(J+1)-1] - D[J(J+1)-1]^2 + q[J(J+1)] \qquad (7.2)$$

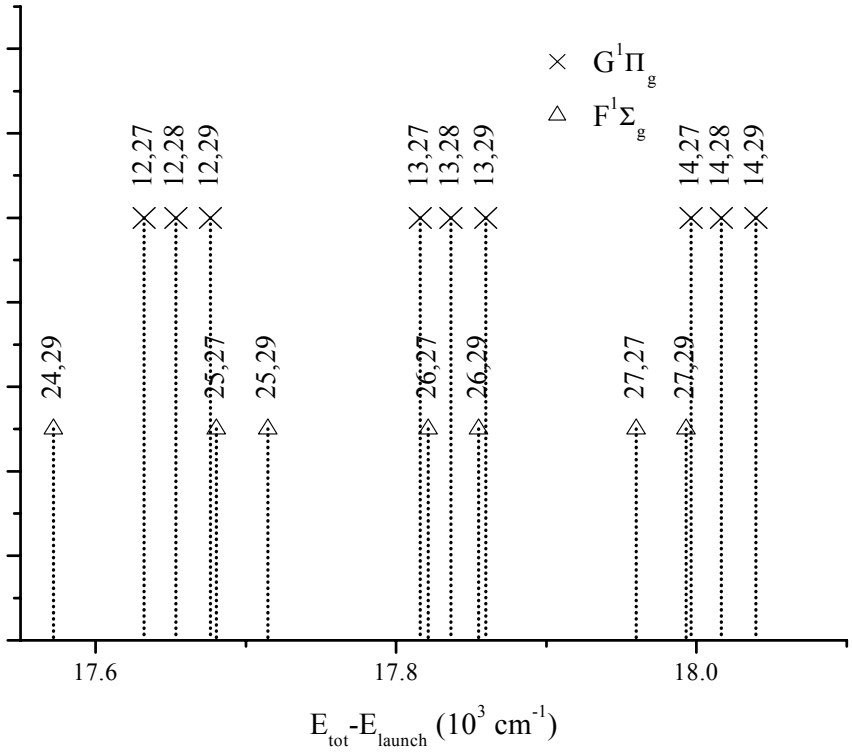

Figure 7.2: State locations accessible from the v_A, J_A=11, 28 launch state with a central pump energy of 17,550 cm^{-1} to 18, 100 cm^{-1}. P and R branch transitions are included for the $F^1\Sigma_g^+$ state, and P, Q, and R branches are included for the $G^1\Pi_g^+$ state. States are labeled as (v, J).

where G_v is the energy for vibrational level v, B_v is the rotational constant for vibrational level v, D is the centrifugal distortion constant, and q is the Λ doubling parameter. The centrifugal distortion constants are calculated based upon the Dunham fit parameters for the rotational constant Y_{01} and vibrational frequency Y_{10} so that $D=4Y_{01}^3/Y_{10}^2$[114]—approximately $4.31\text{x}10^{-6}$ cm^{-1} and $7.84\text{x}10^{-6}$ cm^{-1} for the F and G states, respectively. The Λ doubling parameter only applies to vibrational levels on the G state, splitting each rotational level into two, hence the term "doubling" parameter. For even J_G, the higher lying state has (+) parity, and the lower lying state has (-) parity, and for odd J_G, this is reversed. To maintain the +↔- parity selection rule, this means that the P and R transitions excite the higher level, and the Q branch the lower level, of each J_G doublet[112]. This means that in Eq. (7.2), the Λ doubling parameter only applies to the P and R branches of the G state. All constants for the F state are taken from refs. [107, 115], except for the centrifugal distortion constant which is taken from ref. [116]. V, B, and q for v_G=11 and 12 are taken from ref. [109], and the rest of the constants for the G state are taken from ref. [110]. The state energies for the F state around v_F, J_F=26, 27&29 have not been experimentally determined elsewhere, so the fit values have been given with an error of 0.25 cm^{-1} assumed. In the G state, similar errors should be assumed.

7.3 Results

As stated previously, the observed wave packets show very slowly decaying behavior, as shown in Fig. 7.3. Figure 7.3a shows the time domain pump-probe signal using a pump pulse with a central energy of 17,850 cm^{-1}, and a

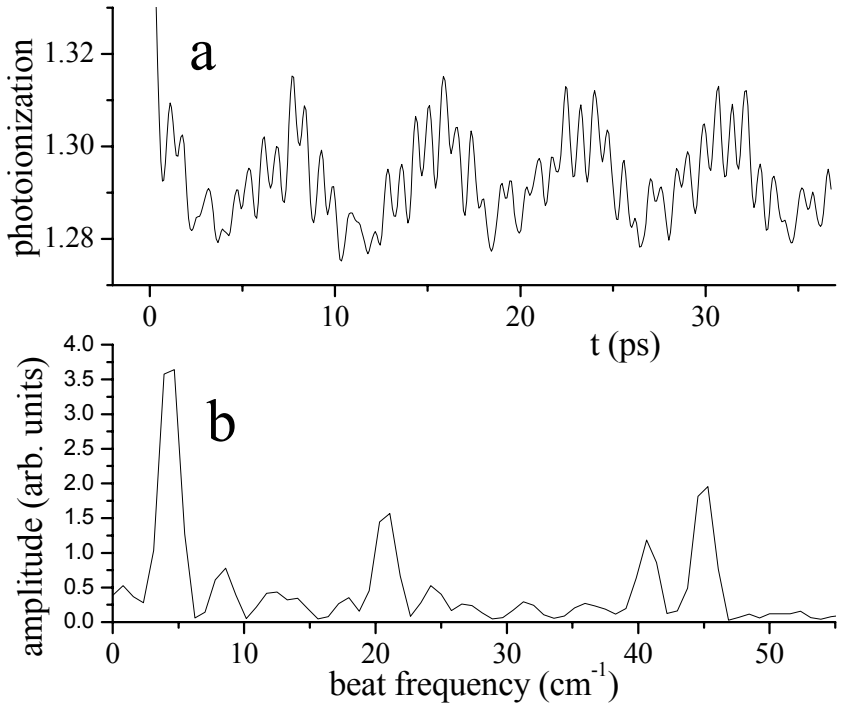

Figure 7.3: Pump-probe signal for a pump energy of 17,850 cm^{-1} for a launch state of v_A, J_A=11,28. Panel a shows the photoionization signal as a function of pump-probe delay. Panel b shows the Fourier Transform of the signal from panel a. Beats at energies of 4, 21, 41, and 45 cm^{-1} are clearly present. Possible peaks are also located at 8 cm^{-1} and 25 cm^{-1}.

bandwidth of 150 cm^{-1} FWHM. Notice that there is a very pronounced low frequency oscillation present along with several higher frequency oscillations. To analyze the nature of the beats, an FT is performed on the signal after t=0.0 ps. The Fourier Transform of this signal shows four pronounced peaks in the beat spectrum. Beats are observed at approximately 4, 21, 41, and 45 cm^{-1}. Each of these peaks is very narrow, in fact their width is defined by the pump-probe scan length. This narrow linewidth suggests that the interfering wavefunctions are relatively stable and do not quickly decay to secondary states.

To identify the quantum beats in Fig. 7.3, the pump pulse energy was varied in an attempt to view any spectral trends. Figure 7.4 shows the FT spectra of the quantum beats observed for a variety of central pump energies ranging from 17,100 cm^{-1} to 18,200 cm^{-1}. In the figure, each spectrum has been offset on the vertical axis to show the relative pump pulse energy. The spectral amplitudes have been normalized so that the beats around 45 cm^{-1} have similar amplitudes. In the case where no beats were observable above the noise level, the spectra were normalized so that the strongest peak in the spectrum coincides with the amplitude of the observable beats around 45 cm^{-1} [see spectra at 17,500 cm^{-1} and 17,600 cm^{-1}]. Due to large instabilities in the experimental apparatus, the amplitudes of the beats are generally unreliable, so an analysis of the spectral amplitudes is generally intractable. However, the *frequencies* of the quantum beats can be reliably observed since, in the weak field limit, the frequencies are independent of the laser intensity or overlap and only need to be sufficiently above the noise to detect [see Eq. (7.1a)]. Each of the peaks that have amplitude

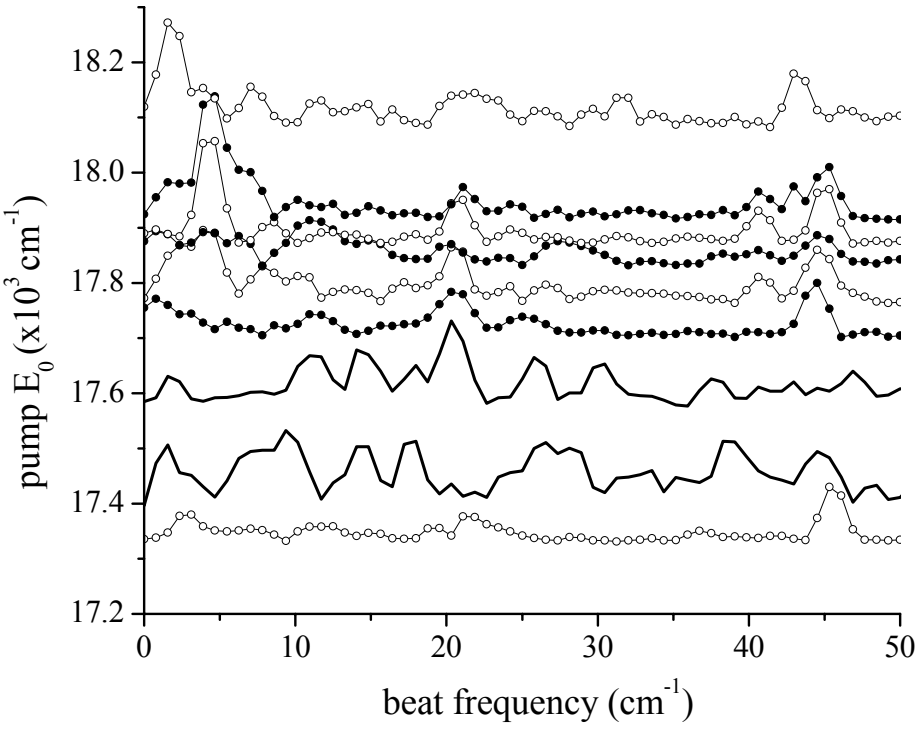

Figure 7.4: Fourier Transform quantum beat spectra for varying pump energies. All traces have been rescaled to show peaks at around 45 cm^{-1}, if present. Where no significant peaks are visible (solid lines), the spectra have been amplified to show the noise baseline. All spectra have been offset to reflect their respective pump pulse energy. Where peaks are clearly above the noise level, the frequency is recorded.

more than twice the noise level were fit with a Gaussian lineshape, and the central frequency is obtained.

A summary of the observed beats as a function of central pump energy is plotted in Fig. 7.5. The error bars for the beat frequencies reflect the widths of the peaks as recorded in Fig. 7.4, except the lowest frequencies which have a higher error due to laser drift as a function of delay stage position. Also included in the figure are the predicted beat frequencies assuming rotational quantum beating in the $G^1\Pi_g^+$ state, and where they are expected to be at their respective maxima. Several trends in the quantum beat frequencies should be noted. First, the beat around 45 cm^{-1} shows a trend toward lower frequencies as the pump energy is increased. The beat around 21 cm^{-1} shows similar behavior, although the degree of change falls within the error bars of the quantum beats. Around pump energies of 17,700 cm^{-1} to 18,100 cm^{-1}, additional beats around 2, 4, 25, and 41 cm^{-1} are observed. These beats are clearly not a part of the overall progression, lending credence to the possibility that the beats are something other than simple rotational beats in the G state. Also included in the figure is a schematic spectrum with a central wavelength of 17,880 cm^{-1} and a FWHM bandwidth of 200 cm^{-1}. This illustrates that quantum beats can be present even if the central pump pulse energy is shifted from the location of the peak beat amplitude. Given that the quantum beats have energies around 45 cm^{-1}, it is concluded that the predominant state at play in this case is the $\Delta J=2$ rotational beat in the G $^1\Pi_g^+$ state. This fits well with previous cw type spectroscopy since the $\Delta J=2$ rotational spacing in the F $^1\Sigma_g^+$ and 5 $^1\Sigma_g^+$ states are 34 cm^{-1} and 52 cm^{-1}, respectively. Additionally, the

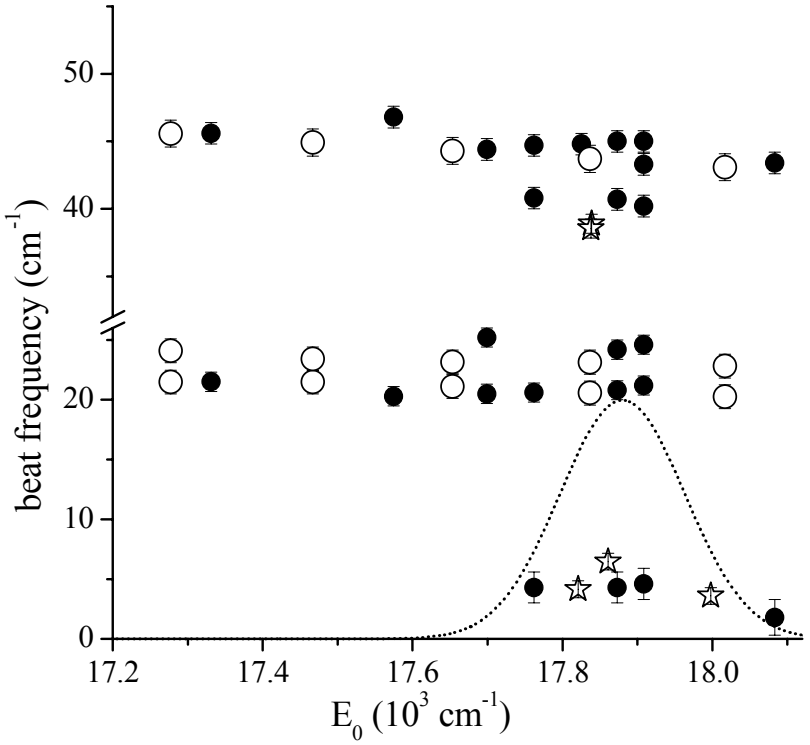

Figure 7.5: Quantum beat energy as a function of central pump pulse energy for 11,28 launch state. A sample spectrum with central energy of 17,880 cm^{-1} is included as a measure of pump pulse bandwidth. Closed circles are experimental quantum beat frequencies for different pump energies. Open circles are predicted rotational quantum beats in the G state, and stars are predicted beat frequencies between the F and G states around 17,850 cm^{-1} and 18,000 cm^{-1} as tabulated in Table 7.1.

progression of rotational beats around 21 cm^{-1} fit well with a $\Delta J=1$ beat (J_G=27&28) that is only possible in the G state due to the $\Delta\Lambda=1$ electronic component of the transition from A $^1\Sigma_u^+$ state. It is interesting to note that the J_G=28&29 beat around 23 cm^{-1} is predominantly absent from these spectra. Since this beat is observed with a rather weak amplitude in several of the traces, the predominant absence of these higher frequency $\Delta J=1$ beats is attributed to a systematically weak transition dipole moment to the Q-branch J_G=28 state as well as a preferential excitation to J_G=27 over J_G=29. Even though the observed quantum beat amplitudes involving the Q-branch states are less than predicted by Hönl-London factors, the line positions coincide with the expected positions[92].

To further verify that the main progressions seen are indeed rotational beats in the G state, a similar series of experiments was carried out for a different launch state. To make sure that any effects related to FCFs are minimized, the same vibrational launch state is chosen but the J state is changed, so that v_A,J_A=9, 16. Assuming the main progression is due to pairs of rotational states (J_G=15&17), the progression should be reproduced. Due to different rotational constants for the F and G potentials, a change in J would result in a shift of the states on one potential relative to the other. Figure 7.6 shows that the vibrational progression of rotational beats is reproduced, with no other beats present, failing to disprove the "extra" beats of Fig. 7.5 are beats between electronic states. Again in this lower J case, the rotational quantum beats involving the Q branch are weaker than those between the P and R branch states and only show the lower frequency beat, except for one low amplitude 14 cm^{-1} beat at E_0=17,530 cm^{-1}.

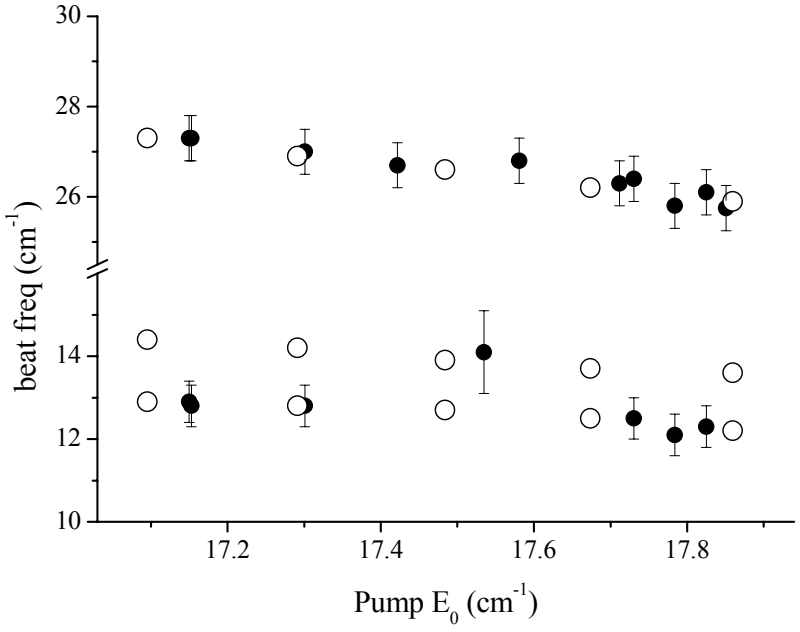

Figure 7.6: Quantum beat frequencies as a function of central pump energy from 11,16 launch state. Closed circles are experiment, and open circles are predicted rotational beats for different vibrational levels of the G state. The beat at E_0=17,530 cm^{-1} has large error bars because its presence was determined in the presence of significant noise.

The absence of additional beats in this progression is attributed to a shift in the F state energy levels due to different rotational constants for the F versus the G states. This further verifies that the beats are in fact rotational and not vibrational in nature. If the additional beats seen for the 11, 28 launch state were confined to the G state, they would be observed from this second launch state, but they are not.

7.4 Discussion and Future Directions

Previously completed high resolution spectroscopy suggests the wave packet excited with 17,850 cm^{-1} contains contributions from both the G and F states, although the reported state to state energy fits deviate up to 0.3 cm^{-1}, depending upon the source[107, 109, 110, 115, 116]. Since the G←A transition consists of $\Delta\Lambda=1$, single photon selection rules allow $\Delta J=0, \pm1$ transitions, hence the presence of the P, Q, and R branch states. The F←A transition corresponds to $\Delta\Lambda=0$, so parity selection rules allow $\Delta J=\pm1$, so only the P and R branch states of the F state are excited. Again, here only the line positions are shown; information regarding transition strength is not included. To identify quantum beats, energy differences must be taken into account, and these values have been summarized in Table 7.1.

Upon examining the expected quantum beat frequencies, the participating states can be inferred. Around 17,850 cm^{-1}, the P-R beat in the G state [*i.e.* G(13,27)-G(13,29)] is seen as the 45.0 cm^{-1} beat, as was established before. The P-Q beats are near their expected values at slightly less than half the P-R

E_{pu}=17,850cm^{-1}

		State (v, J)			
		F(26,27)	G(13,28)	F(26,29)	G(13,29)
State (v, J)	E_{tot}-E_{launch}/	17821.3	17836.6	17854.9	17859.7
G(13,27)	17816.0	(5.3)	20.6	38.9	43.7
F(26,27)	17821.3		(15.3)	(33.6)	(38.4)
G(13,28)	17836.6			18.3	23.1
F(26,29)	17854.9				4.8

E_{pu}=18,000cm^{-1}

		State (v, J)			
		F(27,29)	G(14,27)	G(14,28)	G(14,29)
State (v, J)	E_{tot} - E_{launch}/	17993.0	17996.3	18016.5	18039.4
F(27,27)	17959.9	(33.1)	(36.4)	(56.7)	(79.5)
F(27,29)	17993.0		3.3	(23.5)	(46.4)
G(14,27)	17996.3			(20.3)	43.1
G(14,28)	18016.5				(22.8)

Table 7.1: Expected quantum beat frequencies. For pump pulses centered around 17,850 cm^{-1} and 18,000 cm^{-1}, optically allowed rovibrational states on the F and G electronic curves are listed, along with their total energies. The quantum beat frequency is the difference in energies. Unobserved quantum beats are in parentheses.

frequency due to the Λ doubled spectrum of the G state. Interestingly, when they are observed, the Q-R beats are very weak and have a frequency over 1.0 cm^{-1} away from the predicted frequency. Almost all of the beats involving the F(26, 27) state are observed, with the beats at 4.2 cm^{-1} and 40.9 cm^{-1} observed. The absence of beats involving state F(26, 29) indicate that the photoionization pathway for that state is weak. Calculations show the vibrational overlap between the F(26, 29) and the ion ground state $X^+(25, 28)$ is very near zero. At the energies observed here, ionization proceeds through the $X^+(24, 28)$ state which has nonzero vibrational overlap with F(26, 29), but it should be remembered that there is a small difference in the meanings of the vibrational contribution to a transition dipole and the vibrational overlap between states: $\hat{\mu}_{elec}(R)$. Vibrational overlap calculations assume that $\hat{\mu}_{elec}(R)$ is constant over all R, but even at the small R where there is appreciable vibrational wavefunction in the states observed here, there will be small variations in the transition dipole operator. This means that the vibrational overlap calculations provide qualitative information, but fail to quantitatively characterize the transition strength.

Future experiments can be undertaken that can improve or exploit the effects seen here. In these experiments, quantum beat frequencies are observed as the pump wavelength is tuned. Since the probe light is the 800 nm fundamental from the regenerative amplifier, the final energy of the system is tuned along with the intermediate energy. In order to reduce the number of degrees of freedom in the analysis of the data, it would be advantageous to keep the final energy fixed. This could be overcome somewhat by simultaneously tuning the regenerative

amplifier output along with the OPA wavelength. This will technique will be limited since the optimization of the OPA output depends a great deal on the input pulse characteristics. An alternate means to keep the final energy fixed would be to include the addition of either a second OPA or the use of a second order of output from the OPA in these experiments. Since the signals are still rather weak at this point, the addition of a second OPA is possibly not feasible due to losses in the production of OPA light.

In this series of experiments, we have shown progressions of P-R, Q-R, and Q-P rotational quantum beats on various vibrational levels of the $G^1\Pi_g^+$ state of Li_2. In addition to these single electronic surface quantum beats, we have observed and identified various quantum beats between states on the G state and the $F^1\Sigma_g^+$ state. This observation of low lying Rydberg wave packets begins to bridge the gap between relatively low energy, hence isolated, wave packets on single electronic curves and high lying, nearly ionic Rydberg levels. Additionally, this work sets a benchmark for the types of signals to be expected as the total energy of a system increases towards the ionization limit.

7.5 Ultrafast transient behavior with 680 nm excitation

In the previous sections of this chapter, a type of electronic interaction was examined, where bound wave functions on separate electronic states beat against each other. In an effort to identify as many regions with observable wave packet dynamics such as in the previous section, we scanned other wavelength ranges.

In the process, another interesting spectroscopic feature was found: we observe a very large, transient, photoionization (PI) signal for a pump energy around 14,700 cm^{-1} while exciting the v_A, J_A=11,28 launch state. In fact, we see up to 100 times the total PI signal at short times relative to longer times, as shown in Fig. 7.7. Since this effect is so strong, it is studied to try to identify potentially useful traits. Much of the data support the conclusion that the fast decaying signal is an atomic ionization, motivating us to preempt further study of this effect with several of the studies presented in chapters 5 and 6.

The following section will begin with an examination of the spectral extent of the large transient peak. To verify that the transient effect is not a result of an isolated predissociative rovibrational state, launch states with J_A=16, 28, and 40 are compared. Next, the dependence of the transient signal on the pump polarization is presented. Finally, the results are discussed, and a very simple atomic mechanism will be proposed to explain the ultrafast effect. A significant unanswered question regarding the observed decay time is also presented.

7.5.1 Experiment and Results

The experimental setup for this section is nearly identical to that in the previous section, except that the wavelength range scanned by the OPA is slightly longer. In the experiments described here, a central wavelength range of approximately 650-700 nm (14000-15400 cm^{-1}) will be examined. Generally, the pump bandwidth is about 200 cm^{-1} FWHM. Since the wavelengths studied here are at the edge of the spectral output from the OPA, the bandwidth can be greatly

expanded due to nonidealities in the OPA alignment, further limiting the reliability of the spectral studies in this section. In all discussions, the central

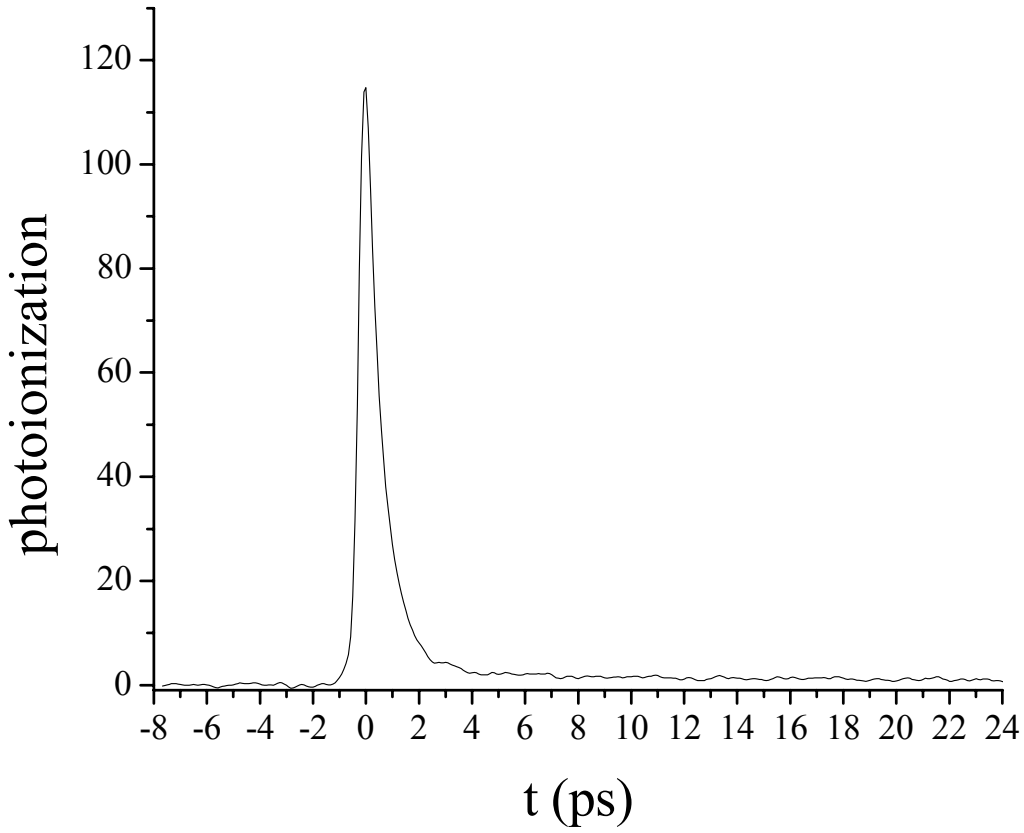

Figure 7.7: Pump-probe signal for E_{pu}=14,700 cm^{-1}. Probe polarization is parallel, and the photoionization (PI) has been normalized so that PI=0 for t<-4.0 ps, and PI=1 for t>20 ps.

energy of the approximately Gaussian spectral envelope will be cited as E_{pu}. Typical OPA output power is approximately 60 mW, but the power at the heat pipe is considerably less (~20 mW) due to losses along the optical path.

To test whether the transient peak was unique to a specific cw frequency, launch states with v_A=11 and J_A=16, 28, and 40 are excited with cw light at 603, 606.955, and 613. nm, respectively. Figure 7.8 shows the transient peak amplitudes for E_{pu} for J_A=16, 28, and 40. From all launch states, pump-probe transients show a similar transient behavior with a quickly decaying peak followed by a stable incoherent photoionization signal. Obviously, from this figure, there is no reliable J_A dependence to the transient signal. The spectral profile of the J_A=28 data shows a small (~100 cm^{-1}) shift relative to J_A=16 and 40, but there is still significant overlap of the profiles.

Finally, the pump polarization was rotated relative to the cw and probe pulses from parallel to the magic angle and perpendicular. Figure 7.9 shows a semilog plot of the pump-probe traces at each of these three critical polarizations for E_{pu}=14700 cm^{-1}, giving unexpected results. In the Fig. 7.9a, the traces have been normalized so that the signal for t<4.0 ps is set to zero, and the signal for t>10 ps is set to 1. Clearly, the transient signal goes down relative to the long time signal. The traces are characterized by an initial exponential rise time where $t_{1/2}$=0.16 ps, as should be expected from the timescale of the pump pulse. After t=0.0 ps, all of the traces exhibit exponential decay behavior with halflives of between 0.43 and 0.59 ps. The parallel and perpendicular signals both show slower ($t_{1/2}$~8 ps) decays, but with much lower amplitude, making quantitative

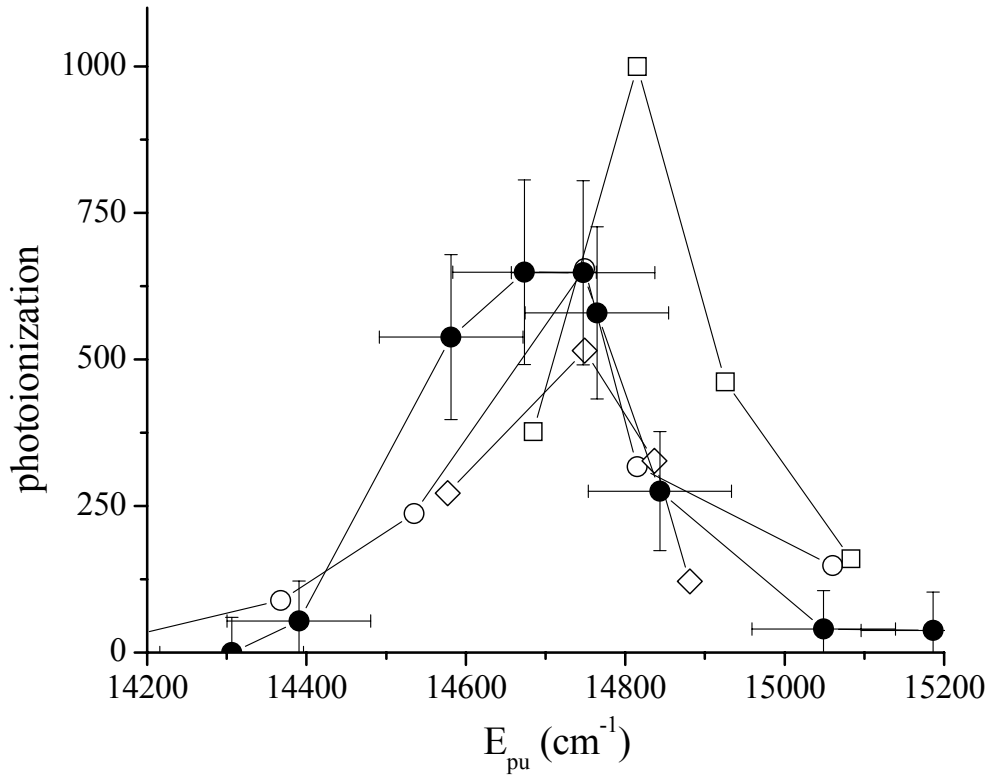

Figure 7.8: Dependence of transient peak height on central pump energy and J_A. The peak photoionization is been plotted as a function of central pump energy for J_A=16 (◇), J_A=28 (○,●), and J_A=40 (□). In all cases v_A=11. The solid circle dataset was taken before a lab relocation, and the open symbols were taken after; this is given to show the repeatability of the data. The error bars given for one data set are similar for the others.

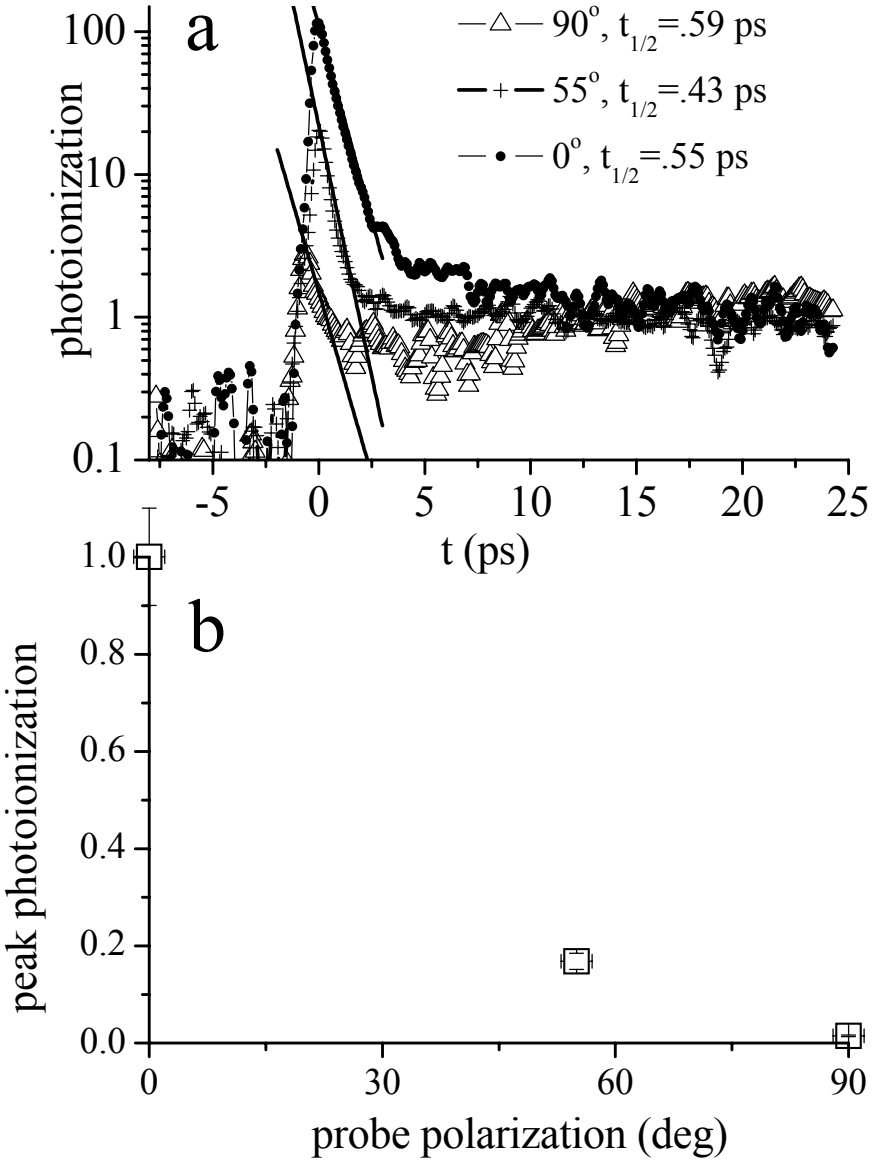

Figure 7.9: Polarization dependence of peak photoionization for parallel, perpendicular, and magic angle pumps. Panel a: Pump-probe traces for each probe polarization. The solid lines are single exponential decay fits, with halflives ranging from 0.43 to 0.59 ps. Panel b: Peak photoionization (relative to t>20 ps) as a function of pump polarization.

conclusions difficult. Figure 7.9b shows the peak amplitude as a function of probe polarization. It is clear that there is a dramatic decrease in the transient signal as a function of degrees off parallel.

7.5.2 Discussion

The data suggest that the main transient peak is an atomic, not molecular, effect. The predominant transient time dependent effect appears to come from an excitation to the quickly decaying 2p→2s atomic transition, resulting in a 1+3 photoionization pathway. To ionize, a total energy of 43,300 cm^{-1} is needed. This means that the 2p electron needs an additional 28,400 cm^{-1}, so a three photon resonance enhanced photoionization pathway with the 800 nm probe is suggested. The resonant enhancement may be possible since the energy between the 2p and 3p electronic levels is only 13,000 cm^{-1}, very near the probe energy, and to reach the ion an additional 15,900 cm^{-1} are needed. Three primary pieces of evidence support this atomic photoionization pathway conclusion: the polarization dependence of the signal, the fluorescence linewidth for the 2p→2s transition, and the similarities of the transient signal with and without the cw laser present. The observed lifetime of the transient peak is three orders of magnitude shorter than the literature value for spontaneous decay for the suggested transition; this large deviation from literature values requires further study before making a definitive conclusion for the transient effect seen.

That the main transient effect is atomic in nature is supported by the dependence of the photoionization on the polarization of the pump and probe

pulses. As it was shown in Fig. 7.9, the transient signal is nearly completely depleted by a simple rotation of the pump polarization relative to the probe. In a molecular system, this should not necessarily be the case. Assuming that there is a non-uniform m_J distribution in the state prepared by the probe (i.e. the state is aligned), the perpendicular signal should not go to zero. By setting the probe polarization to perpendicular relative to the probe, or rotating the frame of reference by 90^o, the effect (disregarding coherences) is approximately a swap of the effective m_J assignments from high to low and vice versa. We can quantify the alignment dependent contribution to the signal, assuming a uniform m_J distribution in the launch state, as the following:

$$S_{align} = \left| \sum_{pu=-J}^{J} \left\langle M_{prf} \left| \hat{\mu}_{pr} \right| M_{pri} \right\rangle \left\langle M_{puf} \left| \hat{\mu}_{pu} \right| M_{pui} \right\rangle \right|^2 , \qquad (7.3)$$

where M is the aligned spherical harmonic wavefunction with a specific J, *i* and *f* refer to the initial and final states of a transition, and *pu* and *pr* refer to the pump and probe steps. Here, it is assumed that all transitions follow the selection rule $\Delta m_J=0$. In the parallel case, the m_J quantum numbers *pu=pr*. For the perpendicular case, the quantum numbers can be approximated by $|pr| \approx J-|pu|$, so that in effect, the $m_{Jpu}=0 \rightarrow m_{Jpr}=\pm(J-1)$ and $m_{Jpu}=\pm(J-1) \rightarrow m_{Jpr}=\pm 1$. The effect of this transformation is that for J=27, the signal decreases by at most 13%. In Li_2, only the electronic ground state of the ion, which is known to have sigma symmetry, is reachable with a single photon from each of the pump and probe pulses. This requires that both pump and probe dipole moment operators lie along the same axis relative to the molecular axis, further justifying the analysis above.

This is all in contrast to the atomic case, where it is well known that a 1+3 photon absorption by an electron shows $\cos^2(\theta)$ dependence where θ is the angle between photon polarizations. This is the first bit of evidence that the transient effect seen in Fig. 7.7 is an atomic effect.

In the dispersed fluorescence spectrum under excitation by the 606.955 nm cw laser, many doublet lines appear that correspond to P and R branch decays from the launch state, as well as regularly spaced collisionally induced satellite lines. An additional line appears that is not part of these progressions at 670.5 nm. Figure 7.10 shows a portion of the dispersed fluorescence spectrum with a doublet at 14,770 and 14,830 cm^{-1} along with an additional prominent line at 14,910 cm^{-1}. The line at 14,910 cm^{-1} corresponds to the exact expected wavelength of the $2p \rightarrow 2s$ atomic transition, and in fact appears in the dispersed fluorescence spectra for many different excitation wavelengths. Higher resolution spectra even show the spin orbit splitting of less than 0.3 cm^{-1} for the 2p state. The linewidth is clearly wider than the molecular lines (the molecular linewidth here is primarily determined by the instrument response). The observation of a broadened line in the dispersed fluorescence spectrum only suggests a short lifetime. Since the linewidth is so much greater than expected from tabulated lifetimes, a significant problem exists with concluding a mechanism based upon this evidence.

One final piece of evidence supports the argument that the observed effect is a result of an atomic, not molecular process. The pump-probe traces observed above were gathered using a three beam interaction, but they can also be seen

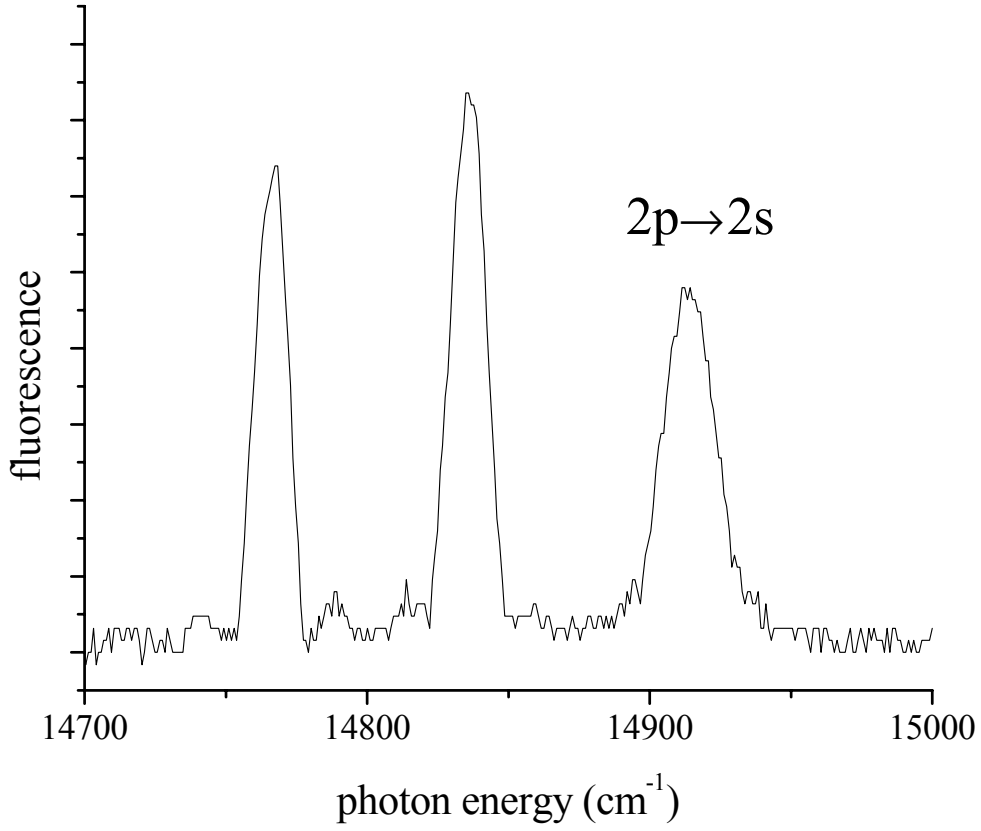

Figure 7.10: Fluorescence spectrum with excitation by 606.955 nm cw laser. The narrow peaks are molecular fluorescent lines with widths limited by the monochromator. The marked line corresponds to the 2p→2s line of atomic lithium.

without any cw laser present. While optically chopping the pump pulse, it is seen that the timescales and spectral profiles of the transient peaks match remarkably well with those in the presence of the cw laser. This evidence supports the mechanism where the OPA excites the 2p←2s transition from the atomic ground state followed by multiphoton ionization by the 800 nm pulse.

The proposed mechanism for the transient effect is a simple excitation of a fast decaying atomic state is supported by four primary pieces of evidence: the spectral profile of the ultrafast transient peak height coincides with the 2p→2s transition in atomic lithium, the dramatic polarization dependence of the peak height, the presence of a wide bandwidth fluorescent line, and the presence of the effect without the cw laser. The fact that the effect is seen to depend on the cw laser (when optically chopping the cw laser) indicates that the cw laser somehow participates in the dynamical effect, but a mechanism is not proposed. Due to the evidence supporting the ultrafast effect being primarily atomic, further study on this system was preempted in favor of studies that are more directly molecular in nature [see chapters 1-6].

This chapter has summarized a series of experiments that address a transient signal in our pump-probe signals. Several series of experiments were performed in an attempt to infer the nature of the transient effect, but with little success since all of the molecular explanations are characterized by significant flaws. This argument was supported by several pieces of evidence including a dramatic pump-probe polarization dependence, the presence of an atomic

fluorescence line in an ostensibly molecular fluorescence spectrum, and the presence of the effect both with and without the cw laser.

Chapter 8

Conclusion

This thesis demonstrates several aspects of coherent control of the well defined lithium dimer using ultrafast lasers and pulse shaping. Primary experimental results include a demonstration of feedback mediated control of photoionization of Li_2 using an evolutionary algorithm. Lessons learned by using the evolutionary algorithm were used to control both the transient amplitudes of contributing wavefunctions in a two-state wave packet. The effects of resonant and nonresonant wavelengths have also been elucidated. Further study into strong-field dynamics were also performed, showing that as the field strength increases, the complexity of the produced wave packets increases as the driving electric field increases. Finally, the possibilities for creating electronic wave packets in lithium dimer were studied, with some electronic wave packets observed.

Bibliography

[1] M. J. J. Vrakking, D. M. Villeneuve and A. Stolow, J. Chem. Phys. **105,** 5647 (1996).

[2] R. M. Bowman, M. Dantus and A. H. Zewail, Chem. Phys. Lett. **161,** 297 (1989).

[3] U. Siegner, M. Haiml, J. Kunde and U. Keller, Opt. Lett. **27,** 315 (2002).

[4] L. Zhu, K. Suto, J. A. Fiss, R. Wada, T. Seideman and R. J. Gordon, Phys. Rev. Lett. **79,** 4108 (1997).

[5] L. Allen and J. H. Eberly, *Optical Resonance and Two-Level Atoms*, 2 (Dover, New York, 1987).

[6] E. Mirowski, H. U. Stauffer, J. B. Ballard, B. Zhang, C. L. Hetherington and S. R. Leone, J. Chem. Phys. **117,** 11228 (2002).

[7] J. B. Ballard, H. U. Stauffer, Z. Amitay and S. R. Leone, J. Chem. Phys. **116,** 1350 (2002).

[8] N. Dudovich, B. Dayan, S. M. Gallagher Faeder and Y. Silberberg, Phys. Rev. Lett. **86,** 47 (2001).

[9] J. Che, J. L. Krause, M. Messina, K. R. Wilson and Y. Yan, J. Phys. Chem. **99,** 14949 (1995).

[10] M. Shapiro, J. Phys. Chem. **97,** 7396 (1993).

[11] E. Skovsen, M. Machholm, T. Ejdrup, J. Thogersen and H. Stapelfeldt, Phys. Rev. Lett. **89,** 133004 (2002).

[12] M. Shapiro and P. Brumer, J. Chem. Phys. **84,** 4103 (1986).

[13] A. P. Peirce, M. A. Dahleh and H. Rabitz, Phys. Rev. A **37,** 4950 (1988).

[14] L. Zhu, V. Kleiman, X. Li, S. P. Lu, K. Trentelman and R. J. Gordon, Science **270,** 77 (1995).

[15] A. Shnitman, I. Sofer, I. Golub, A. Yogev, M. Shapiro, Z. Chen and P. Brumer, Phys. Rev. Lett. **76,** 1886 (1996).

[16] C. J. Bardeen, V. V. Yakovlev, K. R. Wilson, S. D. Carpenter, P. M. Weber and W. S. Warren, Chem. Phys. Lett. **280,** 151 (1997).

[17] R. J. Gordon and S. A. Rice, Annu. Rev. Phys. Chem. **48,** 601 (1997).

[18] A. H. Zewail, G. Casati, S. A. Rice, M. Chergui, D. J. Tannor, T. Kobayashi and H. Rabitz, Adv. Chem. Phys. **101,** 3 (1997).

[19] J. Paci, M. Shapiro and P. Brumer, J. Chem. Phys. **109,** 8993 (1998).

[20] M. Bergt, T. Brixner, B. Kiefer, M. Strehle and G. Gerber, J. Phys. Chem. **103,** 10381 (1999).

[21] B. M. Goodson, D. Goswami, H. Rabitz and W. S. Warren, J. Chem. Phys. **112,** 5081 (2000).

[22] H. Rabitz, R. d. Vivie-Riedle, M. Motzkus and K. Kompa, Science **288,** 824 (2000).

[23] R. J. Levis, G. M. Menkir and H. Rabitz, Science **292,** 709 (2001).

[24] M. Gruebele, Theoretical Chemistry Accounts **in press,** (2002).

[25] T. C. Weinacht and P. H. Bucksbaum, Journal of Optics B **4,** R35 (2002).

[26] R. Bartels, S. Backus, E. Zeek, L. Misoguti, G. Vdovin, I. P. Christov, M. M. Murnane and H. C. Kapteyn, Nature **406,** 164 (2000).

[27] Z. Amitay, J. B. Ballard, H. U. Stauffer and S. R. Leone, Chem. Phys. **267,** 141 (2001).

[28] T. Baumert, T. Brixner, V. Seyfried, M. Strehle and G. Gerber, Appl. Phys. B **65,** 779 (1997).

[29] M. M. Wefers and K. A. Nelson, Opt. Lett. **18,** 2032 (1993).

[30] A. M. Weiner, D. E. Leaird, J. S. Patel and J. R. I. Wullert, IEEE J. Quant. Elec. **28,** 908 (1992).

[31] H. Kawashima, M. M. Wefers and K. A. Nelson, Annu. Rev. Phys. Chem. **46,** 627 (1995).

[32] Z. Amitay, R. Kosloff and S. R. Leone, Chem. Phys. Lett. **359,** 8 (2002).

[33] J. B. Ballard, A. N. Arrowsmith, L. Hüwel and S. R. Leone, Phys. Rev. A **66,** 043402 (2002).

[34] M. M. Wefers and K. A. Nelson, J. Opt. Soc. Am. B **12,** 1343 (1995).

[35] M. M. Wefers, K. A. Nelson and A. M. Weiner, Opt. Lett. **21,** 746 (1996).

[36] U. Gaubatz, P. Rudecki, S. Schiemann and K. Bergmann, J. Chem. Phys. **92,** 5363 (1990).

[37] L. Xu, N. Nakagawa, R. Morita, H. Shigekawa and M. Yamashita, IEEE J. Quant. Elec. **36,** 893 (2000).

[38] H. Rabitz and W. Zhu, Acct. Chem. Res. **33,** 572 (2000).

[39] T. Hornung, R. Meier and M. Motzkus, Chem. Phys. Lett. **326,** 445 (2000).

[40] A. Glass, R. Rozgonyi, T. Feuer, R. Sauerbrey and G. Szabo, Appl. Phys. B **71,** 267 (2000).

[41] T. Hornung, R. Meier, D. Zeidler, K.-L. Kompa, D. Proch and M. Motzkus, Appl. Phys. B **71,** 277 (2000).

[42] H.-P. Schwefel, *Evolution and Optimum Seeking*, (Wiley, New York, 1995).

[43] D. E. Goldberg, *Genetic Algorithms*, (Addison-Wesley, New York, 1989).

[44] D. Y. Meshulach, D.; Silberberg, Yaron, Optics Communications **138,** 345 (1997).

[45] R. Trebino, K. W. DeLong, D. N. Fittinghoff, J. N. Sweetser, M. A. Krumbugel and B. A. Richman, Rev. Sci. Inst. **68,** 3277 (1997).

[46] B. E. A. Saleh and M. C. Teich, *Fundamentals of Photonics*, 1 (John Wiley & Sons, Inc., New York, 1991).

[47] R. Uberna, Z. Amitay, C. X. W. Qian and S. R. Leone, J. Chem. Phys. **114,** 10311 (2001).

[48] R. Uberna, M. Khalil, R. M. Williams, J. M. Papanikolas and S. R. Leone, J. Chem. Phys. **108,** 9259 (1998).

[49] S. Zamith, J. Degert, S. Stock, B. d. Beauvoir, V. Blanchet, M. A. Bouchene and B. Girard, Phys. Rev. Lett. **87,** 033001 (2001).

[50] M. Gruebele and A. H. Zewail, J. Chem. Phys. **98,** 883 (1993).

[51] N. F. Scherer, D. M. Jonas and G. R. Fleming, J. Chem. Phys. **99,** 153 (1993).

[52] J. Cao, C. J. Bardeen and K. R. Wilson, J. Chem. Phys. **113,** 1898 (2000).

[53] A. N. Naumov, A. Materny, W. Kiefer, M. Motzkus and A. M. Zheltikov, Laser Physics **11,** 1319 (2001).

[54] E. I. Biolatti, R. C.; Zanardi, P.; Rossi, F., Phys. Rev. Lett. **85,** 5647 (2000).

[55] C. M. Tesch and R. de Vivie-Riedle, Phys. Rev. Lett. **89,** 157901 (2002).

[56] J. Ahn, C. Rangan, D. N. Hutchinson and P. H. Bucksbaum, Phys. Rev. A **66,** 022312 (2002).

[57] Z. Bihary, D. R. Glenn, D. A. Lidar and V. A. Apkarian, Chem. Phys. Lett. **360,** 459 (2002).

[58] M. A. Nielsen and I. L. Chuang, *Quantum Computation and Quantum Information*, 1 (Cambridge University Press, Cambridge, 2000).

[59] D. P. DiVincenzo, D. Bacon, J. Kempe, G. Burkhard and K. B. Whaley, Nature **408,** 339 (2000).

[60] M. N. Leuenberger and D. Loss, Nature **410,** 789 (2001).

[61] N. A. Gershenfeld and I. L. Chuang, Science **275,** 350 (1997).

[62] J. A. Jones and M. Mosca, J. Chem. Phys. **109,** 1648 (1998).

[63] J. I. Cirac and P. Zoller, Phys. Rev. Lett. **74,** 4091 (1995).

[64] D. Kielpinski, C. Monroe and D. J. Wineland, Nature **417,** 709 (2002).

[65] D. Oron, N. Dudovich, D. Yelin and Y. Silberberg, Phys. Rev. Lett. **88,** 063004 (2002).

[66] C. J. Bardeen, V. V. Yakovlev, J. A. Squier and K. R. Wilson, Journal of the American Chemical Society **120,** 13023 (1998).

[67] L. Nugent-Glandorf, M. Scheer, D. A. Samuels, A. M. Mulhisen, E. R. Grant, X. M. Yang, V. M. Bierbaum and S. R. Leone, Phys. Rev. Lett. **87,** 193002 (2001).

[68] R. Kodama, Nature **418,** 933 (2002).

[69] I. Last and J. Jortner, Journal of Physical Chemistry A **106,** 10877 (2002).

[70] J. Degert, W. Wohlleben, B. Chatel, M. Motzkus and B. Girard, Phys. Rev. Lett. **89,** 203003 (2002).

[71] R. Netz, A. Nazarkin and R. Sauerbrey, Phys. Rev. Lett. **90,** 063001 (2003).

[72] J. S. Melinger, S. R. Gandhi, A. Hariharan, J. X. Tull and W. S. Warren, Phys. Rev. Lett. **68,** 2000 (1992).

[73] T. H. Stievater, X. Li, D. G. Steel, D. Gammon, D. S. Katzer, D. Park, C. Piermarocchi and L. J. Sham, Phys. Rev. Lett. **87,** 133603 (2001).

[74] E. M. Hiller and J. A. Cina, J. Chem. Phys. **109,** 3419 (1996).

[75] V. S. Malinovsky and J. L. Krause, Phys. Rev. A **63,** 043415 (2001).

[76] J. Manz, H. Naundorf, M. Yamashita and Y. Zhao, J. Chem. Phys. **113,** 8969 (2000).

[77] M. Demirplak and S. A. Rice, J. Chem. Phys. **116,** 8028 (2002).

[78] K. Nagaya, Y. Teranishi and H. Nakamura, J. Chem. Phys. **117,** 9588 (2002).

[79] S. Schiemann, A. Kuhn, S. Steuerwald and K. Bergmann, Phys. Rev. Lett. **71,** 3637 (1993).

[80] J. Martin, B. W. Shore and K. Bergmann, Phys. Rev. A **54,** 1556 (1996).

[81] B. Y. Chang, I. R. Sola, V. S. Malinovsky and J. Santamaria, J. Chem. Phys. **113,** 4901 (2000).

[82] M. K. Schmitt, G.; Materny, A.; Kiefer, W., J. Phys. Chem. **102,** 4059 (1998).

[83] D. J. Nesbitt and R. W. Field, J. Phys. Chem. **100,** 12735 (1996).

[84] B. Y. Chang, I. R. Sola and J. Santamaria, Journal of Physical Chemistry A **105,** 8864 (2001).

[85] D. J. Maas, D. I. Duncan, R. B. Vrijen, W. J. van der Zande and L. D. Noordam, Chem. Phys. Lett. **290,** 75 (1998).

[86] R. B. Vrijen, D. I. Duncan and L. D. Noordam, Phys. Rev. A **56,** 2205 (1997).

[87] S. Chelkowski and A. D. Bandrauk, J. Chem. Phys. **99,** 4279 (1993).

[88] K. Sundermann, H. Rabitz and R. d. Vivie-Riedle, Phys. Rev. A **62,** 013409 (2000).

[89] R. A. Dressler, H. Meyer and S. R. Leone, J. Chem. Phys. **87,** 6029 (1987).

[90] H. Meyer and S. R. Leone, J. Chem. Phys. **105,** 5858 (1996).

[91] B. Liu and X.-J. Ning, Phys. Rev. A **64,** 013401 (2001).

[92] R. N. Zare, *Angular Momentum--Understanding spatial aspects in chemistry and physics*, (John Wiley & Sons, New York, 1988).

[93] W. Demtroder, *Laser Spectroscopy*, 2 (Springer, Berlin, 1998).

[94] H. U. Stauffer, J. B. Ballard, Z. Amitay and S. R. Leone, J. Chem. Phys. **116,** 946 (2002).

[95] B. Broers, H. B. van Linden van den Heuvell and L. D. Noordam, Phys. Rev. Lett. **69,** 2062 (1992).

[96] V. G. Stavros, J. A. Ramswell, R. A. L. Smith, J. R. R. Verlet and H. H. Fielding, Phys. Rev. Lett. **83,** 2552 (1999).

[97] F. Texier and C. Jungen, Phys. Rev. Lett. **81,** 4329 (1998).

[98] F. Texier, C. Jungen and S. C. Ross, Faraday Discussions **115,** 71 (2000).

[99] F. Texier and F. Robicheaux, Phys. Rev. A **61,** 043401 (2000).

[100] V. Blanchet, S. Lochbrunner, M. Schmitt, J. P. Shaffer, J. J. Larsen, M. Z. Zgierski, T. Seideman and A. Stolow, Faraday Discussions **115,** 33 (2000).

[101] J. Xin, S. A. Reid, F. Santoro and C. Petrongolo, J. Chem. Phys. **115,** 8868 (2001).

[102] J. R. R. Verlet and H. H. Fielding, Int. Rev. Phys. Chem. **20,** 283 (2001).

[103] J. R. R. Verlet, V. G. Stavros, R. S. Minns and H. H. Fielding, Phys. Rev. Lett. **89,** 263004 (2002).

[104] A. Pashov, W. Jastrzebski and P. Kowalczyk, J. Chem. Phys. **113,** 6624 (2000).

[105] I. Schmidt-Mink, W. Muller and W. Meyer, Chem. Phys. **92,** 263 (1985).

[106] J. M. Papanikolas, R. M. Williams, P. D. Kleiber, J. L. Hart, C. Brink, S. D. Price and S. R. Leone, J. Chem. Phys. **103,** 7269 (1995).

[107] S. Antonova, G. Lazarov, K. Urbanski, A. M. Lyyra, L. Li, G.-H. Jeung and W. C. Stawalley, J. Chem. Phys. **112,** 7080 (2000).

[108] M. Y. Song, P.; Liu, Y.; Li, Li; Jeung, G.-H., J. Mol. Spect. **215,** 251 (2002).

[109] J. Q. Shang, Jianbing; Li, Li; Lyyra, A. Marjatta, J. Mol. Spect. **203,** 255 (2000).

[110] R. A. Bernheim, L. P. Gold, P. B. Kelly, T. Tipton and D. K. Veirs, J. Chem. Phys. **74,** 2749 (1981).

[111] D. Townsend, A. L. Goodgame, S. R. Proctor, S. R. Mackenzie and T. P. Softley, Journal of Physics B **34,** 439 (2001).

[112] G. Herzberg, *Spectra of Diatomic Molecules*, 7 (D. Van Nostrand Company, Inc., Princeton, 1950).

[113] V. G. Stavros and H. H. Fielding, Phys. Rev. A **60,** 4774 (1999).

[114] G. Herzberg, *The Spectra and Structures of Simple Free Racicals*, (Dover Publications, Inc., New York, 1988).

[115] See EPAPS Document No. E-JCPSA6-112-013015. This document may be retreived via http://www.aip.org/pubservs/epaps.html.

[116] R. A. Bernheim, L. P. Gold, P. B. Kelly, C. A. Tomczyk and D. K. Viers, J. Chem. Phys. **74,** 3249 (1981).